12-1-2008

Robust longitudinal rate gyro bias estimation for reliable pitch attitude observation through utilization of a displaced accelerometer array

Ryan Weisman

Robust Longitudinal Rate Gyro Bias Estimation for Reliable Pitch Attitude Observation through Utilization of a Displaced Accelerometer Array

by

Ryan M. Weisman

Thesis submitted to the Faculty of the
Rochester Institute of Technology
in partial fulfillment of the requirements for the degree of

Master of Science
in
Mechanical Engineering

Approved by:

Dr.Agamemnon Crassidis -*Thesis Advisor* _____
Department of Mechanical Engineering

Dr. Tuhin Das _____
Department of Mechanical Engineering

Dr. Mark Kempski _____
Department of Mechanical Engineering

Dr. Edward Hensel _____
Department Head of Mechanical Engineering

Rochester, New York
December, 2008

Keywords: Attitude Estimation, Bias Estimation, Kalman Filtering, Rigid Body Dynamics

Permission to Reproduce Thesis

Robust Longitudinal Rate Gyro Bias Estimation for Reliable Pitch Attitude Observation through Utilization of a Displaced Accelerometer Array

I, Ryan M. Weisman, hereby grant permission to the Wallace Memorial Library of Rochester Institute of Technology to reproduce my thesis in the whole or part. Any reproduction will not be for commercial use or profit.

Date: _____ Signature: _____

December 2008

Abstract

In this thesis, a novel attitude estimation device is proposed utilizing cost-effective measurement sensors. The device fuses a rate gyroscope with an accelerometer array to estimate and eliminate the rate gyro bias online yielding accurate real time aircraft attitude tracking. Attitude determination algorithms are dependent on instantaneous and accurate measurements of translational and rotational body rates for precise estimation of vehicle orientation in three-dimensional space. Measurement error of instantaneous rate sensors, gyroscopes, is introduced via inherent biases and signal noise resulting in gyro drift. Integration of the rate signal for calculation of a net displacement amplifies these minute measurement errors leading to inaccurate and unreliable attitude observation. The proposed device is a departure from typical attitude observers and bias estimators due to its reliance on accelerometers measuring the local gravitational vector in lieu of additional magnetic field sensors or GPS. The end result of this work is a longitudinal attitude estimation device able to compute a rate gyro bias in real-time producing accurate pitch angle tracking while subjected to simulated aircraft flight conditions. The effectiveness of the newly constructed attitude estimation algorithm is demonstrated by comparison of attitude and rate gyro bias estimates produced from noise corrupted and biased sensors with the actual attitude of a nonlinear aircraft model and true rate gyro bias.

Acknowledgments

I would like to thank Dr. Agamemmon Crassidis for his guidance, patience, and research leeway because of his confidence in my abilities. I would also like to thank Dr. Tuhin Das and Dr. Mark Kempski for their guidance, help along the way, and their donated time and effort.

There are thousands to tell you it cannot be done,
There are thousands to prophesy failure;
There are thousands to point out to you one by one,
The dangers that wait to assail you.
But, just buckle in with a bit of grin,
Just take off your coat and go to it;
Just start in and sing as you tackle the thing
That "cannot be done,"
and you'll do it.
-Edgar A. Guest

In short,
"First you jump off the cliff and you build wings on the way down"
-Ray Bradbury

Contents

List of Tables

List of Figures

Nomenclature

Parameters

X, Y, Z	: Primary, Secondary, and Tertiary Coordinate System Axes
i, j, k	: Primary, Secondary, and Tertiary Unit Vector Directions
$\mathbf{S}$	: Translational Displacement Vector of Reference System Axes
$\mathbf{s}$	: Translational Displacement Vector of Vehicle System Axes
$\phi,\ \theta,\ \psi$	: Bank, Elevation, and Heading Euler Angles
$p,\ q,\ r$	: Roll, Pitch, and Yaw Vehicle Angular Rates
$\mathbf{F}$	: Force Vector
$\mathbf{W}$	: Weight Vector
$\mathbf{M}$	: Moment Vector
$\mathbf{V}$	: Velocity Vector
m	: Vehicle Mass
$\vec{\omega}$	: Vehicle Angular Rate Vector
$\overleftrightarrow{\mathbf{I}}$	: Inertia Tensor
L, M, N	: Primary, Secondary, and Tertiary Scalar Moments
$\mathbf{T}$	: Transformation Matrix
$\mathbf{Q}$	: Unit Quaternion - 4 by 1 Column Vector
q_0	: Quaternion Scalar Element
$\mathbf{q}$	: Quaternion Vector
$\mathbf{I}_{N\times N}$	: N element by N element Identity Matrix

Superscripts and Subscripts

*	: Quaternion Conjugate
^{T}	: Transpose of Matrix or Vector
$_{veh}$	: Relative to Vehicle Coordinate Frame
$_{ref}$	: Relative to Reference or Inertial Coordinate Frame
$_{R2V}$	: Reference Frame to Vehicle Frame
$_{V2R}$	: Vehicle Frame to Reference Frame

$_{i}$: Relating to "ith"Accelerometer of Accelerometer Array
$_{Imp}$: Imposed Translational (Inertial) Loading due to Vehicle Maneuvers
$_{Man}$: Angular Displacement due to Vehicle Maneuvers
$_{Z,CG}$: Mounting at the center of gravity of the vehicle along the vehicle tertiary axis
$_{z,i}$: "ith"accelerometer measuring acceleration relative to the vehicle's tertiary axis

Mathematical Operators

$|x|$: Scalar or Vector Magnitude $= \sqrt{x_1^2 + \cdots + x_n^2}$
$\bullet$: Dot Product
$\times$: Cross Product or designation of Matrix rows and Columns
$*$: Multiplication
$S\varphi$: Sine of φ
$C\varphi$: Cosine of φ

Note: Unless otherwise stated, boldface variables represent vectors or matrices and italicized variables represent scalars.

Chapter 1

Introduction

1.1 Background

Precise execution of vehicle maneuvers during mission operations requires accurate and up-to-date estimates of a vehicle's attitude in three-dimensional space. Reliable attitude estimation requires constant assessment of noisy measurements relative to the vehicle's center of gravity or relative to a fixed point of reference. Fusion of both types of sensors along with knowledge of vehicle dynamics aids in reducing sensor noise yielding the most accurate solution for vehicle attitude determination.

Measurement of motion relative to the vehicle is exemplified by a rate sensor, angular or translational, and produces instantaneous accurate measurements in the short term but is not reliable over a large time scale. Measurement of motion relative to a fixed point of reference, often the center of the earth, is exemplified by displacement or magnetic field direction sensors. These sensors, called inertial sensors due to their reference to a datum quantity, possess long term accuracy with the trade-off of short term unreliability if the vehicle experiences rapid chaotic movement. Examples of sensors measuring inertial quantities are accelerometers, magnetometers, and GPS while rate gyroscopes are examples of vehicle relative motion sensors. Fusion of both types of sensors yields the most accurate solution for vehicle attitude determination.

When operating in real-world environments, measuring movement accurately proves difficult due to inherent sensor biases or signal noise generated by surrounding hardware or the operating environment. These error sources possess the ability to change over time therefore sensor output signal must be constantly monitored. Signals used for attitude estimation left unchecked or unfiltered may lead to large departures from the vehicle's true attitude. For example, integration of a minute error in a rate gyro signal for determination of an attitude estimate results in a deviation from the vehicle's true angular

displacement, referred to as drift. Rate gyro precision can be increased with trade-offs consisting of increased cost and weight, making it infeasible for many unmanned vehicle and robotic applications. Current methods to estimate and eliminate bias effects employ the use of magnetic field sensors or GPS receivers along with a reference system model to reduce and eliminate rate gyro drift. Due to various anomalies in the Earth's magnetic field and radio interference or jamming, magnetomer and GPS data may be unreliable or nonexistent. The use of system models in either a Kalman Filter or recursive least-squares routine is a common practice within the aerospace industry for onboard attitude estimation but requires accurate knowledge of a system's operation to produce a linear or linearized model for implementation.

This work expands on a prior proposed device [7] composed of a rate gyro and one-axis accelerometers by augmenting it with two additional accelerometers and a new attitude determination algorithm for use in nonlinear systems such as aircraft. The system is able to estimate and eliminate rate gyro bias in real-time during both dynamic maneuvers and static or trim conditions resulting in accurate attitude tracking. Proof of concept will include implementation of the device in a linear model and nonlinear aircraft model executing longitudinal maneuvers with sensor biases and noise present. The new system's effectiveness will be demonstrated by the comparison of the estimated and true vehicle attitude along with the estimated and true rate gyro bias. This study is the first step toward the end goal of precise and reliable three dimensional attitude estimation using cost-effective sensors coupled with a low computational burden for application in small unmanned vehicles and robotics without relying on corruptible GPS or magnetometer measurements.

1.2 Technology and Current Work

Identification of sensor bias and filtering of sensor output is vital to feedback control law development for accurate control of all systems. A commonly used model in the aerospace industry for biased and noise corrupted rate gyro data is documented in [17] initially developed by Farrenkopf in 1974, [9], and is reiterated throughout literature published since due to its simplicity and effectiveness in modeling gyro behavior. The measurement model is displayed below in Equation 1.1 and again in Section 2.3.1

$$\begin{array}{rcccccc} \textit{measured value} & = & \textit{true value} & + & \textit{measurement noise} & + & \textit{bias} \\ \tilde{\mathbf{x}} & = & \mathbf{x} & + & \nu(t) & + & b(t) \end{array} \tag{1.1}$$

Offline sensor bias estimation either before or after system implementation has been conducted in [2, 12, 14], but this method of analytically determining the sensor bias is not immediately useful and is subject to batch state estimation errors. The end result being general trending instead of precise estimation. The need for online accurate bias

estimation is crucial in real-time operation of unmanned vehicles. Sensor measurement may vary with operating environment or from sensor degradation which offline estimation cannot account for unless testing includes such variations usually infeasible.

Kalman Filtering has long been used in the aerospace industry for accurate online attitude estimation of satellites pairing noise or bias corrupted gyros and other noise corrupted attitude sensors with a linear or linearized state-space system model [17]. The main Kalman Filter limitations include need for a linear dynamic system model or the need to constantly re-linearize the nonlinear system model about the previous state vector and statistical information about the sensor measurements to achieve an optimal convergence time, seconds compared to minutes or hours. A large system model exposes the computation burden of the Kalman Filter exists where its recursive least-squares nature is displayed when matrix inverses as well as matrix multiplication are required. If the attitude estimate lies in the Quaternion instead of the Euler domain, an additional burden is imposed because the Euler vector contains three elements whereas the Quaternion contains four elements with the additional constraint of having a unity magnitude [16, 22]. However, the Kalman Filter is extremely effective and is shown to be the optimal filter for linear applications [27] and its computational burden can be reduced to simple mathematical operations for systems with only a few states. In addition, the stochastic nature of the Kalman Filter allows for solution convergence in real-world applications possessing corrupted sensor data causing other less flexible algorithms to diverge.

Fusion of sensor data in both the vehicle frame and absolute frame is required to calculate a reliable attitude estimate since the vehicle is commanded in vehicle frame but commands are governed by its position and orientation in an absolute frame of reference. The Kalman Filter utilized in the aerospace industry is the nonlinear form known as the Extended Kalman Filter, EKF. This form is used in conjunction with a rate gyro, short-term accurate vehicle frame rate sensor, and at least two other long-term accurate reference frame sensors measuring difference absolute quantities, accelerometer and magnetometer or magnetometer and GPS sensor for example [28]. The combination of a relative sensor with two inertial sensors is synergistic relating the vehicle orientation in the vehicle frame to the absolute frame of reference via a 3 by 3 orthogonal rotation matrix. A more complex filter is required for implementation of multiple inertial sensors to aid in estimation of the gyro bias because of the introduction of additional inertial sensor errors that cannot always be compensated for *a priori*.

1.2.1 Inertial Sensor Capabilities

Inclinometers

For elimination of rate gyro drift in the pitch or roll axis, an inclinometer can be paired with a rate gyro. The inclinometer makes use of an encapsulated air bubble in a liquid with a known resistance between two electrodes when the vial is perpendicular to the local gravity vector. When the vial is tilted about the sensing axis, the voltage between the electrodes changes and is used to estimate pitch or roll angle. These units have inherently slow dynamics due to the need to wait for the bubble to stop moving within the vial so the attitude can be accurately determined from measuring the resistance between the two electrodes. In addition, inclinometers are sensitive to translational shock and vibration loads leading to unreliable measurement. Shock and vibration resistant inclinometers are available but are expensive and have a relatively large space requirement compared with other sensors such as accelerometers as documented in [6]. A rate gyro was paired with inclinometers on a walking robotic platform in [25] for producing accurate attitude observation in a nonlinear system using cost-effective sensors. This research showed inclinometers posses a significant time lag resulting in less accurate attitude tracking even when the research was conducted using only small angle departures from the static condition. Akella et. al. in [3] published results of an attitude estimator more accurate and robust than [25] over a wider range of maneuver angles. The induced error from the gyro bias was reduced by not integrating the gyro measurements resulting in an estimator that could not determine the gyro bias online. This research like [25] was predicated on utilizing the vehicle's tensor of inertia in the Euler equations of motion yielding the consequence of induced error if an inaccurate tensor was used.

Magnetometers

For faster measurement updates with additional measurement on all three axes, magnetometers can be implemented in the attitude estimator. Magnetometers can be paired with a rate gyro for vehicle attitude because the angle between the Earth's magnetic field and the particular axis of the vehicle can be measured in both magnitude and direction. Magnetometers are used extensively to provide bounds to attitude determination error in many unmanned aircraft because of their long term reliability. However, magnetometers must be paired with other sensors measuring another reference, such as gravity, because the vehicle axis can lie anywhere on the surface of a cone of semi-angle equal to the sensed angle about the magnetic field vector. Magnetometers are susceptible to large errors when encountering magnetic anomalies arising from changes in the Earth's magnetic field, presence of ferromagnetic material, or changing fields associated with the vehicle's power electronics or instrumentation. Thus, the sensor is required to be mounted at the extremities of the vehicle far from internal interference and needs to have a region's magnetic anomalies well mapped. Magnetometers in aircraft performing many a roll

maneuver are susceptible to attitude error because the rolling motion produces an alternating magnetic field, giving rise to the need of incorporation of a sensor knowing the vehicle is rolling. [31]

Global Position System - GPS

Global Positioning System, GPS, receivers are often utilized to correct vehicle position errors brought about by sensor signal corruption. The system was originally designed for terrestrial and low-altitude applications but has been implemented in marine operations, high altitude atmospheric measurements and attitude determination. GPS signals can be converted into translational position and velocity estimates, however a minimum of four satellites is needed for defining the vehicles attitude. GPS signals are electro-magnetic, EM, waves and phase modulated, PM, signals decoded by the receiver with the military receiving high precision position estimation and the commercial public receiving lower precision estimates. Depending on the operating environment, the GPS signal can be either jammed or nonexistent because of the nature, e.g. underwater or cave operating environment, and transmission structure of the signal. An example of intentional interference is when the Department of Defense intentionally dithers the signal, resulting in degradation of position in real-time. Additional GPS errors result from signal noise, bias, and mistakes resulting in errors of 0.5 meters up to hundreds of kilometers. [1]

Accelerometers

Accelerometers are susceptible to noise resulting from vibration or from uncompensated inertial loading of the vehicle. Integrated circuit accelerometers are the most cost effective of the different types and are small enough to be easily isolated from vehicle vibration but possess an upper limit operation temperature due to their micromachined construction [6]. Vehicle inertial loads due to dynamic maneuvers can be compensated for by using several accelerometers and comparing their signals or not using the accelerometer during the dynamic maneuver. The fusion of a single rate gyro and three-axis accelerometers using a Kalman Filter has been employed in walking robots requiring accurate attitude estimation while being subjected to accelerated motion [26]. However, the accelerometer sensors are not always used if the signal becomes saturated, within a certain threshold of $\pm$ 9.81m/s^2 or 1 gee. This results in gyro reliance during periods of accelerated movement causing increased error in attitude estimation as accelerated motion continues until the robot motion falls back into the unaccelerated regime. The algorithm implemented on the robotic platform relied upon implementation of a linear system dynamics with two linear Kalman Filters to estimate attitude of a nonlinear system. Kingston in [15], expresses how navigation grade gyro are too large to be flown in small unmanned air vehicles and micro air vehicles. Thus giving rise to attitude determination research conducted using accelerometers and GPS paired with a rate gyro and using the Quaternion form of the EKF for a non-accelerating body. Kingston's research serves as a comparison to the

work proposed in this thesis since simulated signal noise characteristics and deviation of estimate from truth results are explicitly stated.

1.2.2 Inertial and Relative Sensor Pairing

Estimation of the transformation matrix and gyro bias in a nonlinear Vertical Take-Off and Landing Unmanned Aerial Vehicle, VTOL-UAV, through use of two nonlinear complementary filters is introduced in [19]. The nonlinear aspects of motion were preserved making attitude estimation more accurate unlike EKF, requiring linearization of the nonlinear system model, however tuning of the complementary filters was still required. Estimation of the gyro bias on one axis resulted in the need for two absolute sensors each mounted along separate axes. The design of VTOL UAV played a key role in attitude estimation accuracy due to its ducted-fan design subjected to quasi-stationary flight in an indoor environment allowing for reliable magnetometer and accelerometer data.

Accurate longitudinal attitude tracking and online estimation of a rate gyro bias using a rate gyro and a series one axis using accelerometers mounted in the plane perpendicular to gyro measurement was proposed in [7] to combat the problems of unreliable GPS, magnetometer, and inclinometer sensor data. Additionally, a less computationally expensive bias calculation is considered when pairing the rate gyro with low-cost accelerometers placed at known orientations. This arrangement allows for continual bias estimation during static conditions and discrete bias estimation during dynamic maneuvers due to accelerometer signal vector similarities. To produce continual attitude tracking during dynamic maneuvers the calculated bias is subtracted from the continuous rate gyro signal until the next discrete bias estimation can occur. This research presents a novel way to estimate the gyro bias and vehicle attitude during dynamic maneuvers without the use of different sensors or extremely complex filtering. However, this study assessed only a purely rotating operating environment for a terrestrial robotic platform with only gravity as the imposed inertial loading.

Instead of modeling the complete nonlinear system and focusing on sensor operation [10] demonstrates the power a a linear discrete time Kalman Filter to estimate a rate gyro bias and the vehicle's attitude using known sensor noise variances along with the gyro sensor model shown in Equation 1.1. This rate gyro bias and attitude estimator can be implemented using the quaternion instead of Euler attitude formation as is common in the aerospace industry shown by [17]. By resetting the rate gyro integration initial conditions using the output from the Kalman Filter at the discrete trigger points during dynamic maneuvers and continuously during trim conditions, a more robust and accurate estimator of longitudinal attitude and gyro bias can be developed.

1.3 Overview and Motivation for Present Work

The following research is concerned with development of a longitudinal attitude determination device able to identify and eliminate effects of a rate bias using accelerometers thereby producing an accurate estimation of object orientation in real-time. Expansion on prior work of the proposed concept will include implementation of the device in a nonlinear aircraft model simulating longitudinal maneuvers. The device will provide online estimation of the rate gyro bias without reliance on knowledge of the vehicle plant model, or additional inertial sensing either through a global positioning system datalink, or magnetometer.

The device layout consists of 13 accelerometers evenly spaced about a semi-circular arc with the rate gyro at the arc's origin. The locations of the accelerometers from the vehicle's axes are utilized by the algorithm to estimate the rate gyro bias and the vehicle's attitude. Figure 1.1 displays the proposed device with the rate gyro measuring rotation about the axis pointing out of the page. The vehicle's primary axis is considered to be the horizontal vector.

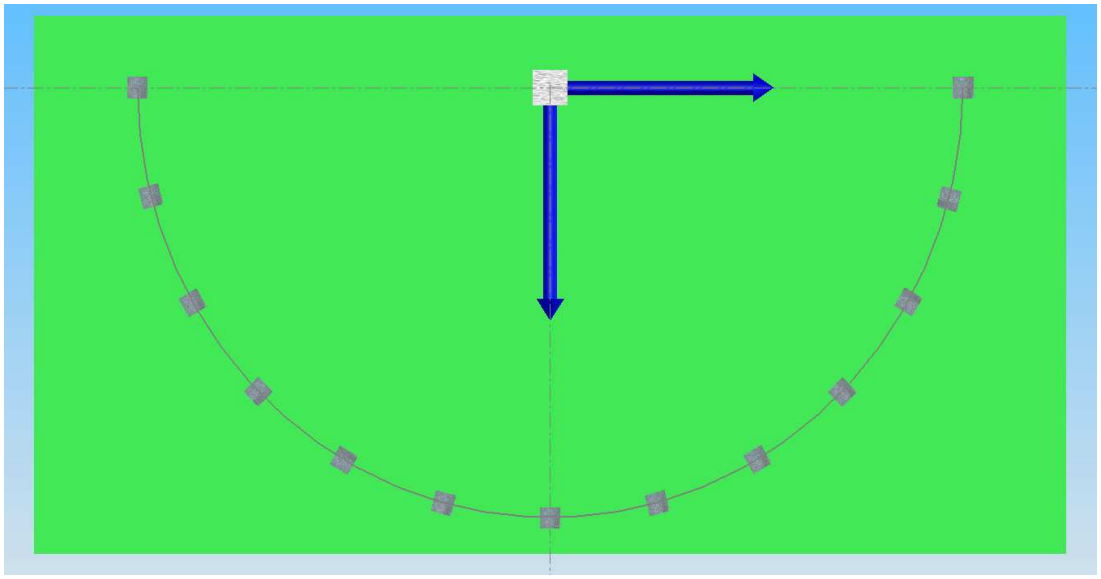

Figure 1.1: Device Front View

The above device is utilized for bias and attitude estimation both during static conditions and dynamic maneuvers. During static conditions, dictated by the filtered derivative of the rate gyro, the measurements from the accelerometers are used to continually reinitialize the rate gyro's integration initial conditions allowing for continuous bias and attitude estimation. During dynamic maneuvers, the rate gyro can be estimated at discretely triggered points where the signal difference of two adjacent accelerometers is below a set threshold. At these trigger points the integration initial conditions are reset and the

calculated bias is continually subtracted from the rate gyro signal until the next dynamic trigger or the vehicle enters static operation.

The device and bias estimation algorithm will be tested and compared with the true, simulated, attitude using a simulation that incorporates nonlinear dynamics, sensor biases, and sensor noise modeled in Simulink®with data analysis conducted in MATLAB®. The general structure for this research is as follows:

1. Develop a nonlinear aircraft model capable of producing an accurate simulation of real-world aircraft maneuvers.

2. Develop an accurate online rate gyro bias computation algorithm utilizing the rate gyro and accelerometer device.

3. Implement rate gyro and accelerometer device, simulated open-loop hardware observer, within the nonlinear aircraft model along with rate gyro sensor noise and bias and accelerometer noise too simulate longitudinal aircraft maneuvers.

4. Analyze and compare the device results with the true attitude of the simulation.

Chapter 2

Background Theory

Preface

This chapter provides the necessary rigid body motion, signal filtering, and bias estimation background for simulation development of the proposed device and the simulated operation environments.

2.1 Rigid Body Dynamics

2.1.1 Attitude Representation Convention

Rigid body angular and translation displacement with respect to a fixed, reference, coordinate system within a Cartesian space is described by six parameters, three in translation and three in rotation. Translation displacement along the three reference coordinate system axes represents the vehicle position while the traditional vehicle attitude is represented by the angular displacement, Euler Angles, about the reference system axes. Describing a body's position and orientation requires use of two right-handed coordinate systems or frames, one fixed and the other free to move and rotate about the fixed, inertial, coordinate system.

The coordinate system fixed to the vehicle body is referred to as "body fixed"with its origin typically at the center of gravity of the body. The body fixed coordinate system rotates and translates about the stationary reference coordinate system. The Earth Center coordinate system uses the center of the Earth as the origin of the reference system and is commonly used for orbital mechanics or globe circumnavigation applications. The Earth Fixed coordinate system is commonly used with its origin at local ground level. The primary axis for the Earth fixed coordinate system is taken to be pointing to geographic North, the secondary axis is oriented along East, and the tertiary axis oriented

parallel with the local gravity vector. The Euler displacement angles about the fixed coordinated system are referred to as Bank, Elevation, and Heading, respective to the primary, secondary, and tertiary axes. For the body fixed coordinate system, the primary, roll, axis is oriented along the long axis of the aircraft with the secondary, pitch, axis extending out the starboard side of the aircraft, and the tertiary, yaw, axis extending in the direction of the cross product of the primary and secondary axes. The origin of the body coordinate system is typically taken to be the vehicle's center of gravity. Figure 2.1 provides visual representation of a fixed, inertial, coordinate system and a vehicle reference system. Table 2.1 provides a shorthand reference for axis designation, position, angle, and angular rate.

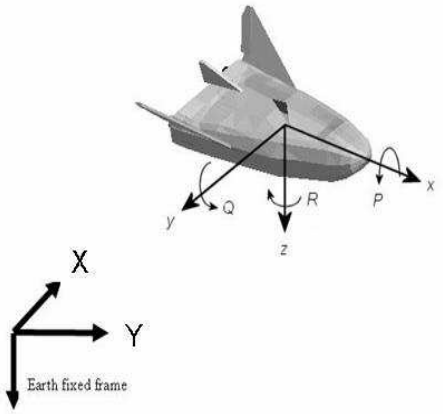

Figure 2.1: Earth Fixed and Body Fixed Coordinate System [18]

Parameter \ Axis	Primary Axis		Secondary Axis		Tertiary Axis	
	Earth	Body	Earth	Body	Earth	Body
Designation	X_{ref}	X_{veh}	Y_{ref}	Y_{veh}	Z_{ref}	Z_{veh}
Position	S_X	s_x	S_Y	s_y	S_Z	s_z
Velocity	V_X	u	V_Y	v	V_Z	w
Angle, φ	ϕ_E	ϕ_b	θ_E	θ_b	ψ_E	ψ_b
Angular Rate, ω	$\dot{\phi}$	p	$\dot{\theta}$	q	$\dot{\psi}$	r

Table 2.1: Coordinate System Definitions

In addition to the traditional handling of aircraft attitude by resolving the vehicle displacement angles to Euler displacement angles via the directional cosine matrix, attitude descriptors such as the Euler Axis Formulation and the Euler-Rodrigues Quaternion Formulation should be considered [22, 28]. Other attitude descriptors in transferring vehicle

angular displacement rates to the reference axes displacement rates are needed due to the Gimbal Lock situation. A vehicle achieving a pitch angle of 90 degree positive or negative from its primary reference axis is subject to Gimbal Lock. In this orientation, vehicle rates cannot be resolved to the reference coordinate system and integrated to find bank and heading angle due a divide by zero error arising from the vehicle to reference rate transformation matrix. The physical interpretation of this phenomena is that when the vehicle conducts such a pitch maneuver, the roll axis and yaw axis become parallel and the vehicle yaw is no longer able to be sensed. This situation arises in the traditional three gimbal Inertial Measurement Unit assembly, due to its reliance on the Euler Angle convention for vehicle attitude sensing. To remedy this situation, a fourth gimbal is added to maintain separation between the pitch and yaw gimbals.

The Gimbal Lock situation is resolved mathematically by also adding a fourth element to the attitude description. The Euler Axis Formulation describes the motion of the vehicle reference frame to the inertial reference frame by using a single rotation angle about a particular unit vector, Euler axis or eigenaxis. However, even though the Gimbal Lock situation is resolved, a singularity in integration of the eigenaxis and eigenangle exists when the eigenangle is either 0 or 180 degrees. This situation arises when the primary vehicle axis is parallel with the ground and is heading either North or South. The primary way of dealing with simulation or computation when encountering Gimbal Lock in the aerospace community is through use of the Euler-Rodrigues Quaternion Formulation. The quaternion uses four elements and is derived from the eigenaxis formulation. [22, 28]. The Quaternion is utilized in this work to assess angular displacement changes and rates of change in calculation of the rate gyro bias.

2.1.2 Rigid Body Application of Newton's Second Law [21, 33]

For appropriate simulation of a nonlinear aircraft in three dimensions, Newton's Second Law is applied for force and moment resolution. Proper application of Newton's Second Law requires the summation of external forces on a body be equal to the body's time rate change of momentum and the summation of moments be equal to the body's time rate change of angular momentum, as shown in Equations 2.1 and 2.2.

$$\sum \mathbf{F} + \mathbf{W} = \frac{d}{dt}\left(m\mathbf{V}\right) \tag{2.1}$$

$$\sum \mathbf{M} = \frac{d}{dt}\left(\vec{\omega}\overleftrightarrow{\mathbf{I}}\right) \tag{2.2}$$

Where $\mathbf{F}$ is the net force vector on the body, $\mathbf{W}$ is the weight vector of the body,$\mathbf{V}$ is the translational rate vector, $\mathbf{M}$ is the net moment vector about the coordinate frame origin, $\overleftrightarrow{\mathbf{I}}$ is the inertia tensor, and $\vec{\omega}$ is the angular rate vector. These vectors and tensor are with respect to the vehicle's body frame with the origin taken at the vehicle's center of

gravity, CG. Thus, the Inertia tensor is defined by Equations 2.3, 2.4 and 2.5.

$$\overleftrightarrow{\mathbf{I}}_{veh} = \begin{bmatrix} I_{xx} & -I_{xy} & -I_{xz} \\ -I_{yx} & I_{yy} & -I_{yz} \\ -I_{zx} & -I_{zy} & I_{zz} \end{bmatrix} \tag{2.3}$$

$$I_{\substack{ij \\ i \neq j}} = \iiint_m \left(i^2 + j^2\right) dm \tag{2.4}$$

$$I_{ii} = \iiint_m \left(j^2 + k^2\right) dm \tag{2.5}$$

From Equation 2.4, the Inertia tensor is symmetric about its diagonal. Using the general convention for development of a body reference system, vehicles are typically symmetric about the plane formed by the primary and tertiary axes, x and z, and there is a negligible contribution of inertia about the plane formed by the primary and secondary, x and y, axes compared to that of the diagonal terms of the tensor. Thus, $I_{xy}, I_{yx}, I_{yz},$ and I_{zy} terms are generally set to 0. For the research conducted, this generalization was not implemented in order to produce a more accurate simulation of the aircraft.

Equations 2.1 and 2.2 are defined for motion in one coordinate system, i.e. the vehicle's body frame. To relate the vehicle's motion in body frame to inertial frame, the rate of change of body frame vector $\mathbf{G}_{veh}$ possessing an angular velocity vector, $\vec{\omega}$, can be related to a reference frame vector $\mathbf{G}_{ref}$ by Equation 2.6. [33]

$$\frac{d}{dt}\mathbf{G}_{ref} = \frac{d}{dt}\mathbf{G}_{veh} + \vec{\omega} \times \mathbf{G}_{veh} \tag{2.6}$$

Equation 2.6 is applied to Equations 2.1 and 2.2 resulting in Equations 2.7 and 2.8. These equations relate the force and moment experienced by the vehicle to the inertial frame of reference.

$$\sum \mathbf{F}_{ref} + \mathbf{W}_{ref} = \frac{d}{dt}\left(m\mathbf{V}_{veh}\right) + \vec{\omega} \times \left(m\mathbf{V}_{veh}\right) \tag{2.7}$$

$$\sum \mathbf{M}_{ref} = \frac{d}{dt}\left(\vec{\omega}\,\overleftrightarrow{\mathbf{I}}_{veh}\right) + \vec{\omega} \times \left(\vec{\omega}\,\overleftrightarrow{\mathbf{I}}_{veh}\right) \tag{2.8}$$

The scalar forms of Equations 2.7 and 2.8 for calculation of the net force and moment terms are given below in Equations 2.9 and 2.10.

$$\begin{Bmatrix} F_X \\ F_Y \\ F_Z \end{Bmatrix}_{ref} = \begin{Bmatrix} m\left(\dot{u} - vr + wq\right) \\ m\left(\dot{v} + ur + wp\right) \\ m\left(\dot{w} - uq + vp\right) \end{Bmatrix} = \mathbf{W}_{ref} + \mathbf{F}_{Aerodynamic} + \mathbf{F}_{Thrust} \tag{2.9}$$

$$\mathbf{M}_{ref} = \left\{ \begin{array}{c} L \\ M \\ N \end{array} \right\} = \left\{ \begin{array}{c} \dot{p}I_{xx} - \dot{q}I_{xy} - \dot{r}I_{xz} \\ -\dot{p}I_{xy} + \dot{q}I_{yy} - \dot{r}I_{yz} \\ -\dot{p}I_{xz} - \dot{q}I_{yz} + \dot{r}I_{zz} \end{array} \right\} =$$

$$\left\{ \begin{array}{c} qr\left(I_{yy} - I_{zz}\right) + \left(q^2 - r^2\right) I_{xy} - prI_{xy} + pqI_{xz} \\ pr\left(I_{zz} - I_{xx}\right) + \left(r^2 - p^2\right) I_{xz} - pqI_{yz} + qrI_{xy} \\ pq\left(I_{xx} - I_{yy}\right) + \left(p^2 - q^2\right) I_{xy} - qrI_{xz} + prI_{yz} \end{array} \right\} + \mathbf{M}_{external} \tag{2.10}$$

Equation 2.9 accounts for forces resulting from aerodynamic and propulsive forces and Equation 2.10 accounts for additional moments arising from the aerodynamic and propulsive forces. The thrust force on the aircraft is assumed to be present along the primary vehicle axis only for the conducted simulations. The governing nonlinear six degree-of-freedom equations for spacecraft and aircraft flight are well known and documented [21, 22, 28] with Appendix F providing the additional force and moment equations along with the stability derivatives for the particular aircraft used in the nonlinear plant model simulations.

2.1.3 Euler Kinematics [21, 22]

For correct determination of a body's orientation with respect to the Earth fixed coordinate system, a coordinate transform between body and Earth coordinate systems is required. This is achieved through Euler angle rotations about the Earth fixed coordinate system in a specific sequence whose order is important. This work uses the "aerospace"or "3-2-1 "sequence for Earth fixed to body fixed transformation. Equations 2.11, 2.12, and 2.13 define rotations about the primary, secondary, and tertiary reference axes to the vehicle's primary, secondary, and tertiary axes respectively. These relationships are derived in Appendix A.

$$R1 = \left[\begin{array}{ccc} 1 & 0 & 0 \\ 0 & \cos\phi & \sin\phi \\ 0 & -\sin\phi & \cos\phi \end{array} \right] \tag{2.11}$$

$$R2 = \left[\begin{array}{ccc} \cos\theta & 0 & -\sin\theta \\ 0 & 1 & 0 \\ \sin\theta & 0 & \cos\theta \end{array} \right] \tag{2.12}$$

$$R3 = \left[\begin{array}{ccc} \cos\psi & \sin\psi & 0 \\ -\sin\psi & \cos\psi & 0 \\ 0 & 0 & 1 \end{array} \right] \tag{2.13}$$

With these relationships, Equation 2.14 defines the transformation matrix, T_{R2V}, from fixed inertial frame to vehicle body frame. Equation 2.15 gives the transformation equation for translational movement from inertial frame to vehicle frame.

$$\mathbf{T}_{R2V} = R1 * R2 * R3 \tag{2.14}$$

$$\mathbf{S}_{veh} = \mathbf{T}_{R2V} * \mathbf{S}_{ref} = \begin{bmatrix} C\theta C\psi & C\theta S\psi & -S\theta \\ S\phi S\theta C\psi - C\phi S\psi & S\phi S\theta S\psi + C\phi C\psi & S\phi C\theta \\ C\phi S\theta C\psi + S\phi S\psi & C\phi S\theta S\psi - S\phi C\psi & C\phi C\theta \end{bmatrix} * \mathbf{S}_{ref} \quad (2.15)$$

$$\textit{Note: } C\varphi = \cos(\varphi) \textit{ and } S\varphi = \sin(\varphi)$$

The transformation matrix in Equation 2.15 is known as the Direction Cosine Matrix or DCM. Due to the nature of the inverse of square orthogonal matrices, the transformation matrix from vehicle frame to inertial frame is the transpose of Equation 2.14, yielding Equation 2.16 and giving Equation 2.17 for transference of vehicle translational motion to the inertial frame.

$$\mathbf{T}_{V2R} = R3 * R2 * R1 \quad (2.16)$$

$$\mathbf{S}_{ref} = \mathbf{T}_{V2R} * \mathbf{S}_{veh} = \begin{bmatrix} C\psi C\theta & -S\psi C\phi + C\psi\ S\theta S\phi & S\psi S\phi + C\psi S\theta C\phi \\ S\psi C\theta & C\psi C\phi + S\psi S\theta S\phi & S\psi S\theta C\phi - C\psi S\phi \\ -S\theta & C\theta S\phi & C\theta C\phi \end{bmatrix} * \mathbf{S}_{veh} \quad (2.17)$$

Transference of translational rates in inertial frame to vehicle rates follows Equation 2.15 with the rate vectors taking the place of the displacement vectors. Transference of vehicle translational rates to inertial rates utilizes Equation 2.17 with rate vectors replacing position vectors in addition to wind components in inertial frame, this yields Equation 2.18

$$\mathbf{V}_{ref} = \mathbf{T}_{V2R} * \mathbf{V}_{veh} + \mathbf{V}_{wind} \quad (2.18)$$

The relationship between Euler angular rates and vehicle rates is derived for Aerospace 3-2-1 rotation sequence, Appendix A, and is given by Equation 2.19

$$\begin{Bmatrix} p \\ q \\ r \end{Bmatrix} = \begin{bmatrix} 1 & 0 & -\sin\theta \\ 0 & \cos\phi & \cos\theta\sin\phi \\ 0 & -\sin\phi & \cos\theta\cos\phi \end{bmatrix} \begin{Bmatrix} \dot{\phi} \\ \dot{\theta} \\ \dot{\psi} \end{Bmatrix} \quad (2.19)$$

Equation 2.19 can be solved for transferring vehicle angular rates to inertial angular rates and is given by Equation 2.20

$$\begin{Bmatrix} \dot{\phi} \\ \dot{\theta} \\ \dot{\psi} \end{Bmatrix} = \begin{bmatrix} 1 & \sin\phi\tan\theta & \cos\phi\tan\theta \\ 0 & \cos\phi & -\sin\phi \\ 0 & \sin\phi\sec\theta & \cos\phi\sec\theta \end{bmatrix} \begin{Bmatrix} p \\ q \\ r \end{Bmatrix} \quad (2.20)$$

By integration of either Equation 2.19 or 2.20, the total angular displacement over time can be calculated for the coordinate system of interest. Equation 2.20 demonstrates the Gimbal Lock phenomena with a divide by zero error at $\theta = \pm 90\,\text{deg}$ where the bank and

heading angles are unable to be computed due to the parallel alignment of the roll and pitch axes.

To alleviate the problem of Gimbal Lock in transferring vehicle angular rates to inertial frame angle rates, Euler(1775) proposed the use of a single rotation through an angle Θ about a particular axis called the *Euler Axis* or *Eigen Axis*[22]. This Formulation gives rise to a four element vector with one element being the total rotation angle, Θ, and the other elements being a vector with unit magnitude, $\mathbf{E}$, that is rotated about. The Euler Axis unit vector, $\mathbf{E} = [E_x \ E_y \ E_z]^T$, eliminates redundancy because it describes only one axis to rotate about. Figure 2.2 displays the Eigenvector and total rotation angle for an arbitrary vehicle orientation.

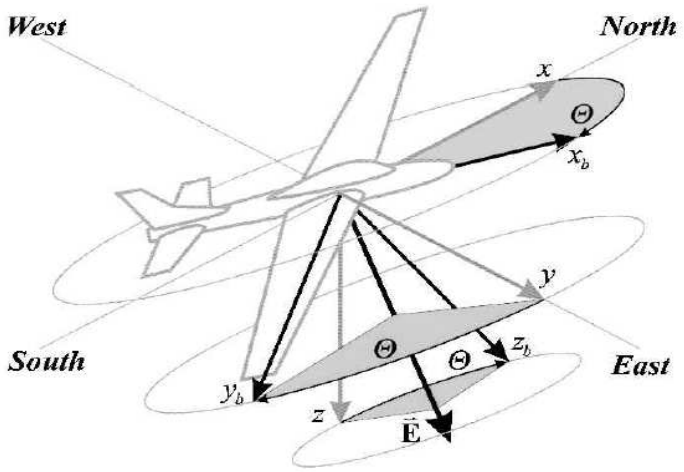

Figure 2.2: Arbitrary Orientation Euler Axis and Total Rotation Angle [23]

Euler Axis Vector possesses the same components in both inertial and vehicle frame during rotation. The components of an arbitrary vector, $\mathbf{G}$, in vehicle frame can be related to inertial frame through *Euler's Formula* given by Equation 2.21

$$\mathbf{G}_{inertial} = \begin{bmatrix} E_{xx} + \cos\Theta & E_{xy} - E_z \sin\Theta & E_{xz} + E_y \sin\Theta \\ E_{xy} + E_z \sin\Theta & E_{yy} + \cos\Theta & E_{yz} - E_x \sin\Theta \\ E_{xz} - E_y \sin\Theta & E_{yz} + E_x \sin\Theta & E_{zz} + \cos\Theta \end{bmatrix} * \mathbf{G}_{vehicle} \qquad (2.21)$$

$$Note: \ E_{ij} = E_i E_j \left(1 - \cos\Theta\right)$$

The inverse of the transformation matrix in Equation 2.21 transforms an arbitrary vector from inertial frame to vehicle frame. Again, note the orthogonality of square matrices allows the transform from inertial to vehicle frame to be the transpose of the transformation matrix from vehicle to inertial frame. The time rate change of the Euler Axis parameters is calculated from the vehicle angular rates and a 12 element transformation

matrix shown in Equation 2.22

$$\begin{Bmatrix} \dot{\Theta} \\ \dot{E}_x \\ \dot{E}_y \\ \dot{E}_z \end{Bmatrix} = \frac{1}{2} \begin{bmatrix} 2E_x & 2E_y & 2E_z \\ E'_{xx} + \cot\frac{\Theta}{2} & E'_{xy} - E_z & E'_{xz} + E_y \\ E'_{xy} + E_z & E'_{yy} + \cot\frac{\Theta}{2} & E'_{yz} - E_x \\ E'_{xz} - E_y & E'_{yz} + E_x & E'_{zz} + \cot\frac{\Theta}{2} \end{bmatrix} \begin{Bmatrix} p \\ q \\ r \end{Bmatrix} \tag{2.22}$$

$$\textit{Note: } E'_{ij} = -E_i E_j \cot\frac{\Theta}{2}$$

From Equation 2.22, the Gimbal Lock situation has been resolved only to have a new singularity arise, when $\Theta = 0\,\text{deg}$ or $180\,\text{deg}$. This situation arises when the vehicle's fuselage is parallel with the ground and is heading either due North or due South.

2.1.4 The Quaternion

Quaternions are commonly used in the aerospace industry as attitude descriptors since the formulation is free of any orientation singularities. Additionally, the quaternion has been proven to be the attitude representation requiring the least number of elements to produce linear kinematic equations for a nonlinear system. [23]

Quaternion Attitude Formulation [16]

Quaternions are related to the Euler Axis parameter via a manipulation of variables shown in Equation 2.23.

$$\mathbf{Q} = \begin{Bmatrix} q_0 \\ q_1 \\ q_2 \\ q_3 \end{Bmatrix} = \begin{Bmatrix} \cos\frac{\Theta}{2} \\ E_x \sin\frac{\Theta}{2} \\ E_y \sin\frac{\Theta}{2} \\ E_z \sin\frac{\Theta}{2} \end{Bmatrix} = q_0 + q_1\mathbf{i} + q_2 + \mathbf{j} + q_3\mathbf{k} = \begin{Bmatrix} q_0 \\ \mathbf{q} \end{Bmatrix} \tag{2.23}$$

Just as with the Euler Axis vector, $\mathbf{E}$, the four components of the Quaternion, $\mathbf{Q}$, are not altered due to a coordinate transformation because the Quaternion vector, $\mathbf{q}$, is directed along the Euler Axis. The first element of the Quaternion is a scalar with the other three components forming the Quaternion vector. Since there are four parameters governing three axes of rotation, the mathematical redundancy must be eliminated. This is done by looking at the square of the magnitude of the Quaternion and noting that $\cos(\varphi)^2 + \sin(\varphi)^2 = 1$, and remembering $\mathbf{E}$ is a unit vector, shown in Equation 2.24.

$$\begin{aligned} |\mathbf{Q}|^2 = q_0^2 + q_1^2 + q_2^2 + q_3^2 &= \cos\left(\frac{\Theta}{2}\right)^2 + \left(q_1^2 + q_2^2 + q_3^2\right)\sin\left(\frac{\Theta}{2}\right)^2 \\ &= q_0^2 + q_1^2 + q_2^2 + q_3^2 = 1 \end{aligned} \tag{2.24}$$

Preliminary Quaternion Mathematics [22, 28]

All elements of the quaternion are real numbers even with designation as a hypercomplex number. Addition of two quaternions is performed by adding their corresponding components and multiplication of a quaternion by a scalar constant is performed by multiplying each component by the scalar constant. These properties are demonstrated in Appendix B.

For attitude calculations, namely angular displacements, the difference of two quaternions does not give the overall rotation angle and multiplying by a scalar factor does not change the rotation angle because the quaternion must always be normalized or else it has no meaning in attitude estimation. Differencing and Normalizing quaternions involves use of the quaternion conjugate shown below in Equation 2.25

$$\begin{aligned} \text{Let } \mathbf{Q} &= q_0 + q_1\mathbf{i} + q_2 + \mathbf{j} + q_3\mathbf{k} \\ \text{Then } conj\,(Q) = \mathbf{Q}^* &= q_0 - q_1\mathbf{i} - q_2 + \mathbf{j} - q_3\mathbf{k} \end{aligned} \tag{2.25}$$

The norm of a quaternion is the quaternion product of the quaternion and it's conjugate, shown in Equation 2.26. The quaternion product of two unit magnitude quaternions is shown in Equation 2.27. If the quaternion is not a unit quaternion, normalization of the quaternion requires dividing the present quaternion by its norm.

$$\text{Norm of } \mathbf{Q} \;\equiv\; N\,(\mathbf{Q}) = \frac{\mathbf{Q}}{\sqrt{\mathbf{Q}^*\mathbf{Q}}} \tag{2.26}$$

$$\mathbf{PQ} = p_0q_0 - \mathbf{p}\cdot\,\mathbf{q} + p_0\mathbf{q} + q_0\mathbf{p} + \mathbf{p}\times\mathbf{q} \tag{2.27}$$

The quaternion product shown in Equation 2.27 represents a combined rotation of separate quaternion rotations, thus the order of the sequence is important with $\mathbf{Q}$ being the first rotation and $\mathbf{P}$ being the second rotation. Since the quaternion represents a transformation from one coordinate system to another, the quaternion product of a quaternion and its inverse must have unitary value just like the Euler transformation matrices. This property is shown in Appendix B.

Quaternion rotation of an attitude vector is known as quaternion operation, a reference coordinate system input attitude vector $\mathbf{G}_{ref}$ is rotated from the reference frame to vehicle frame via $\mathbf{Q}$, producing a vehicle coordinate system output vector $\mathbf{G}_{veh}$ shown in Equation 2.28.

$$\mathbf{G}_{veh} = \mathbf{Q}^*\,(\mathbf{G}_{ref})\,\mathbf{Q} = \left(q_0^2 - |\mathbf{q}|^2\right)\mathbf{G}_{ref} + 2\left(\mathbf{q}\mathbf{q}^T\right)\mathbf{G}_{ref} - 2q_0\,(\mathbf{q}\times\mathbf{G}_{ref}) \tag{2.28}$$

Note: $\mathbf{G}_{ref}$ *= 3 by 1 Vector of Reference Axes displacements or rates*
$\mathbf{Q}$ *= 4 by 1 Quaternion Vector*
$\mathbf{G}_{veh}$ *= 3 by 1 Vector of Vehicle Axes displacements or rates*

Equation 2.28 can be carried about mathematically to produce the transformation matrix shown in Equation 2.29

$$\mathbf{G}_{vehicle} = \begin{bmatrix} 2q_0^2 - 1 + 2q_1^2 & 2q_1q_2 + 2q_0q_3 & 2q_1q_3 - 2q_0q_2 \\ 2q_1q_2 - 2q_0q_3 & 2q_0^2 - 1 + 2q_2^2 & 2q_2q_3 + 2q_0q_1 \\ 2q_1q_3 + 2q_0q_2 & 2q_2q_3 - 2q_0q_1 & 2q_0^2 - 1 + 2q_3^2 \end{bmatrix} \mathbf{G}_{ref} \tag{2.29}$$

Likewise, a transfer from vehicle to reference frame can be performed as shown in Equation 2.30

$$\mathbf{G}_{ref} = \mathbf{Q}\left(\mathbf{G}_{vehicle}\right)\mathbf{Q}^* = \left(2q_0^2 - 1\right)\mathbf{G}_{veh} + 2\left(\mathbf{q}\cdot\mathbf{G}_{veh}\right)\mathbf{q} + 2q_0\left(\mathbf{q}\times\mathbf{G}_{vehicle}\right) \tag{2.30}$$

Rotation quaternions about each individual inertial coordinate system axis are calculated by applying Equation 2.23 to each axis and its respective Euler angle displacement, producing Equations 2.31, 2.32, 2.33, and the Aerospace Quaternion Rotation for a reference frame to vehicle frame rotation is given in Equation 2.34 according to the order of rotation rule for the quaternion product.

$$\textit{Rotation about Reference } Z : \mathbf{Q}_Z = \cos\frac{\psi}{2} + 0\ \hat{\mathbf{i}} + 0\ \hat{\mathbf{j}} + \sin\frac{\psi}{2}\hat{\mathbf{k}} \tag{2.31}$$

$$\textit{Rotation about Reference } Y : \mathbf{Q}_Y = \cos\frac{\theta}{2} + 0\ \hat{\mathbf{i}} + \sin\frac{\theta}{2}\ \hat{\mathbf{j}} + 0\ \hat{\mathbf{k}} \tag{2.32}$$

$$\textit{Rotation about Reference } X : \mathbf{Q}_X = \cos\frac{\phi}{2} + \sin\frac{\phi}{2}\ \hat{\mathbf{i}} + 0\ \hat{\mathbf{j}} + 0\ \hat{\mathbf{k}} \tag{2.33}$$

$$\mathbf{Q}_{R2V} = \mathbf{Q}_X\mathbf{Q}_Y\mathbf{Q}_Z \tag{2.34}$$

Thus,

$$\mathbf{G}_{veh} = \mathbf{Q}^*_{R2V}\mathbf{G}_{Ref}\mathbf{Q}_{R2V} \tag{2.35}$$

Attitude Quaternion [17, 22, 28]

Calculation of the attitude quaternion for a given set of Euler rotation angles in the Aerospace sequence requires equating the transfer matrix of Equation 2.29 and the transfer matrix of Equation 2.15. The quaternion parameters for the attitude quaternion are shown in the Equation Set 2.36. These equations are derived in Appendix B.

$$\begin{Bmatrix} q_0 \\ q_1 \\ q_2 \\ q_3 \end{Bmatrix} = \pm \begin{Bmatrix} \cos\frac{\phi}{2}\cos\frac{\theta}{2}\cos\frac{\psi}{2} + \sin\frac{\phi}{2}\sin\frac{\phi}{2}\sin\frac{\phi}{2} \\ \sin\frac{\phi}{2}\cos\frac{\theta}{2}\cos\frac{\psi}{2} - \cos\frac{\phi}{2}\sin\frac{\phi}{2}\sin\frac{\phi}{2} \\ \cos\frac{\phi}{2}\sin\frac{\theta}{2}\cos\frac{\psi}{2} + \sin\frac{\phi}{2}\cos\frac{\phi}{2}\sin\frac{\phi}{2} \\ \cos\frac{\phi}{2}\cos\frac{\theta}{2}\sin\frac{\psi}{2} - \sin\frac{\phi}{2}\sin\frac{\phi}{2}\cos\frac{\phi}{2} \end{Bmatrix} \tag{2.36}$$

Both solutions given in Equation 2.36 are correct for equating the transform matrices given in Equations 2.29 and 2.15. Two solutions are possible because the orientation of one coordinate system relative to another can be described by the terms of two right-handed rotations, thus the two solutions represent the two equivalent rotations with the

positive solution normally selected [22]. Equation 2.36 is useful if the Direction Cosine Matrix, T_{R2V} is not already known, if T_{R2V} is known then Equations 2.37 and 2.38 can be applied.

$$q_0 = \frac{1}{2}\sqrt{1 + DCM_{11} + DCM_{22} + DCM_{33}} \tag{2.37}$$

$$\left\{ \begin{array}{c} q_1 \\ q_2 \\ q_3 \end{array} \right\} = \left\{ \begin{array}{c} \frac{1}{4q_0}\left(DCM_{23} - DCM_{32}\right) \\ \frac{1}{4q_0}\left(DCM_{31} - DCM_{13}\right) \\ \frac{1}{4q_0}\left(DCM_{12} - DCM_{21}\right) \end{array} \right\} \tag{2.38}$$

Note: $DCM_{ij} = i^{th}$ row and j^{th} column of the Direction Cosine Matrix, T_{R2V}

Computation of the Euler Angles from a given attitude quaternion using the Aerospace sequence is shown as an algorithm in Equation 2.39 for attitude estimation even at Gimbal Lock.

$$\begin{aligned}
&\textbf{IF } q_1q_3 - q_2q_0 = -\frac{1}{2} \\
&\qquad \left\{ \begin{array}{c} \phi \\ \theta \\ \psi \end{array} \right\} = \left\{ \begin{array}{c} 2\text{asin}\left[q_1/\cos\left(\pi/4\right)\right] - \psi \\ \pi/2 \\ \text{Arbitrary} \end{array} \right\} \\
&\textbf{IF } q_1q_3 - q_2q_0 = \frac{1}{2} \\
&\qquad \left\{ \begin{array}{c} \phi \\ \theta \\ \psi \end{array} \right\} = \left\{ \begin{array}{c} 2\text{asin}\left[q_1/\cos\left(\pi/4\right)\right] + \psi \\ -\pi/2 \\ \text{Arbitrary} \end{array} \right\} \\
&\textbf{ELSE } \theta \neq \pm\pi/2 \\
&\qquad \left\{ \begin{array}{c} \phi \\ \theta \\ \psi \end{array} \right\} = \left\{ \begin{array}{c} \text{atan2}\left[2\left(q_0q_1 + q_2q_3\right), \left(2q_0^2 - 1 + 2q_3^2\right)\right] \\ \text{asin}\left[2\left(q_0q_2 - q_1q_3\right)\right] \\ \text{atan2}\left[2\left(q_0q_3 + q_1q_2\right), \left(2q_0^2 - 1 + 2q_1^2\right)\right] \end{array} \right\}
\end{aligned} \tag{2.39}$$

Equation 2.39's algorithm possesses two "IF "statements for dealing with Gimbal Lock occurrences at $\pm\pi/2$ deg where the Heading angle, ψ, becomes arbitrary. The criteria for the "IF" statements is based upon equating the third element in the first row of the Euler and Quaternion form of the Direction Cosine Matrix, i.e. $-\sin\theta = 2\left(q_1q_3 - q_2q_0\right)$, and substituting in the appropriate θ resulting in Gimbal Lock.

If the vehicle experiences no rotational movement about its axes, the attitude quaternion relating vehicle movement to reference frame movement remains constant. When the vehicle experiences rotation about any of the axes, the attitude quaternion must be modified to compensate for the rotational displacement. Translation does not affect the attitude quaternion because it is a rotation representation. For a rigid body rotating

at a constant rate, the system of governing differential equations written in Quaternion form is given by Equations 2.40 and 2.41.

$$\dot{\mathbf{Q}} - \Omega\mathbf{Q} = 0 \tag{2.40}$$

$$\Omega = \frac{1}{2}\begin{Bmatrix} 0 & -\vec{\omega}^T \\ \vec{\omega} & -[\vec{\omega}\times] \end{Bmatrix} = \frac{1}{2}\begin{bmatrix} 0 & -p & -q & -r \\ p & 0 & r & -q \\ q & -r & 0 & p \\ r & q & -p & 0 \end{bmatrix} \tag{2.41}$$

The solution to the first-order linear differential vector equation given in Equation 2.40, assuming constant rotation, is given by Equation 2.42. The derivation of this solution is given in Appendix B.

$$\mathbf{Q} = \left[\mathbf{I}_{4\times4}\cos\left(\frac{|\vec{\omega}|t}{2}\right) + \frac{2\Omega}{|\vec{\omega}|}\sin\left(\frac{|\vec{\omega}|t}{2}\right)\right]\mathbf{Q}_{t=t_0} \tag{2.42}$$

Using Equations 2.40 and 2.30 and comparing the kinematic calculation to the sensed displacement, a bias error for the rate sensors can be estimated when the vehicle experiences rotational motion.

2.2 Signal Filtering

2.2.1 Noise Contaminated Signal Model

Due to noise presence in sensor signals, the signal must be filtered before implementation in the attitude estimation algorithm without major deviation from the signal's truth. The adopted sensor model accounting for noise, is the sum of the true signal and generated noise due to the sensor or another source. Equation 2.43 relates the measured output of a sensor given noise contamination which may or may not vary with time.

$$\begin{array}{ccccc} \textit{measured value} & = & \textit{true value} & + & \textit{measurement noise} \\ \tilde{\mathbf{x}} & = & \mathbf{x} & + & \nu(t) \end{array} \tag{2.43}$$

Signal contamination arises from any number of sources, including or in addition to any of the following:

1. **Mission Operation Environment** - extreme/harsh weather effects on electronics or unpredicted fluctuations in Earth's magnetic field
2. **Vehicle Hardware Environment** - signal interference from other powered electronics from within the vehicle or degradation quality of electronics
3. **External Signal Interference** - signal interference from other electronic sources outside of the vehicle

2.2.2 Signal Noise Types

The measurement noise, $\nu(t)$, can take many a form depending on the classification of the noise - Gaussian or NonGaussian noise and further divided into white or colored. For this research, White Gaussian noise was simulated for sensor signal contamination across all frequencies at equal power since this distribution is the most common for modeling sensor error due to noise corruption [8].

Gaussian Noise is distributed according to the probability density function $p(x)$, of the Normal Distribution defined by a mean, μ, and a standard deviation, σ, yielding the traditional bell-shaped distribution. Equation 2.44 gives the probability density function defining the distribution. This distribution is common used for noise effects because of the *Central Limit Theorem* stating that any random sample of data generated from any distribution with a given μ and σ^2 will approach a Gaussian Distribution of μ and σ^2/N as the sample size, N, increases.

$$p(x) = \frac{1}{\sqrt{2\pi\sigma^2}}\exp\left(-\frac{1}{2\sigma^2}(x-\mu)^2\right) \tag{2.44}$$

NonGaussian Noise is distributed in a similar fashion to Gaussian but allows for extreme outlier data to effect the shape of the probability density function. Equation 2.45 gives the probability density function defining such a distribution. [24]

$$p(x) = \frac{1}{\sqrt{2\sigma^2}}\exp\left(-\sqrt{\frac{2}{\sigma^2}}|x|\right) \tag{2.45}$$

White Noise contains all noise frequencies with the mean of the noise signal being zero since all frequencies are represented equally. White noise is most commonly used to model sensor noise in parameter estimation since White noise is uncorrelated from one instant to the next. Colored Noise contains all frequencies of noise at equal power except certain frequencies, typically high and low, are attenuated due to the low power associated with the signal at those fringe frequencies. An example of colored noise is the Markov Sequence where the power decreases at increasing frequencies and the noise is correlated from one instant to the next. [30]

2.2.3 Signal Filters [4, 11, 24, 32]

Signal filters are designed to allow certain frequencies to pass through unchanged, bandwidth, while attenuating other frequencies. Linear filters are designed for use with linear functions, possessing no nonlinearities resulting from saturation or dead-bands, while nonlinear filters are used for signals where saturation or dead-banding is an issue. Digital filters are applied to discrete time signals whereas analog filters are applied to continuous

time signals, a conversion between the two filters exists as long as the sampling frequency of the signal is known. The types of analog filters used in this work are low-pass, LPF, and high-pass, HPF, due to either the slow dynamics of sensor, accelerometer, or the fast dynamics of a sensor's signal derivative, rate of change of the rate gyro signal. All the filters used in this work derived in Appendix C.

First-Order Filters

The corresponding electrical representation of the transfer functions of a First-Order LPF and HPF are derived from a resistor and capacitor in series, Appendix C.1, where the input is voltage $\mathbf{V}_{IN}$ corresponds with output voltages, $\mathbf{V}_C$ for a LPF in Equation 2.46 and $\mathbf{V}_R$ for a HPF in Equation 2.47. Figure 2.3 displays the magnitude and phase responses of the first-order filters with a natural frequency, ω_n of 1 rad/sec and damping ratio, ζ, of $1/\sqrt{2}$.

$$\mathbf{LPF} = \frac{\mathbf{V_C}}{\mathbf{V_{in}}} = \frac{\zeta\omega_n}{s + \zeta\omega_n} \tag{2.46}$$

$$\mathbf{HPF} = \frac{\mathbf{V_R}}{\mathbf{V_C}} = \frac{s}{s + \zeta\omega_n} \tag{2.47}$$

$$Note: \ \zeta\omega_n = \frac{1}{RC}$$

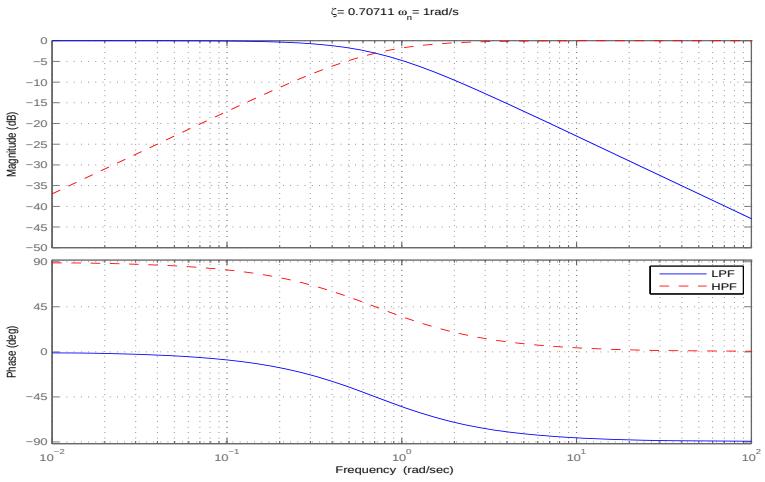

Figure 2.3: Bode Diagrams of First-Order Analog Filters

Examining the LPF character in Figure 2.3, around 0.2 rad/sec, the magnitude starts to decrease with a slight parabolic trajectory known as "roll off". The roll off until achieving a -20dB/decade slope spans a frequency band from 0.2 rad/sec to 2 rad/sec. The "roll on" frequency band for the HPF is approximately the same as the roll off and the slope is +20dB/decade.

Second-Order Filters

If either of the first-order filters have a roll taking up a considerable part of the bandwidth, a second-order filter analog filter should be used so the targeted low frequency band or high frequency band passes through unattenuated. The transfer functions for second-order analog filters are derived from a resistor, inductor, and capacitor in series, known as a RLC circuit, displayed n Figure 2.4.

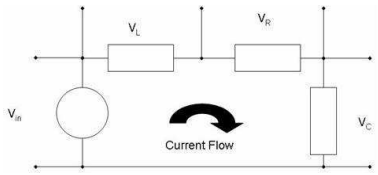

Figure 2.4: Series RLC Circuit Diagram

The transfer functions for the second-order LPF is given in Equation 2.48 and the transfer function for the second-order HPF is given in Equation 2.49, with their derivations given in Appendix C.2.

$$\mathbf{LPF} = \frac{\mathbf{V_C}}{\mathbf{V_{in}}} = \frac{\omega_n^2}{s^2 + 2\zeta\omega_n s + \omega_n^2} \tag{2.48}$$

$$\mathbf{HPF} = \frac{\mathbf{V_L}}{\mathbf{V_C}} = \frac{s^2}{s^2 + 2\zeta\omega_n s + \omega_n^2} \tag{2.49}$$

$$Note: \ \omega_n^2 = \frac{1}{LC} \text{ and } 2\zeta\omega_n = \frac{R}{L}$$

The Bode diagram in Figure 2.5 of Equations 2.48 and 2.49 with the same ω_n and ζ displays how the roll frequency band was diminished to interval of 0.8 rad/sec to 1.25 rad/sec with a slope of 40dB/decade, positive for HPF and negative for LPF as compared to the 0.2 to 2 rad/sec interval and 20dB/decade for the first-order filters.

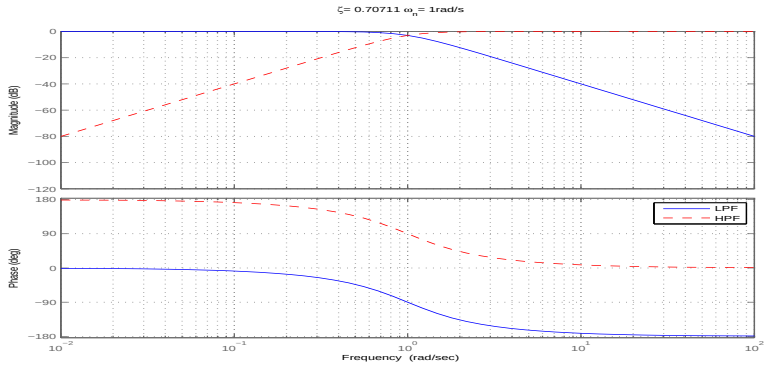

Figure 2.5: Bode Diagrams of Second-Order Analog Filters

Figures 2.3 and 2.5 illustrate minimizing the roll off band for a LPF offers greater control over dictating the frequencies passed through unaltered and those which are attenuated. Increasing the order of the filter increases the magnitude of the roll slope while diminishing the length of the roll band. Practical implementation of analog signal filtering is shown in Figure 2.6, where a LPF performs better than a HPF when filtering a white Gaussian noise contaminated gyro signal. This is demonstrated by the smooth line tracking the gyro signal for the LPF while the HPF possesses a large amount of noise and does not correctly track the gyro signal, yielding the conclusion of signal contamination stemming from high frequency noise. Considering the phase responses from the Bode Diagrams, care must be taken with filter implementation because the phase response can be as much as 180 degrees out of phase with the original signal leading to induced errors depending on how the filtered signal is to be used within the system's control law or system observer. As shown by Figure Even though the LPF possesses better tracking, the filtered signal lags significantly behind the gyro signal during large pitch rate phases.

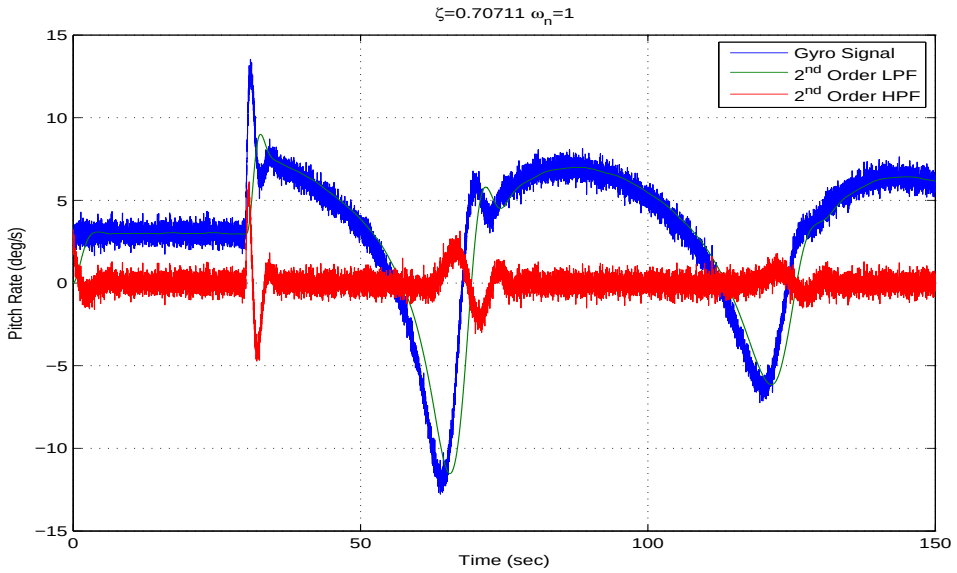

Figure 2.6: Time History of LPF and HPF Filtered Data

Butterworth Filter

Another filter used in this work is a form of a low-pass filter called a Butterworth Filter. This filter has relatively the same shape as the previously derived LPF and is used to keep frequency passband shape as flat as possible with no oscillation while having a short band of frequency roll off. The Butterworth filter is the only filter that maintains its shape as its order is increased except that its declining slope increases linearly with its order. A Fourth-Order Butterworth filter transfer function with a cutoff frequency of 15

rad/sec is given in Equation 2.50, with calculation of the coefficients from Appendix C.3. The cutoff frequency, ω_C, is defined as the frequency at which the filtered magnitude decays to -3db of its original magnitude. The appropriate cutoff frequency is arrived at experimentally through frequency analysis of the parameter to be measured by the sensor and knowing the hardware limits of the sensor. The Bode Diagram of Equation 2.50 is shown in Figure 2.7. The Butterworth filter effectiveness is illustrated by comparing the filtered output accelerometer data to the white Gaussian noise contaminated signal taken from a linear plant model simulation as shown in Figure 2.8.

$$Butterworth\ TF = \frac{50625}{1s^4 + 39.1969s^3 + 768.1981s^2 + 8819.3s + 50625} \tag{2.50}$$

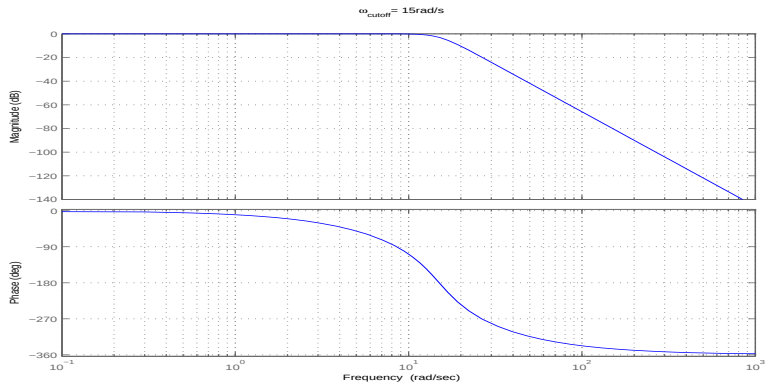

Figure 2.7: Fourth-Order Butterworth Filter with Cutoff Frequency = 15 rad/s

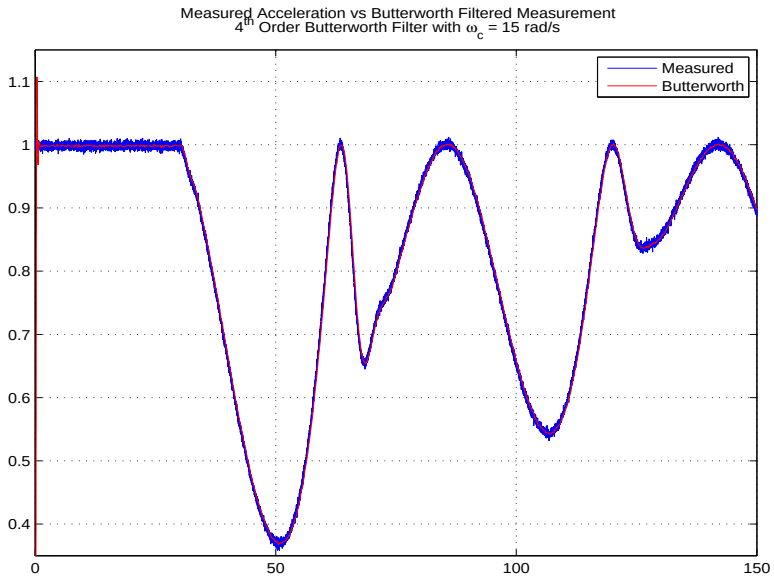

Figure 2.8: Fourth-Order Butterworth and Original Accelerometer Data Comparison

Figure 2.7 shows a phase lag of more than 90 degrees between the near zero frequencies and the frequencies around 10 radians per second. The filter's phase lag effect is considerable when the vehicle is experiencing significant changes in rotational. The phase lag of the filter across the passband increases as the filter's order is increased. This lag can be lessened by increasing the passband with the tradeoff of passing higher frequency content through the filter unattenuated resulting the possibility of signal corruption. An alternative action to reduce the phase lag while keeping the passband unaltered is by reducing the order of the butterworth filter, with the consequence of a more noisy output compared to a higher order filter. Figure 2.9 displays the Bode diagram comparison of a second and fourth order butterworth filters.

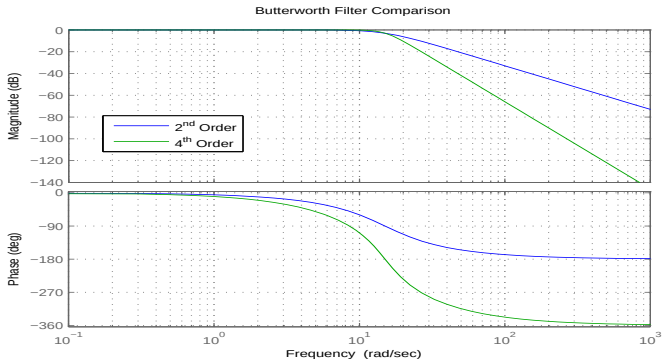

Figure 2.9: Bode Diagram for Second and Fourth Order Butterworth Filters

By reducing the order of the Butterworth Filter, the phase lag between the filtered accelerometer estimate from a noise contaminated signal and the true accelerometer measurement is reduced resulting in a reduced attitude error when using accelerometer data. Figure 2.10 displays the decrease in accelerometer measurement error by filter order reduction is approximately 0.02 gees during vehicle maneuvers. Figure 2.11 shows this error decrease results in an attitude accuracy of the resolved measurements to be ± 3 degrees for the second-order filter where the fourth-order filter had an accuracy of ± 6 degrees.

2.3 Bias Estimation

2.3.1 Biased Noise Contaminated Signal Model

A Sensor bias can arise due to hardware shortcomings in manufacturing or calibration errors in hardware installation. Equation 2.51 expands upon Equation 2.43 to account for a signal bias term with the ability to change over time to produce the generally accepted

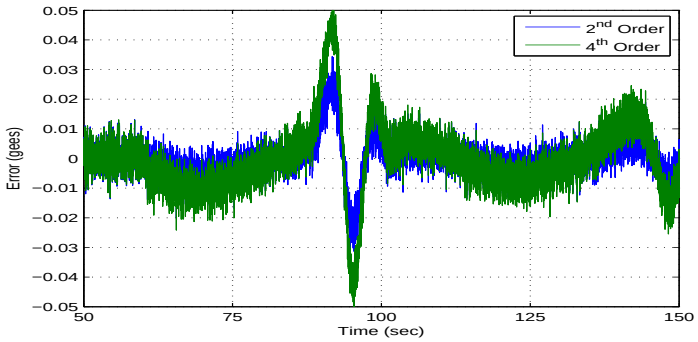

Figure 2.10: Accelerometer Error of different order Butterworth Filters

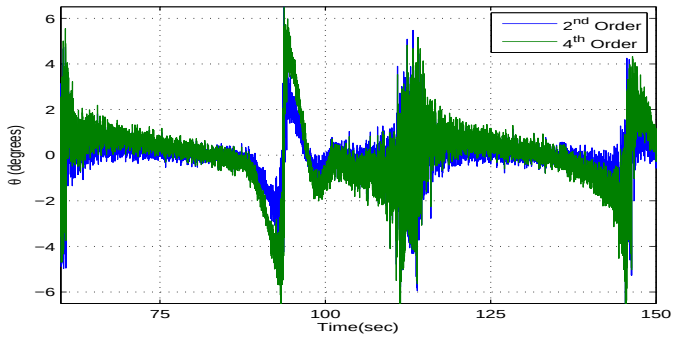

Figure 2.11: Theta Error of different order Butterworth Filters

noise contaminated sensor model developed by Farrenkopf in [9].

$$\begin{array}{ccccccc} \textit{measured value} & = & \textit{true value} & + & \textit{measurement noise} & + & \textit{bias} \\ \tilde{\mathbf{x}} & = & \mathbf{x} & + & \nu(t) & + & b(t) \end{array} \tag{2.51}$$

A sensor measuring vehicle rates is producing a relative measurement because the measurement is not with respect to the inertial coordinate frame but instead a relative frame. While sensor measurements of vehicle motion in inertial frame are producing an absolute measurement. The bias associated with an absolute sensor, accelerometer, can be calculated by comparing what the expected value should be at a given orientation to the output of the sensor. Ease of estimation of a bias associated with a relative sensor can range from simple to complex depending on the information known about the sensor and the dynamics of the vehicle. Estimation algorithms vary widely depending on vehicle operation conditions and available sensor information. Trigger back-differencing and Kalman Filter estimation algorithms are presented based upon the proposed device utilizing a rate gyro and accelerometer measurements operating in a wide array of conditions.

2.3.2 Trigger Back-differencing [7]

As priorly mentioned, [7] presents a device consisting of a rate gyro paired mounted perpendicular to an accelerometer array to estimate the rate gyro bias during vehicle maneuvers based upon the difference of two consecutive accelerometers falling below a preset threshold. The rate gyro bias is calculated at the discrete trigger points using Equation 2.52.

$$\hat{\mathbf{b}}_{Dynamic} = \frac{[\hat{\varphi}_{\mathrm{i}} - \hat{\varphi}_{\mathrm{i}-1}] - [\tilde{\varphi}_{\mathrm{i}} - \tilde{\varphi}_{\mathrm{i}-1}]}{\mathrm{t_i} - \mathrm{t_{i\text{-}1}}} \tag{2.52}$$

$Where:$	$\hat{\varphi}$	=	Angle estimate from integration of Rate Gyro Signal
	$\tilde{\varphi}$	=	Angle estimate from Accelerometers
	t	=	Time of Angle estimate
	i,i-1	=	Present Dynamic Trigger Point, Previous Dynamic Trigger Point

A dynamic trigger point is defined as a point where the vehicle experiences rotational acceleration and the difference of two consecutive accelerometers measure the gravity vector within a specified tolerance. Since the positions of the accelerometers with respect to the vehicle's axes are known, the absolute orientation of the vehicle can be calculated and the rate gyro integration initial conditions can be reset using measurements from the accelerometers and the trigonometric relationship given in Equations 2.53 and 2.54. These equations assume the device is undergoing pure rotation motion, is only subjected to gravitational acceleration, and the device is set-up according to [7] shown in Figure 2.12 with the horizontal vector pointing in the direction of the vehicle's primary axis and the middle accelerometer collinear with the vehicle's tertiary axis.

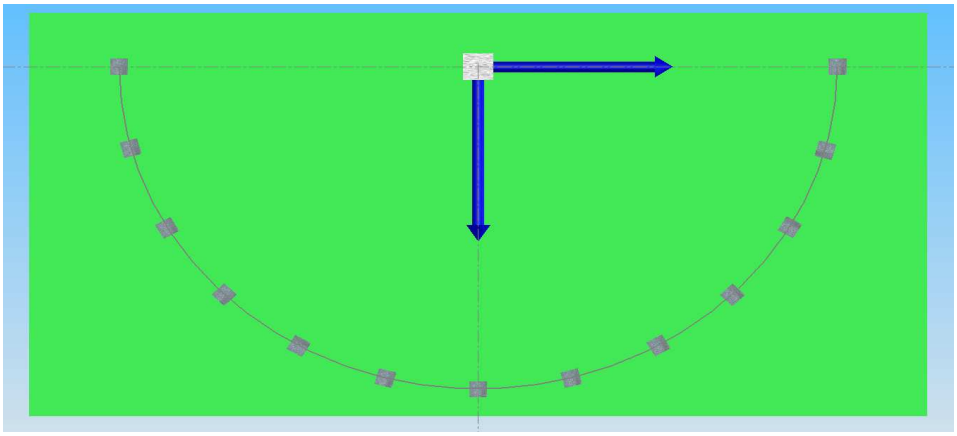

Figure 2.12: Device Set-Up

$$|\theta_{Maneuver}| = \arccos\left(gA_{z,i}\right) - |\theta_{i,static}| \tag{2.53}$$

$$\theta_{Maneuver} = |\theta_{Maneuver}| * -sign\left(gA_{z,1}\right) \tag{2.54}$$

Where $gA_{z,i}$ is the measurement of the i^{th} accelerometer in gees and $gA_{z,1}$ is the measurement of the accelerometer mounted 90 degrees clockwise from the accelerometer parallel with the vehicle's tertiary axis. By continuously subtracting the bias term the rate gyro signal, "dynamic compensation"for drift is performed. However, the device must register rotational motion to obtain a rate gyro bias estimate via dynamic compensation.

A static trigger occurs when no significant rotational acceleration, measured by the filtered derivative of the rate gyro signal compared with a threshold value, about the measurement axis has been sensed for a given time interval. Static compensation is performed using a single accelerometer to calculate the attitude angle using the tertiary axes element from Equation 2.17. This yields Equation 2.55, relating the acceleration of gravity in the fixed coordinate system, $\ddot{S}_Z$, to the accelerations registered along the roll, pitch, and yaw axes due to a roll and/or pitch maneuver, $\ddot{s}_x,\ \ddot{s}_y,\ \ddot{s}_z, \phi$ and θ respectively. The calculated angle is then used to reset the rate gyro integration initial conditions and calculate the gyro bias using Equation 2.52.

$$\ddot{S}_Z = -\ddot{s}_x \sin\theta + \ddot{s}_y \cos\theta \sin\phi + \ddot{s}_z \cos\theta \cos\phi \tag{2.55}$$

For accurate bias estimation, the static estimator and dynamic estimator must be fused using a boolean switch which corresponds to the presence of significant rotational acceleration of the measurement axis. Equation 2.56 uses an angular acceleration threshold, $\ddot{\varphi}_{thres}$, defined depending on the application to trigger bias estimation.

$$\hat{\mathbf{b}} = \xi\left(\hat{\mathbf{b}}_{Dynamic}\right) + (1-\xi)\left(\hat{\mathbf{b}}_{Static}\right) \tag{2.56}$$
$$Where:\ \xi = \begin{cases} 1 & \ddot{\varphi} > \ddot{\varphi}_{thres} \\ 0 & \ddot{\varphi} \leq \ddot{\varphi}_{thres} \end{cases}$$

2.3.3 The Kalman Filter [8, 13, 30, 34]

The Linear Kalman Filter

A Kalman filter is a linear sequential recursive observer updating the observed state estimates based on actual system measurements and the predicted state values from a predefined system model. For implementation, a state-space system model must be provided correctly modeling the system dynamics, process noise, and measurement noise as shown in Equation 2.57 for the continuous linear case and Equation 2.58 for the linear discrete case. Table 2.2 summarizes the variable definitions, the conversion from linear to discrete matrices is given in the Appendix in Section D.2.

$$\begin{aligned} \dot{\mathbf{x}} &= \mathbf{A}(\mathrm{t})\,\mathbf{x} + \mathbf{B}(\mathrm{t})\,\mathbf{u}(\mathrm{t}) + \mathbf{G}(t)\,\mathbf{w}(\mathrm{t}) \\ \mathbf{y} &= \mathbf{C}(t)\,\mathbf{x} + \mathbf{v}(\mathrm{t}) \end{aligned} \tag{2.57}$$

$$\begin{aligned} \mathbf{x}_{k+1} &= \Phi_k \mathbf{x}_k + \Gamma_k \mathbf{u}_k + \Upsilon_k \mathbf{w}_k \\ \mathbf{y}_k &= \Lambda_k \mathbf{x}_k + \mathbf{v}_k \end{aligned} \tag{2.58}$$

The Kalman Filter uses prior states and state covariances along with present measure-

Domain Variable		Vector or Matrix	Description
Continuous	Discrete		
$\dot{\mathbf{x}}$	$\mathbf{x}_{k+1}$	N by 1 Vector	Equations for Model State Update
$\mathbf{A}(t)$	Φ_k	N by N Matrix	State Transition Matrix
$\mathbf{x}$	$\mathbf{x}_k$	N by 1 Vector	"N"State Variables
$\mathbf{B}(t)$	Γ_k	N by M Matrix	Input Distribution Matrix
$\mathbf{u}$	$\mathbf{u}_k$	M by 1 Vector	System Input Vector
$\mathbf{G}(t)$	Υ_k	N by N Matrix	Process Noise Distribution Matrix
$\mathbf{w}(t)$	$\mathbf{w}_k$	N by 1 Vector	Process Noise in State Equations
$\mathbf{y}$	$\mathbf{y}_k$	L by 1 Vector	System Output Vector
$\mathbf{C}(t)$	Λ_k	L by L Matrix	Measurement Output Matrix
$\mathbf{v}(t)$	$\mathbf{v}_k$	L by 1 Vector	Measurement Noise in Output

Table 2.2: State Space Equation Definitions

ments to continually predict and correct state estimates based upon the system model output and available measurements. The filter seeks to minimize the residual state error between the measured states, $\mathbf{x}^*$, and system model states, $\hat{\mathbf{x}}$, by continually adjusting the Kalman Gain vector "K". The gain is a function of the accumulating error in the error covariance matrix "P", a square matrix summarizing the estimation error variance associated with the state variables, and the noise variances modeled in the system. The Kalman Gain vector is determined by minimizing the trace of the state error covariance matrix which is equivalent to minimizing the length of the estimation error vector [8]. Table 2.3 gives the algorithm for the linear discrete for discrete Kalman filter, LDKF. Appendix D.1 summarizes the calculation of the statistic variables used in the Kalman Filter, derivations of the linear discrete and continuous Kalman Filter can be found from numerous sources, [8], [13], [17], [30], with [34] completely devoted the Kalman Filter and its applications.

For initialization of the LDFK when measurements are available at the initial time, step D2 occurs followed subsequently by steps D3 through D5 to propagate the new states, the filter then cycles through steps D3 through D5 after initialization for continued operation. If no measurements are available step D5 is executed first to initialize the states and their covariances so the continual operation steps of D3 through D5 can be performed until the final measurement is given. Equations D3 and D5 are known as the *Matrix Riccati Equations*. The LDKF is usually implemented for real-world applications but the continuous linear Kalman filter, Table 2.4, is useful in understanding steady state operation of the discrete Kalman filter as a low-pass filter with the bandwidth as a function

Assumptions	$\mathbf{w}_k \sim N(0, \mathrm{Q}_k)$, $\mathbf{v}_k \sim N(0, \mathrm{R}_k)$ $\mathrm{E}\{\mathbf{w}_k \mathbf{v}_k^{\mathrm{T}}\}$=0 for all k and $\mathrm{R}_k = E\{\mathbf{v}_k \mathbf{v}_k^T\}$	$(D1)$
Initialize States and Covariance	$\hat{\mathbf{x}}(\mathrm{t}_0) = \hat{\mathbf{x}}_0$ $\mathbf{P}_0 = \mathrm{E}\left\{\tilde{\mathbf{x}}(\mathrm{t}_0)\,\tilde{\mathbf{x}}(\mathrm{t}_0)^T\right\}$	$(D2)$
Kalman Gain "Input Stage"	$\mathrm{K}_k = \mathbf{P}_k^- \Lambda_k^T \left[\Lambda_k \mathbf{P}_k^- \Lambda_k^T + R_k\right]^{-1}$	$(D3)$
Updates	$\hat{\mathbf{x}}_k^+ = \hat{\mathbf{x}}_k^- + K_k\left[\tilde{\mathbf{y}}_k - \Lambda_k \hat{\mathbf{x}}_k^-\right]$ $\mathbf{P}_k^+ = [I - K_k\Lambda_k]\,\mathbf{P}_k^-$ I = Identity Matrix	$(D4)$
Propagation "Output Stage"	$\hat{\mathbf{x}}_{k+1}^- = \Phi_k \hat{\mathbf{x}}_k^+ + \Gamma_k \mathbf{u}_k$ $\mathbf{P}_{k+1}^- = \Phi_k P_k^+ \Phi_k^T + \Upsilon_k Q_k \Upsilon_k^T$	$(D5)$

Table 2.3: Linear Discrete Time Kalman Filter (LDKF) Algorithm

Assumptions	$\mathbf{w}(\mathrm{t}) \sim N(0, \mathrm{Q}(t))$, $\mathbf{v}(\mathrm{t}) \sim N(0, \mathrm{R}(t))$, R^{-1} exists $\mathrm{E}\left\{\mathbf{w}(t)\,\mathbf{v}(t)^{\mathrm{T}}\right\}$=0 for all time and R=$E\{\mathbf{v}\mathbf{v}^T\}$	$(C1)$
Initialize States and Covariance	$\hat{\mathbf{x}}(\mathrm{t}_0) = \hat{\mathbf{x}}_0$ $P_0 = \mathrm{E}\left\{\tilde{\mathbf{x}}(\mathrm{t}_0)\,\tilde{\mathbf{x}}(\mathrm{t}_0)^T\right\}$	$(C2)$
Kalman Gain "Input Stage"	$K(t)$=$P(t)\boldsymbol{C}^T(t)\,R^{-1}$	$(C3)$
Update Covariance	$\dot{P} = \mathbf{A}(t)\,P(t) + P(t)\,\mathbf{A}^T(t)$ $-P(t)\,\mathbf{C}^T(t)\,R^{-1}(t)\,\mathbf{C}(t)\,P(t) + \mathbf{G}(t)\,Q(t)\,\mathbf{G}^T(t)$	$(C4)$
Update States	$\dot{\hat{\mathbf{x}}}(t) = \mathbf{A}(t)\,\hat{\mathbf{x}}(t) + \mathbf{B}(t)\,\mathbf{u}$ $+K(t)\,[\tilde{\mathbf{y}} - \mathbf{C}(t)\,\hat{\mathbf{x}}(t)]$	$(C5)$

Table 2.4: Linear Continuous Time Kalman Filter (LCKF) Algorithm

of the process and measurement noise [34]. If the sampling interval is small enough the LDKF becomes a LCKF. Initialization of the LCKF requires initial measurements to be present in order for the filter to operate else the states and state covariances cannot be updated.

At steady state the system operation, the linear system follows equation C5 except the impact of the input has long been dissipated:

$$\dot{\hat{\mathbf{x}}}(t) = \mathbf{A}(t)\,\hat{\mathbf{x}}(t) + K(t)\,[\tilde{\mathbf{y}} - \mathbf{C}(t)\,\hat{\mathbf{x}}(t)] \tag{2.59}$$

Equation 2.59 results in two first-order linear differential equations for a two state vector. These equations can be solved in the Laplace domain to yield the state estimate to

measurement transfer function as a function of the Kalman Gain vector elements shown in Equation 2.60.

$$\frac{\hat{\mathbf{x}}}{\tilde{\mathbf{y}}} = \frac{K_1 s + K_2}{s^2 + K_1 s + K_2} \tag{2.60}$$

From Equation 2.60, the steady state linear continuous two state Kalman filter is a second-order transfer function that behaves as a combined low-pass and bandpass filter with a natural frequency, ω_n, of $\sqrt{K_2}$ and a damping ratio, ζ, of $K_1/\left(2\sqrt{K_2}\right)$. Since the Kalman gain vector is a function of the state covariance, the measurement output matrix, and the measurement noise, the steady-state response characteristics of the filter are computed as a function of process noise from the state covariance matrix and the measurement noise. [34]

The Nonlinear Extended Kalman Filter

A large group of system models exist in the nonlinear form, i.e. aircraft models, where adaptations to linear filter and control techniques are needed because nonlinear systems yield more output solutions than linear systems. It can be advantageous to implement a Kalman filter in a nonlinear system because redundant sensors can be eliminated as long as the system's dynamics are modeled correctly and attitude data is available, in some form, from other sensors. For a continuous nonlinear system, the state-space model is given in Equation 2.61 where $\mathbf{a}\left(\mathbf{x}\left(t\right), \mathbf{u}\left(t\right), t\right)$ and $\mathbf{c}\left(\mathbf{x}\left(t\right), t\right)$ are assumed to be continuously differentiable with respect to the state vector, $\mathbf{x}\left(t\right)$.

$$\begin{aligned} \dot{\mathbf{x}}\left(t\right) &= \mathbf{a}\left(\mathbf{x}\left(t\right), \mathbf{u}\left(t\right), t\right) + \left[G\right]\mathbf{w}\left(t\right) \\ \tilde{\mathbf{y}} &= \mathbf{c}\left(\mathbf{x}\left(t\right), t\right) + \mathbf{v}\left(t\right) \end{aligned} \tag{2.61}$$

Examples of nonlinearities in systems are the result of centripetal forces in rotational motion, Coulomb friction inherent to the system, and saturation of a particular sensor or the dead-zone of a motor imposed on the system [29]. Consequently nonlinear systems do not possess the superposition characteristic beneficial to linear systems where two or more separate linear systems can be added together, creating a composite linear system. Nonlinear system models must be constructed at instance of system operation because addition of multiple nonlinear models mimicking parts of the overall system may not produce the output characteristic of overall system operation.

Implementation of the nonlinear model via a linearized form of the Kalman Filter can be done various ways. The Extended Kalman Filter, EKF, assumes the true state is sufficiently close to the estimated state and thus the error dynamics can be relatively accurately portrayed by a linearized first-order Taylor series expansion about a nominal state [8]. The linearization of $\mathbf{a}$ and $\mathbf{c}$ using a first-order Taylor Series expansion about

some desired state, $\bar{\mathbf{x}}(t)$, is shown in Equations 2.62 and 2.63.

$$\begin{aligned}\mathbf{a}(\mathbf{x}(t),\mathbf{u}(t),t) &\cong \mathbf{a}(\bar{\mathbf{x}}(t),\mathbf{u}(t),t) + \left.\frac{\partial \mathbf{a}}{\partial \mathbf{x}}\right|_{\bar{\mathbf{x}}(t)} [\mathbf{x}(t) - \bar{\mathbf{x}}(t)] \\ &\cong \mathbf{a}(\bar{\mathbf{x}}(t),\mathbf{u}(t),t) + \mathbf{A}(\bar{\mathbf{x}}(t),t)[\mathbf{x}(t) - \bar{\mathbf{x}}(t)] \qquad (2.62)\\ \mathbf{c}(\mathbf{x}(t),t) &\cong \mathbf{c}(\bar{\mathbf{x}}(t),t) + \left.\frac{\partial \mathbf{c}}{\partial \mathbf{x}}\right|_{\bar{\mathbf{x}}(t)} [\mathbf{x}(t) - \bar{\mathbf{x}}(t)] \\ &\cong \mathbf{c}(\bar{\mathbf{x}}(t),\mathbf{u}(t),t) + \mathbf{C}(\bar{\mathbf{x}}(t),t)[\mathbf{x}(t) - \bar{\mathbf{x}}(t)] \qquad (2.63)\end{aligned}$$

The nominal state is taken to be the current estimate, $\hat{\mathbf{x}}$, in the EKF. The approximations

Assumptions	$\mathbf{w}(t) \sim N(0, \mathrm{Q}(t))$, $\mathbf{v}(t) \sim N(0, \mathrm{R}(t))$, R^{-1} exists $\mathrm{E}\left\{\mathbf{w}(t)\,\mathbf{v}(t)^{\mathrm{T}}\right\}$=0 for all k
Initialize States and Covariance	$\hat{\mathbf{x}}(\mathrm{t}_0) = \hat{\mathbf{x}}_0$ $P_0 = \mathrm{E}\left\{\tilde{\mathbf{x}}(\mathrm{t}_0)\,\tilde{\mathbf{x}}(\mathrm{t}_0)^T\right\}$
Kalman Gain "Input Stage"	$K(t) = P(t)\,\mathbf{C}^T(\hat{\mathbf{x}}(t),t)\,R^{-1}$ Where: $\mathbf{C}(\hat{\mathbf{x}}(t),t) = \left.\frac{\partial \mathbf{c}}{\partial \hat{\mathbf{x}}}\right\|_{\hat{\mathbf{x}}(t)}$
Update Covariance	$\dot{P} = \mathbf{A}(\hat{\mathbf{x}}(t),t)\,P(t) + P(t)\,\mathbf{A}^T(\hat{\mathbf{x}}(t),t)$ $-P(t)\,\mathbf{C}^T(\hat{\mathbf{x}}(t),t)\,R^{-1}(t)\,\mathbf{C}(\hat{\mathbf{x}}(t),t)\,P(t) + \mathbf{G}(t)\,Q(t)\,\mathbf{G}^T(t)$ Where: $\mathbf{A}(\hat{\mathbf{x}}(t),t) = \left.\frac{\partial \mathbf{a}}{\partial \hat{\mathbf{x}}}\right\|_{\hat{\mathbf{x}}(t)}$
Update States	$\dot{\hat{\mathbf{x}}}(t) = \mathbf{a}(\hat{\mathbf{x}}(t),\mathbf{u}(t),t) + K(t)\,[\tilde{\mathbf{y}} - \mathbf{C}(\hat{\mathbf{x}}(t),t)\,\hat{\mathbf{x}}(t)]$

Table 2.5: Continuous Time Nonlinear Kalman Filter Algorithm

are then substituted for the nonlinear functions in the Continuous Linear Kalman Filter shown in Table 2.5. Since the $\mathbf{A}(\bar{\mathbf{x}}(t),t)$ and $\mathbf{C}(\bar{\mathbf{x}}(t),t)$ are not constant, a steady-state gain cannot be found resulting in increased computation burden since n(n+1)/2 nonlinear equations need to be integrated to determine P(t) [8].

The EKF estimate accuracy can be enhanced by continually relinearizing about the most recent estimate and recalculating the covariance matrix, P, and the Kalman Gain this method is known as the *Iterated Extended Kalman Filter*. The extended Kalman Filter can be shown to converge on a state estimate even with errors in the initial conditions through simulation. The EKF can also be linearized about a nominal state vector, $\bar{\mathbf{x}}$, that is known *a priori* instead of the current estimate, $\hat{\mathbf{x}}$. This is known as the "*Linearized Kalman Filter*"which has reduced accuracy compared to the EKF but the online computational burden is reduced significantly because the nominal state vector is already known. [8]

Kalman Filter Considerations [8, 13, 34]

Sufficient knowledge of the system's dynamics and measurement signal is required for construction and implementation of an effective Kalman Filter. The posed linear model must be extremely accurate due to the use of prior model estimates and system noise to calculate appropriate gains for update of the state variables. Any error in modeling dynamics or associated noise will have a propagated impact over the entire filter operation interval.

State-space model design must consider the polynomial order of the measurement signal so all necessary derivatives are accounted for without introducing unnecessary process noise. For example, if the measurement signal is a third-order polynomial but the filter was designed with only second-order dynamics, the third derivative will not be estimated and state estimate error results. Likewise, if the system was modeled as a third-order system with a second-order measurement signal, additional process noise is present resulting in estimation error. The measurement interval should be taken into account since a lower order filter is more accurate than a higher order filter when only a small amount of data is available.

The initialization of the state error covariance matrix, P, possesses tuning sensitivity when the standard deviation of the noise to the signal amplitude ratio is greater than unity or when the diagonal elements of the matrix are set very close to zero. When the diagonal elements are set very close to zero, the filter ceases to update the state estimates resulting in either filter divergence or a long convergence time. In the noise to signal ratio case, the measured signal is completely saturated by the sensor noise produced from failing or fail sensors. For proper filter operation, the sensor biases must be exactly known to produce a correct tracking estimate via a perfectly initialized state vector. With the bias and noise perfectly known results in a the state covariance matrix equal to all zeros rendering the filter virtually worthless.

Assuming the vehicle possesses relatively accurate sensors and the system model is relatively accurate even a badly initialized linear Kalman filter will usually recover to provide a good estimate given time to collect enough measurement data. As long as the diagonal terms of the matrix are not set to zero, the filter will converge to the correct estimate with the difference being the time to converge. The convergence transient can be reduced by a process called *warm starting* where good initial state estimates are provided resulting in a lower initial covariance matrix. If no *a priori* state information exists the filter can be initialized by setting the diagonal elements of the state covariance matrix to infinity, or the reciprocal of machine epsilon for computer implementation, with the off-diagonal elements equal to zero and an arbitrary state vector, such as all zeros. Initialization of the state covariance matrix to infinity will essentially have the filter ignore the initial

state estimate and act exactly like a recursive filter if there is no process noise. If process noise is present the filter will ignore the initial state estimate and behave as a pseudo-recursive filter until the covariance matrix and state vector are updated and propagated.

Verification of proper steady-state filter operation online is performed by comparing the state error residuals with the bounds imposed by the state covariance matrix. The state errors are computed from the difference between the estimated states and the input measurements. Ideally the state error would be calculated using the true states but if the true states are known there is no need for a filter. The diagonal elements of the state covariance matrix represent are the variances of the estimated states allowing for comparison of the state error with the one and three standard deviation value to verify proper steady-state operation and the appropriate order of the filter state model. The covariance analysis presented in the simulation section uses the true state values for error calculations. The on-line residual covariance analysis is presented in the Nonlinear Model Phase II simulation section.

For proper operation from a statistical standpoint, approximately 68% of the state error must lie within the 1σ bounds and approximately 99% must lie within the 3σ bounds calculated from the state covariance matrix. These percentages come from the assumption the Kalman Filter is operating with Gaussian distributed data or the filter has received enough measurements to approximate the distribution as Gaussian according to the *Central Limit Theorem*, see Appendix D. Only the steady-state operation can be verified since the state covariance update and propagation equations do not take system inputs into account.

The comparison between state error and the covariance provides insight on the effectiveness of the order of the state-space model. A lower order filter will provide superior noise reduction over a higher order filter with the tradeoff of potential divergence due to the neglect of higher order derivatives. If the filter diverges out of the standard deviation bounds after being inside the bounds for a time, a higher order model should be considered or process noise should be added to the highest derivative with the drawback of additional steady-state error [34]. On the other side, if the filter is operating within bounds and the highest derivative state can be considered negligible, it will be computationally advantageous to implement a lower order filter.

Design of a Linear Discrete Kalman Filter Design for a Rate Gyro

The direction of this research requires the development of an algorithm and device to estimate a rate gyro bias and accurately track the attitude of a vehicle given an array of accelerometers and a rate gyro. Development of an EKF for this application would involve linearization of the rigid body equations given in Section 2.1.2 used in conjunc-

tion with aircraft force and stability derivative equations given in Appendix F. The result would be a linearized model only for the particular aircraft and not a universal application due to the nonlinearities of the six degree-of-freedom model linearized. For use of the device and algorithm in a variety of applications, a linear discrete Kalman filter was developed to filter the sensed attitude and estimate a rate gyro bias using only information from the rate gyro and accelerometers.

Construction of the linear discrete Kalman Filter requires implementation of equations modeling the attitude rate output from the rate gyro and the rate gyro bias using [8, 10, 30] for Euler Attitude state equations. Equation 2.51 is applied to form the gyro output of longitudinal rate, $\dot{\theta}$, and modeled in Equation 2.64 as the estimated rate, $\tilde{\omega}$, in the presence of white Gaussian sensor noise, η_G, and a sensor bias, β. Accounting for inaccuracies arising from bias drift, the drift rate is modeled by a random walk process dictated by white Gaussian noise, η_B, shown in Equation 2.65. Both white Gaussian noise processes are described by the variances of σ_G^2 and σ_B^2 respectively that are obtained experimentally.

$$\dot{\theta} = \tilde{\omega} - \beta - \eta_G \tag{2.64}$$

$$\dot{\beta} = \eta_B \tag{2.65}$$

The expected values of Equations 2.64 and 2.65 are calculated by taking the expectations of the equations according to Appendix D.1, yielding Equations 2.66 and 2.67. Equation 2.67 implies that the bias estimate is constant over the prediction interval of sample time "dt"but not necessarily over the entire simulation.

$$\hat{\dot{\theta}} = \tilde{\omega} - \hat{\beta} \tag{2.66}$$

$$\hat{\dot{\beta}} = 0 \tag{2.67}$$

The continuous time state-space state equation is given by Equation 2.68 must then be converted to discrete time given by Equation D5 in Table 2.3

$$\dot{\mathbf{x}}(t) = \begin{bmatrix} 0 & -1 \\ 0 & 0 \end{bmatrix} \begin{pmatrix} \theta \\ \beta \end{pmatrix} + \begin{pmatrix} 1 \\ 0 \end{pmatrix} \omega + \begin{bmatrix} -1 & 0 \\ 0 & 1 \end{bmatrix} \begin{pmatrix} \eta_G \\ \eta_B \end{pmatrix} \tag{2.68}$$

In the discrete domain, Φ_k was calculated using Section D.2, the input distribution matrix remains constant, and the process noise distribution matrix becomes the identity matrix since the negative sign is repositioned into the noise vector. Equation 2.68 becomes Equation 2.69 with the matrices defined in Equation 2.70.

$$\begin{pmatrix} \theta_{k+1} \\ \beta_{k+1} \end{pmatrix} = \Phi_k \begin{pmatrix} \theta_k \\ \beta_k \end{pmatrix} + \Gamma_k \tilde{\omega} + \Upsilon_k \begin{bmatrix} g_k \\ b_k \end{bmatrix} \tag{2.69}$$

$$\Phi_k = \begin{bmatrix} 1 & -dt \\ 0 & 1 \end{bmatrix},\ \Gamma_k = \begin{bmatrix} dt \\ 0 \end{bmatrix},\ \Upsilon_k = \begin{bmatrix} 1 & 0 \\ 0 & 1 \end{bmatrix} \tag{2.70}$$

Where: $dt = t_{k+1} - t_k$

The variables g_k and b_k reflect the influence of the bias and gyro noise parameters on the propagation of the states, θ and β, and are defined in Equations 2.71 and 2.72, respectively.

$$g_k = \int_{t_k}^{t_{k+1}} \left[-\eta_G(\tau) - (t_{k+1} - \tau)\,\eta_B(\tau)\right] d\tau \tag{2.71}$$

$$b_k = \int_{t_k}^{t_{k+1}} \eta_B(\tau)\, d\tau \tag{2.72}$$

These parameters are used to calculate the process noise covariance matrix, $\mathbf{Q}_k$, in Equation 2.73 given the state transition matrix, the process noise distribution matrix, and the noise spectral density matrix, $\mathbf{Q}$' given in Equation 2.74.

$$\mathbf{Q}_k = \int_{t_k}^{t_{k+1}} \mathbf{A}(t_{k+1}, \tau)\,\mathbf{G}(\tau)\,\mathbf{Q}'(\tau)\,\mathbf{G}^T(\tau)\,\mathbf{A}^T(t_k, \tau)\, d\tau \tag{2.73}$$

$$\mathbf{Q}'(\tau) = \begin{bmatrix} \sigma_G^2 & 0 \\ 0 & \sigma_B^2 \end{bmatrix} \tag{2.74}$$

Equation 2.73 becomes integration of Equation 2.75 after the matrix multiplication is carried out assuming the bias random walk process and the gyro noise are uncorrelated.

$$\mathbf{Q}_k = \begin{bmatrix} E\{g_k^2\} & E\{g_k b_k\} \\ E\{g_k b_k\} & E\{b_k^2\} \end{bmatrix} = \begin{bmatrix} \sigma_G^2 dt^2 + \frac{1}{3}\sigma_B^2 dt^3 & -\frac{1}{2}\sigma_B^2 dt^2 \\ -\frac{1}{2}\sigma_B^2 dt^2 & \sigma_B^2 dt \end{bmatrix} \tag{2.75}$$

The measurement model of the longitudinal rotation angle taken from the accelerometer measurements in the presence of noise, $\mathbf{v}_k$ with variance $R_k = \sigma_A^2$, is given by Equation 2.76.

$$\tilde{y} = \theta_k + \mathbf{v}_k \tag{2.76}$$

The linear discrete time state-space equations for the Kalman Filter derived are given in Equation 2.77.

$$\begin{gathered} \mathbf{x}_{k+1} = \Phi_k \mathbf{x}_k + \Gamma_k \tilde{\omega} + \mathbf{w}_k \\ \tilde{y} = \Lambda_k \mathbf{x}_k + \mathbf{v}_k \\ \mathbf{x} = [\theta\ \beta]^T,\ \Phi_k = [dt\ 0]^T,\ \Lambda_k = [1\ 0],\ \mathbf{Q}_k = E\left\{\mathbf{w}_k \mathbf{w}_k^T\right\} \end{gathered} \tag{2.77}$$

The state model given in Equation 2.77 can be implemented in the Linear Discrete Kalman Filter Algorithm given in Table 2.3 when the variances and time interval are known. The residual for the output states is computed using Equations 2.78 and 2.79 for checking proper steady-state operation of the filter online.

$$M_k = \Phi_k P_k^- \Phi_k^T + Q_k \tag{2.78}$$

$$Res = \Lambda_k M_k \Lambda_k^T + R_k \tag{2.79}$$

The bias for the simulation can be estimated by tracking the value of the second element of the state matrix, $\mathbf{x}$. The output matrix, $\mathbf{C}$, does not consider the bias state because it cannot be directly measured, only derived from the absolute motion output from the accelerometers when compared with the relative motion output of the rate gyro.

Variance Sensitivity of Derived Linear Discrete Kalman Filter

The sensitivity of the Linear Discrete Kalman Filter to the variances and time step can be examined by multiplying out the Kalman Gain along with the state and covariance updates and propagation. Equations 2.80, 2.81, 2.82, 2.83, and 2.84 display the Kalman Gain, state update, covariance update, state propagation, and covariance propagation sensitivities respectively.

$$K_k = \begin{pmatrix} P_{11}^- & P_{12}^- \\ P_{21}^- & P_{22}^- \end{pmatrix} \begin{bmatrix} 1 \\ 0 \end{bmatrix} \left[[1\ 0] \begin{pmatrix} P_{11}^- & P_{12}^- \\ P_{21}^- & P_{22}^- \end{pmatrix} \begin{bmatrix} 1 \\ 0 \end{bmatrix} + \sigma_A^2 \right]^{-1} = \begin{pmatrix} \frac{P_{11}^-}{P_{11}^- + \sigma_A^2} \\ \frac{P_{21}^-}{P_{11}^- + \sigma_A^2} \end{pmatrix} \tag{2.80}$$

$$\mathbf{x}_k^+ = \mathbf{x}^- + K_k \left[y - \mathbf{C}\mathbf{x}^- \right] = \begin{pmatrix} \theta^- \\ \beta^- \end{pmatrix} + K_k \left[\theta_A - \mathbf{x}_{11}^- \right] = \begin{pmatrix} \theta^- + \frac{P_{11}^- \left(\theta_A - \theta^- \right)}{P_{11}^- + \sigma_A^2} \\ \beta^- + \frac{P_{21}^- \left(\theta_A - \theta^- \right)}{P_{11}^- + \sigma_A^2} \end{pmatrix} \tag{2.81}$$

Where θ_A is the pitch measurement from the accelerometers

$$P_k^+ = \left[\mathbf{I}_{2\times 2} - K_k \mathbf{C} \right] P^- = \begin{pmatrix} P_{11}^- \left(1 - K_{11} \right) & P_{12}^- \left(1 - K_{11} \right) \\ -K_{21} P_{11}^- + P_{21}^- & -K_{21} P_{12}^- + P_{22}^- \end{pmatrix} \tag{2.82}$$

Where $\mathbf{I}_{2\times 2}$ is a 4 element Identity Matrix

$$\mathbf{x}_{k+1}^{-} = \mathbf{A}\mathbf{x}_{k}^{+} + \mathbf{B}\omega = \begin{pmatrix} \theta^{+} - \beta^{+}dt + \omega dt \\ \beta^{+} \end{pmatrix} \tag{2.83}$$

$$P_{k+1}^{-} = \mathbf{A}P^{+}\mathbf{A}^{T} + Q_k = \begin{pmatrix} P_{11}^{+} - P_{21}^{+}dt - \left(P_{12}^{+} - P_{22}^{+}dt\right)dt & P_{12}^{+} - P_{22}^{+}dt \\ P_{12}^{+} - P_{22}^{+}dt & P_{22}^{+} \end{pmatrix} + Q_k \tag{2.84}$$

The Kalman Filter sensitivity to measurement noise is shown in Equations 2.80 and 2.81 where the Kalman Gain is inversely proportional to the measurement noise and the state update consideration of the error between the system output and measurements is directly proportional to the Kalman Gain. With high accuracy measurements, the noise variation is lower resulting in a higher Kalman Gain and a larger impact of the error between the model output and measurement. Equations 2.82 and 2.84 show a Kalman Gain increase will result in lower state covariance values when updated and propagated as long as Q_k remains unchanged.

The filter sensitivity to process noise is shown in Equation 2.75 where the diagonal elements of the process noise matrix are proportional to noise and the off-diagonal elements are inversely proportional due to the negative sign. When summed in the state covariance propagation, the diagonal elements are added while the off-diagonal elements are subtracted. The state covariance matrix is a measure of how the states vary together and separately and is desired to be as small as possible to provide reliable tracking. From Equation 2.80, if the covariance elements become smaller than the measurement noise, the Kalman gain will go to 0 and if the covariance elements become larger than then measurement noise the Kalman gain will go to 1. This is an intuitive check because the less the states vary, the less they need to be updated and vice-versa.

To reduce the off-diagonal state covariance elements, the bias noise variance can be increased to account for a wider range of bias values due to a time varying bias or modeling uncertainties. By increasing the bias noise variance, the diagonal state covariance elements are increased leading to larger Kalman Gain values. In the same fashion, the gyro noise variance can be increased to account for a larger range of possible theta estimates. If the rate gyro possesses a large variance in noise and a time varying bias, increasing the process noise variances will allow the Kalman Filter to converge faster on the gyro bias.

By tuning only the measurement and process noise variances depending on the type of data produced from the sensor, there is little need to tune the initial conditions of the state vector and state covariance matrix because the update and propagation of both

matrices allow for speedy convergence to appropriate values. Ideally if there is no process or measurement noise in the system, the state error will converge to zero as more measurements are taken and the real world system is accurately modeled. When process noise is added to the system model, the state error will reach a steady-state value that will not decrease even when there are subsequent measurements. The filter assumes there is always a certain amount of noise present in the signal even when in reality there may not be any. Care must be taken not to significantly increase the noise parameters else a steady state error may introduced that the filter is unable to overcome. The process noise parameters can be obtained through experimental sensor testing using Monte Carlo analysis and a variety of operating scenarios.

The initial estimate of the state covariance matrix has little effect on the convergence of the filter except when the diagonal terms are set equal to zero. Setting the diagonal terms equal to zero assumes perfect sensor measurements and does not allow the state covariance matrix to update resulting in an ineffective filter. The diagonal terms of the initial state covariance matrix can be set to zero because this assumes the states are uncorrelated while the diagonal terms can be set to a near zero value to provide faster convergence compared to values greater than 1. The state vector can be set to zeros if there is no *a priori* knowledge of the rate gyro bias and the vehicle is assumed to start from an initial pitch of zero degrees.

Chapter 3

Simulation Models and Algorithm Operation

3.1 Vehicle Plant Models

3.1.1 Linear Model

A linear plant model was constructed to produce a longitudinal angular displacement and rate for assessment of device operation and the estimation algorithm. The device was considered to rotate about an axis parallel with ground level with gravity as the applied translational acceleration to simulate a test platform purely rotating the device. Figure 3.1 shows how the outputs of the linear model were used in generation of the corrupted rate gyro and accelerometer signals along with the addition of signal noise and bias.

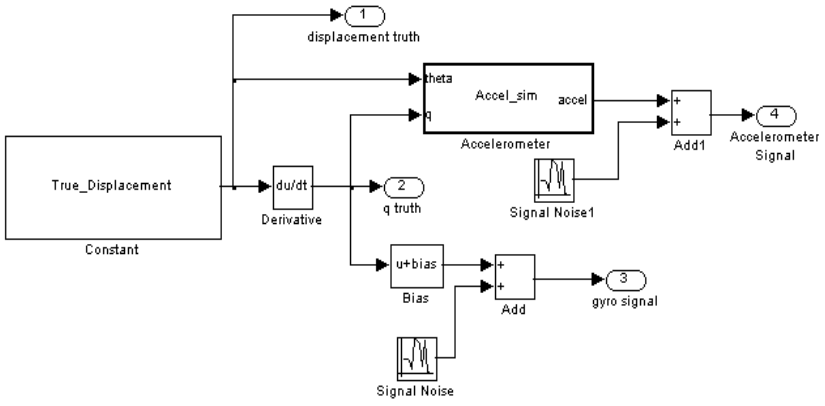

Figure 3.1: Linear Plant Model

The true angular displacement for three different simulations was generated using three different signal types: a 1 radian magnitude Sine wave at 1 Hertz, a time-delayed 60 degree step and hold maneuver, and a double ±85 degree pitch doublet maneuver with each doublet lasting 20 seconds.

3.1.2 Nonlinear Aircraft Model

A nonlinear six degree of freedom aircraft model was implemented to assess the performance of the device and observer algorithm in a simulated real-world environment. The rigid-body equations given in Section 2.1.2 were used in conjunction with the aircraft force and stability derivative equations given in Appendix F for accurate representation of an aircraft response to the surrounding environment and control surface inputs. The control surface inputs are implemented with step inputs to a first order linear actuator model with a 10 millisecond time delay. Appendix F displays the Simulink model used for simulation of the nonlinear model.

The nonlinear model was applied to the device and attitude estimation algorithm in two steps. First, the device and algorithm were subjected to the nonlinear model with rotational acceleration and gravitational loading while neglecting imposed loading from aerodynamic and thrust forces. This preliminary step was performed for comparison with the linear model and for assessment of any discrepancies arising from nonlinear measurements before moving on to full longitudinal loading from the nonlinear model. The second step was application of full longitudinal loading of the device consisting of rotation acceleration and imposed loading effects due to thrust and aerodynamic forces along the primary and tertiary axes. The inertial loading of the secondary vehicle axis was considered negligible since the roll and yaw angles and rates were held at zero.

3.2 Device Model

The previously proposed [7] attitude estimation device consists of 13 one-axis accelerometers spaced even about a 180 degree semi-circle on a 3 inch radius with a one-axis rate gyro at the center perpendicular to the accelerometer measurement plane. The device is assumed to be oriented such that the device axes are collinear with the vehicle's axes as shown in Figure 3.2 with the red axes indicating the reference coordinate system, the black axes indicating the device coordinate system, and the blue axes indicating the vehicle coordinate system. The accelerometer spacing in the longitudinal plane starts at -180 degrees pitch and proceeds counterclockwise to 0 degrees pitch. In the arrangement, Accelerometer 4 is set at a pitch attitude of -135 degrees and Accelerometer 10 is set at a pitch attitude of -45 degrees from the vehicle's primary axis.

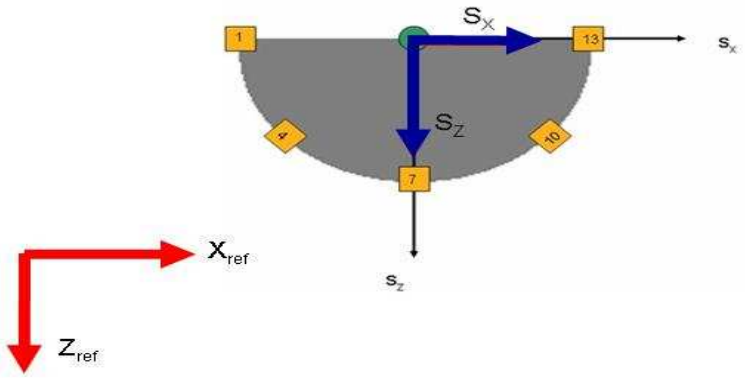

Figure 3.2: Gyro-Accelerometer Device with Vehicle Pitch of 0 degrees

This work utilizes 13 accelerometers because it a feasibility study on the expansion and enhancement of previous research performed in [7] for cost-effective real-world nonlinear environment attitude and sensor bias estimation. The device can be scaled up or down in terms of the number of accelerometers depending on the magnitude of the vehicle maneuvers and the required accuracy during dynamic operation.

3.2.1 Static Operation

When the vehicle is operating in its trim condition, no imposed translational or rotational acceleration loads, the accelerometer readings can be used to calculate the vehicle's attitude. For the case when the vehicle's primary axis is parallel with the ground and Accelerometer 7 is parallel with the vehicle's tertiary axis, the remaining accelerometer measurements, gA_i, are a function of their offset angle, θ_i, from the vehicle's tertiary axis, given by Equation 3.1.

$$gA_{z,i} = g\cos(\theta_i) \tag{3.1}$$

Where "g"represents the acceleration of gravity in gees, where 1 gee is equivalent to $9.81\mathrm{m/s}^2$ or 32.17 $\mathrm{ft/sec}^2$. The offset angle is measured negative clockwise from the vehicle's tertiary axis and positive clockwise. Appendix E.1 lists the accelerometer offset angles used in this work. The accelerometer measurements for any static condition when the vehicle pitch angle $\theta_{Maneuver}$ is not zero is given by Equation 3.2. This equation holds true because the only acceleration measured during static operation is due to the gravity vector. Figure 3.3 shows the vehicle with the device mounted at the center of gravity at a static orientation of +30 pitch.

$$\mathrm{gA}_{z,i} = g\cos(\theta_{Maneuver} + \theta_i) \tag{3.2}$$

The angle calculation using accelerometer data is performed by solving Equation 3.2 for $\theta_{Maneuver}$ and is shown in Equations 3.3 and 3.4. The magnitude of the maneuver angle

is back-calculated using Equation 3.3 with the direction of the longitudinal displacement given by the sign of Accelerometer 1. For maneuvers of the set (0,+180) degrees, the accelerometer reading, $gA_{z,1}$, is positive and negative for maneuvers of the set (0,-180) degrees yielding Equation 3.4. For the cases of a 180 or 0 degree displacements, Accelerometer 7 will measure +1 gee or -1 gee respectively allowing for complete static attitude resolution.

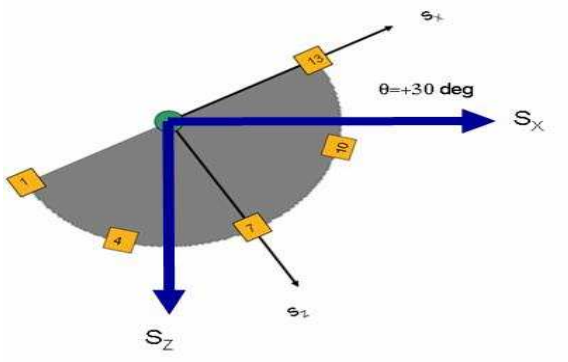

Figure 3.3: Gyro-Accelerometer Device with Vehicle Pitch of 30 degrees

$$|\theta_{Maneuver}| = \arccos\left(gA_{z,i}\right) - |\theta_{i,static}| \tag{3.3}$$

$$\theta_{Maneuver} = |\theta_{Maneuver}| * sign\left(gA_{z,1}\right) \tag{3.4}$$

3.2.2 Longitudinal Loading of an arbitrary located device

For simulation of accelerations measured by an arbitrary located device undergoing both translational and rotational acceleration loading, the translational accelerations of the vehicle along the vehicle axes along with the vehicle rotation rates must be resolved to the device sensor locations. The measured acceleration of an arbitrary accelerometer displaced from the vehicle's center of gravity is derived in Appendix E.2. The angles given in Equation 3.5 represent the misalignment angles of the "ith"sensor with the vehicle axes. The vehicle rotation rates are given by p, q, and r with their subsequent derivatives of $\dot{p}$, $\dot{q}$, and $\dot{r}$ and the displaced distances along each axis are given by $\bar{x}$, $\bar{y}$, and $\bar{z}$.

$$\begin{aligned} gA_{z,i} = &\left[gA_{x,CG} - \left(r^2+q^2\right)\bar{x} + \left(pq-\dot{r}\right)\bar{y} + \left(pr+\dot{q}\right)\bar{z}\right] * \\ &\left(\cos\phi_i \sin\theta_i \cos\phi_i + \sin\psi_i \sin\phi_i\right) + \\ &\left[gA_{y,CG} + \left(pq+\dot{r}\right)\bar{x} - \left(p^2+r^2\right)\bar{y} + \left(qr+\dot{p}\right)\bar{z}\right] * \\ &\left(\sin\psi_i \sin\theta_i \cos\phi_i + \cos\psi_i \sin\phi_i\right) + \\ &\left[gA_{z,CG} + \left(pr-\dot{q}\right)\bar{x} + \left(qr+\dot{p}\right)\bar{y} + \left(q^2+p^2\right)\bar{z}\right] * \left(\cos\theta_i \cos\phi_i\right) \end{aligned} \tag{3.5}$$

The translational accelerations along the vehicle's axes are given by the resultant of the imposed inertial loads due to vehicle acceleration and the resolution of the gravity vector along each axis. These accelerations are given by Equation 3.6.

$$g\begin{Bmatrix} A_x \\ A_y \\ A_z \end{Bmatrix}_{CG} = \begin{Bmatrix} A_x \\ A_y \\ A_z \end{Bmatrix}_{Imposed} + g\begin{Bmatrix} -\sin\theta \\ \cos\theta\sin\phi \\ \cos\theta\cos\phi \end{Bmatrix}_{Man} \tag{3.6}$$

For pure longitudinal motion, the roll and yaw angles are zero along with their subsequent derivatives, reducing Equation 3.5 to Equation 3.7 given the sensor misalignment only in the longitudinal plane.

$$gA_{z,i} = \left[gA_{X,CG} - q^2\bar{x} - \dot{q}\bar{z}\right]\sin\theta_z + \left[gA_{z,CG} - \dot{q}\bar{x}_z + q^2\bar{z}_z\right]\cos\theta_z \tag{3.7}$$

Since the sensors are mounted about a semicircle with a set radius, r_d, with a specified misalignment angle measured from the vehicle tertiary axis, θ_i, Equation 3.7 can be simplified using polar notation for $\bar{x}$ and $\bar{z}$.

$$\begin{aligned} \bar{x} &= r_d\sin\theta_i \\ \bar{z} &= r_d\cos\theta_i \\ gA_{z,i} &= gA_{X,CG}\sin\theta_i + gA_{Z,CG}\cos\theta_i - r_dq^2 \end{aligned} \tag{3.8}$$

By substituting Equation 3.6 into Equation 3.8, the accelerometer measurements can be simulated when the imposed acceleration from translational movement, Euler orientation, and pitch rate of the vehicle are known, as shown in Equation 3.9. This equation simulates the full acceleration loading for an accelerometer displaced from the vehicle center of gravity in the plane formed by the device's, thus vehicle's, primary and tertiary axes.

Simulation of Accelerometer under Full Longitudinal Loading

$$gA_{z,i} = (A_{X,Imp} - g\sin\theta_{Man})\sin\theta_i + (A_{Z,Imp} + g\cos\theta_{Man}\cos\phi_{Man})\cos\theta_i - r_dq^2 \tag{3.9}$$

The above equation is used to simulate the accelerometer measurements when the device is mounted in an aircraft. For pure longitudinal rotational motion there are no imposed translation acceleration or inertial loads due to vehicle motion, only the acceleration due to rotational motion and the gravity vector. Thus, Equation 3.9 reduces to 3.11 when the vehicle is purely rotating in the longitudinal plane.

Simulation of Accelerometer under Pure Rotation

$$gA_{z,i} = (-g\sin\theta_{Man})\sin\theta_i + (g\cos\theta_{Man})\cos\theta_i - r_dq^2 \tag{3.10}$$

Applying the trigonometric identity of $\cos(\alpha + \beta) = \cos\alpha\cos\beta - \sin\alpha\sin\beta$, we find Equation 3.10 becomes 3.11

$$gA_{z,i} = g\cos(\theta_{Maneuver} + \theta_i) - r_d q^2 \tag{3.11}$$

The above equation is used to simulate accelerometer readings when the device is mounted to a rotating testbed. When the vehicle is static, Equation 3.11 becomes Equation 3.2.

3.3 Algorithm Operation

The algorithm uses data from the rate gyro and accelerometers to calculate a pitch attitude estimate and rate gyro bias continuously during static conditions or discretely during maneuvers. The bias is estimated by differencing the integrated rate gyro signal with the angle calculated from the rate gyro signals. For the pitch attitude estimate, the initial condition of the rate gyro integration is reset to the angle estimated by the accelerometers. Before a bias is estimated, the rate gyro signal is passed through a second order low pass filtered derivative transfer function to estimate the pitch acceleration for determination of vehicle operation in either a static or dynamic regime. The accelerometer signals are passed through a Butterworth filter to reduce the signal noise. Figure 3.4 shows the algorithm placement for estimation of the rate gyro bias to be subtracted from the corrupted rate gyro signal continuously along with providing rate gyro integration initial conditions due to static or dynamic environment triggers.

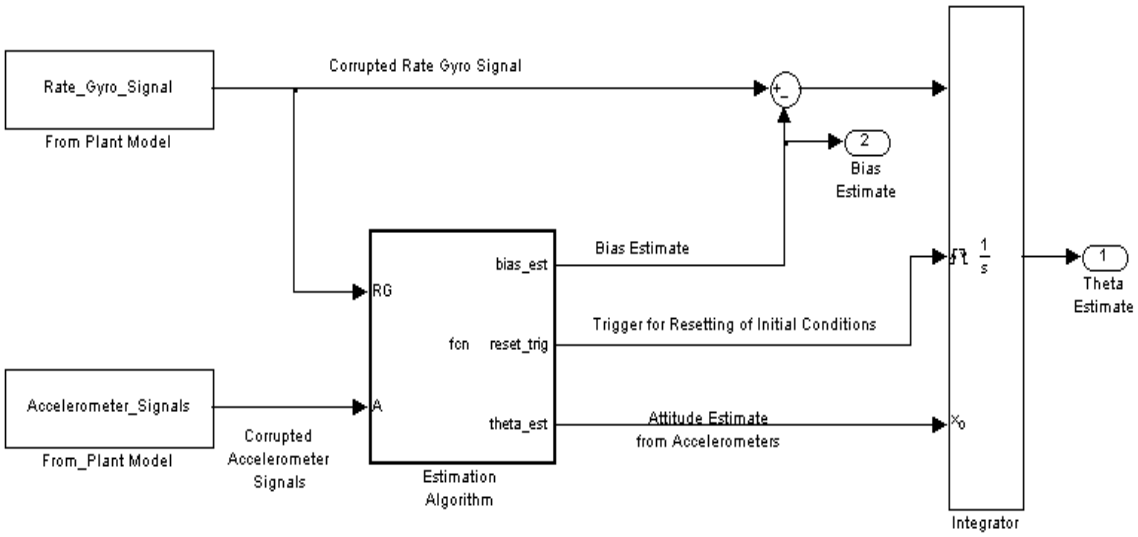

Figure 3.4: Algorithm Placement

When the vehicle is experiencing significant rotational acceleration the rate gyro bias and attitude estimate from accelerometer signals can only be estimated at discrete trigger points while the same parameters can be continuously estimated during static operation where significant rotational motion is lacking. A dynamic trigger occurs when the difference between two consecutive accelerometer measurements is less than a predefined threshold, $a_{z,thres}$, and the pitch acceleration is above another predefined threshold, $\ddot{\theta}_{thres}$. Static triggering occurs when the filtered derivative of the pitch rate is below the predefined threshold for a given length of time. During static operation, the attitude is estimated by averaging acceptable accelerometer angle measurements calculated from Equation 3.4. Acceptable accelerometer measurements are measurement magnitudes less than an established saturation threshold of 0.975 gee. This threshold filter was established to avoid signal noise from pushing the signal measurement past a 1 gee magnitude, resulting in complex output of the arc-cosine function.

3.3.1 Back-Differencing Bias Estimation

A combined bias estimator using static and dynamic environment estimators described in Section 2.3.2 was constructed using the Euler attitude representation then transitioned to the Quaternion attitude representation for additional robustness and ability for expansion into three dimensions. The bias and attitude estimation algorithm is shown in Figure 3.5 with the dynamic bias calculation at discrete points shown in Figure 3.6.

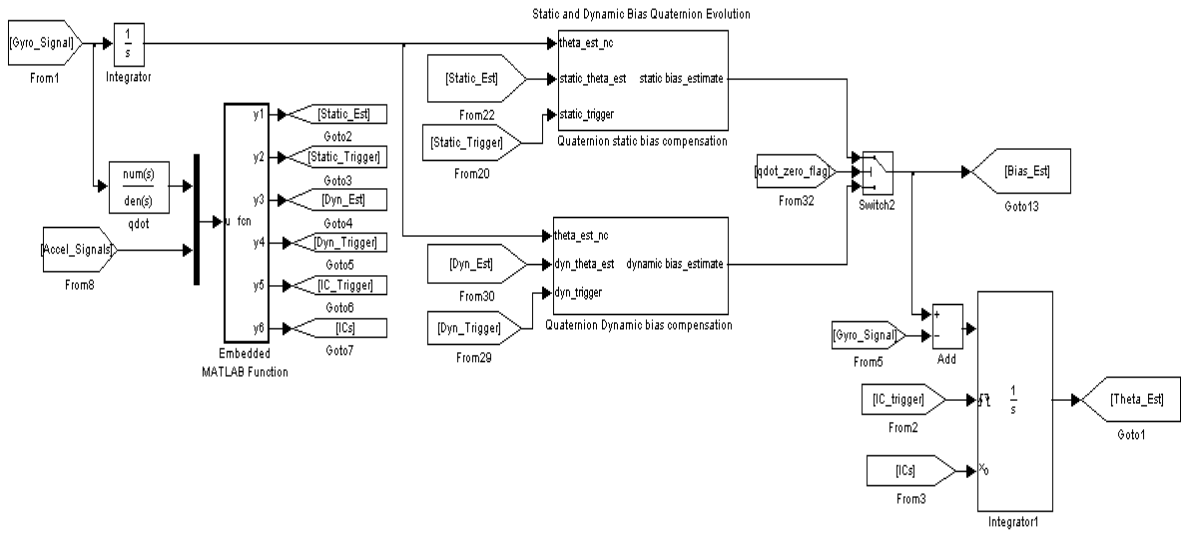

Figure 3.5: Back-Differencing Bias Calculation Flow Chart

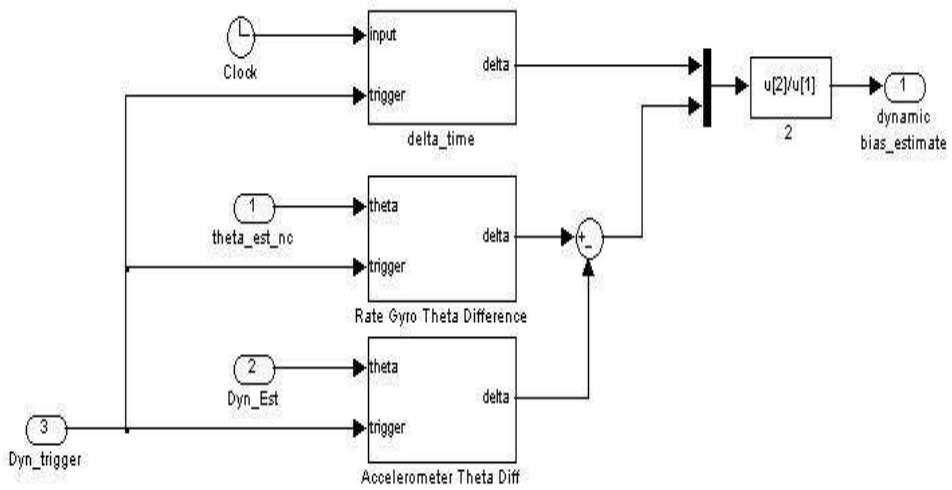

Figure 3.6: Dynamic Bias Estimation

The dynamic estimate from the accelerometers was kept the same as in [7] but the static longitude angle estimate was altered to improve accuracy by including unsaturated accelerometers to combat the noise corrupted accelerometer signals. The acceleration reading of all accelerometers below a given threshold, $gA_{z,staticthres}$, were each resolved into an angular position estimate given the accelerometer positions and Equation 3.4 then averaged to produce a static angle orientation estimate. The saturation threshold was set at 0.975 gee for the linear plant model simulations. The Back-Differencing Algorithm was implemented in the linear and nonlinear plant model simulations but only utilized in the linear plant model simulation due to the robustness and effectiveness of the Linear Discrete Kalman Filter.

3.3.2 Kalman Filter Bias Estimation

A linear discrete Kalman Filter model was constructed to estimate the rate gyro bias and vehicle attitude using the fusion of the rate gyro signal, estimated attitude from the accelerometers, and a linear system model of a rate gyro given in Section 2.3.3. The initial estimate of the state vector is set at zero degrees pitch displacement and a bias of zero degrees per second. The process noise variances of the rate gyro and the measurement noise covariance of the accelerometers can only be determined experimentally, the initial values used in [8] were applied to give a baseline for operation then tuned to increase effectiveness. The model used for the LDKF implementation is given in Figure 3.7.

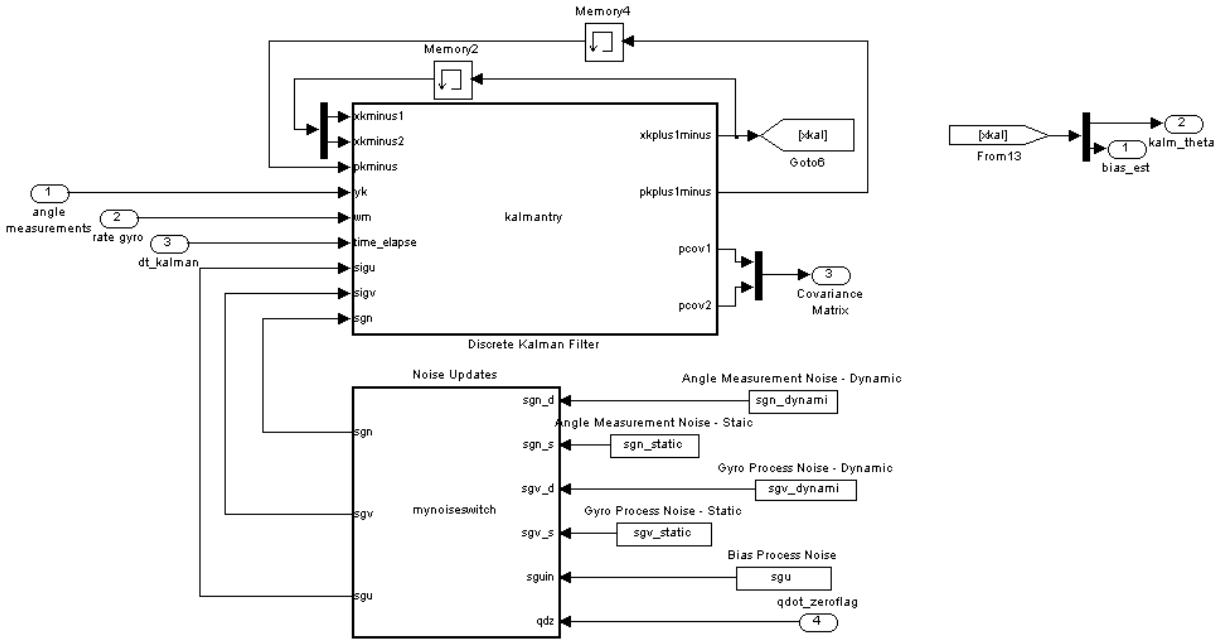

Figure 3.7: Kalman Filter Diagram

The LDKF in Figure 3.7 relies on the rate gyro measurement, the attitude estimate from the accelerometer, and the noise covariances for the gyro, bias, and accelerometer measurements. The gyro process and angle measurement noise covariances have two values that are switched between depending on the operating environment of the aircraft. The need for two variance values depending on the operating regime is predicated on the measurements of the accelerometers being less accurate during maneuvers because of their absolute sensing nature resulting in less triggering for rate gyro integration initial conditions leading to a larger gyro signal variance. The rate gyro bias is assumed to be unaffected by operating conditions, allowing for a constant variance. The rate gyro bias is assumed to be constant because once the rate gyro reaches its proper operating point, with constant temperature, the bias varies insignificantly.

3.3.3 Hardware Configuration Considerations

The configuration along with the operating condition of the rate gyro and accelerometer based device impacts the precision of the bias and attitude estimation algorithm described prior. The following subsections address the issues of rate gyro operation condition, the number of accelerometers used, and the procedure for handling a failed accelerometer.

Rate Gyro Operating Condition

An online check of the rate gyro operating condition can be performed using measurements of the accelerometer located at the vehicle center of gravity measuring acceleration along the tertiary axis, $A_{Z,CG}$, and Accelerometer 7, $A_{z,7}$, by rearranging Equation 3.9 isolating the square of the pitch rate magnitude. The square of the pitch magnitudes from the rate gyro minus the estimated bias and Equation 3.9 can be compared online during static operation allowing for a rate gyro reliability check.

Number of Accelerometers

This work conducted research into the feasibility of implementing the device first proposed by [7] into a nonlinear and imposed acceleration loading environment. This work used accelerometer spacing allowing for a bias estimation trigger every 15 degrees during dynamic operation. If 25 accelerometers were used instead of 13, the spacing would allow for bias estimation every 7.5 degrees yielding additional precision due to additional opportunities to estimate the rate gyro bias and reset the rate gyro integration initial conditions. Conversely if the array was reduced to only 5 accelerometers, the opportunity for bias estimation and resetting of the integration initial condition would be reduced to every 45 degrees resulting in a lower attitude estimation accuracy.

Failed Accelerometers

A sensor bypass procedure has been developed if an accelerometer is determined to be malfunctioning via comparison of the accelerometer's signal with its expected measurement during device ground initialization. During the initialization period, a comparison between the accelerometer signal and its expected value computed from the known location of the local gravity with respect to the device location is conducted. If an accelerometer is deemed to be malfunctioning, its signal is ignored and the readings of the adjacent accelerometers are considered. Instead of differencing the failed accelerometer, A_{failed}, with its adjacent properly operating accelerometers, $A_{Left-of-Failed}$ and $A_{Right-of-Failed}$, the signals of the adjacent accelerometers are differenced. When the magnitude of the difference of the adjacent properly operating accelerometers falls below the triggering threshold, a trigger occurs with the integration initial conditions set to the location of the failed accelerometer. Bypassing the failed accelerometer results in decreased accuracy because the device must experience a change of 15 degrees between the two properly operating adjacent accelerometers for a trigger to occur instead of 7.5. As an example, if Accelerometer 10 was deemed malfunctioning, the signals of Accelerometers 9 and 11 would be differenced. As a result, the accuracy of the device is decreased because no triggers can occur at -37.5 or -52.5 degrees pitch since Accelerometer 10 is located at -45 degrees from the primary axis with Accelerometers 9 and 11 located at -60 and -30 degrees from the primary axis respectively yielding a trigger at -45 degrees.

Chapter 4

Simulation Results

4.1 Simulation Overview

For device feasibility analysis, three longitudinal simulations were constructed using both linear and nonlinear system plant models with applied rotational and translational acceleration loading about the primary and/or tertiary vehicle axis. The simulations were constructed and applied to simulate and assess the effectiveness of the device in estimation of the rate bias online while correctly tracking the vehicle longitudinal attitude. The preliminary simulation consists of the device implemented in a linear system experiencing full rotational acceleration and translational acceleration along the tertiary axes. The second simulation consists of the device implemented in a nonlinear aircraft model experiencing full rotational and translational acceleration only along the vehicle's tertiary axis. The second simulation is unrealistic but of great importance of assessing any shortcomings of the device before all longitudinal translational accelerations are applied. The last simulation consists of the device implemented the nonlinear aircraft experiencing full rotational acceleration and translational acceleration along the vehicle's primary and tertiary axis. The last simulation demonstrates the device and algorithm's effectiveness when implemented in a nonlinear system, such as an aircraft, operating under real-world conditions.

The accelerometers were modeled with a white Gaussian noise variance of 0.000015 gee^2 while the gyro was modeled with a white Gaussian noise variance of 0.15 (deg/sec)^2 and a constant bias of 3 deg/sec. Accelerometers measuring the gravity vector to be less than 1 gee minus three standard deviations of the Gaussian white noise for the accelerometers were considered in calculating the static pitch orientation. The vehicle was considered static if the calculation of the angular acceleration was less than 0.2 deg/sec^2 for at least 1 second. For the estimation of angular acceleration, the rate gyro signal was passed through a low-pass second order filtered derivative with a natural frequency

of 1 radian/second and a damping ratio of 0.707. The accelerometer measurements were filtered using a second order Butterworth filter with a cut-off frequency of 40 radians/second resulting in lag of approximately 50 milliseconds when experiencing a pitch rate of 30 radians/second. A dynamic estimate was produced when the difference between two consecutive accelerometers fell below the threshold of 0.0015 gee based on the measurement threshold of integrated circuit accelerometers of 0.001 gee [31].

4.2 Linear Plant Model

4.2.1 Utilized Model

The linear plant maneuver model constructed in 3.1.1 was used to assess the feasibility of the proposed device before implementation in a nonlinear six degree of freedom vehicle simulation. The three maneuvers used for operation assessment were a 1 radian magnitude Sine wave at 1 Hertz, a time-delayed 60 degree Step-and-Hold maneuver, and a double ±85 degree, 20 second, pitch doublet maneuver. The quaternion form of the back-differencing algorithm was implemented to estimate the rate gyro bias. The linear discrete Kalman filter derived in Section 2.3.3 was applied to the pitch doublet maneuver and compared with the quaternion back-differencing algorithm.

4.2.2 Back-Differencing Bias Estimation

The back-differencing algorithm and gyro reinitialization were implemented in a linear attitude model and evaluated for bias estimation and attitude tracking effectiveness with a variety of maneuvers. Figure 4.1 displays the attitude estimate comparison between the pure integration of rate gyro signal with no modification while reinitializing the rate gyro integration initial conditions at dynamic trigger points. Dynamic and static compensation are turned "off"in the left plot with the absolute error between the true attitude and the reinitialized estimate in the right plot. Estimation of the bias and noise effects are improved at discrete points where the bias is calculated and subtracted from the rate gyro and a new initial condition from the trigger accelerometers for integration is set. By continuously subtracting the calculated rate gyro bias from the rate gyro signal until the next dynamic trigger and reinitializing the integration initial conditions at the estimation trigger, the tracking error is significantly reduced for the same maneuver [7]. This is referred to as "dynamic compensation"with its effect is displayed in the left-side plot of Figure 4.2. The right-side plot of Figure 4.2 shows the absolute error between the rate gyro signal integration using dynamic compensation and the true attitude.

In Figure 4.2, having dynamic compensation turned "on"was enough to provide extremely accurate attitude tracking because the maneuver was continually experiencing rotational motion. The need for static compensation is demonstrated via a 60 degree

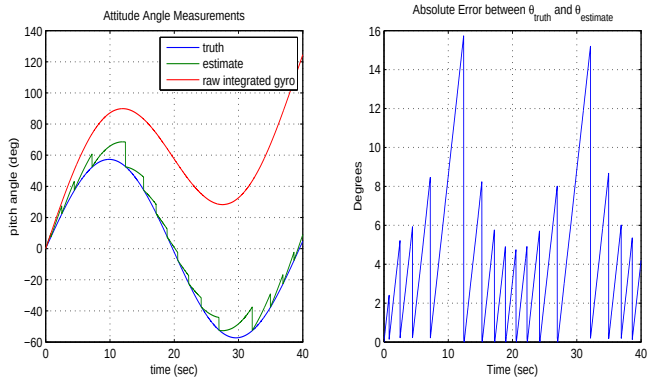

Figure 4.1: Sinusoid Maneuver: Reinitialization of ICs Only

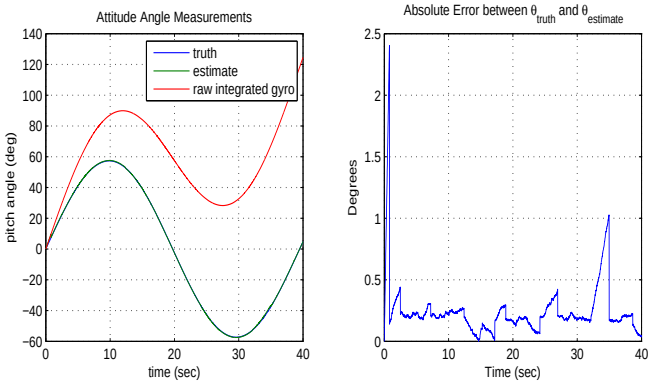

Figure 4.2: Sinusoid Maneuver: Dynamic Compensation "On"

Step-and-Hold maneuver shown with Figure 4.3 where the rate gyro bias is uncorrected after the rotation motion ceases. Turning "on"static compensation drastically reduces attitude estimation error when the sensed rotational motion falls below the pitch acceleration threshold, utilizing both dynamic and static compensation is known as "Full Compensation" [7]. Application of full compensation during dynamic and static operating environments is shown in Figure 4.4.

The rate gyro bias estimates for the Sinusoid and Step-and-Hold Maneuvers are overlaid with comparison to the true bias and shown in Figure 4.5. The rate gyro bias estimates converge within 5 seconds and identify the bias with relative accuracy, the time transient is due to Butterworth filter initialization for accelerometer signal filtering. The Step-and-Hold estimate remains constant since the vehicle is no longer moving while the Sinusoid estimate oscillates discretely due to dynamic triggers from different accelerometers. The accelerometer measurements for each maneuver are given in Appendix E as Figures E.3 and E.2 respectively.

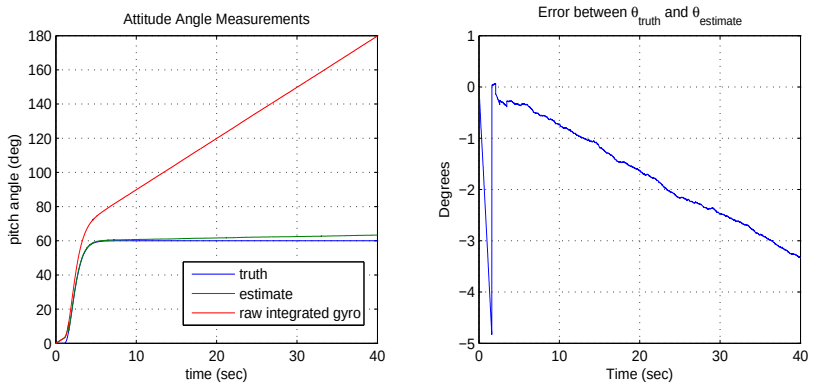

Figure 4.3: Step and Hold Maneuver: Dynamic Compensation Only

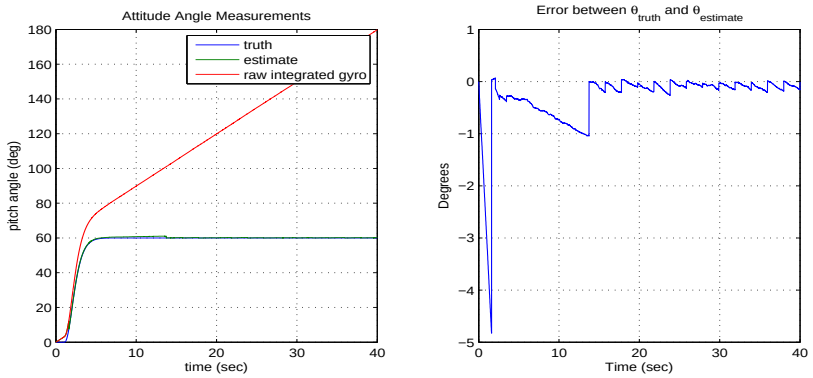

Figure 4.4: Step and Hold Maneuver: Full Compensation

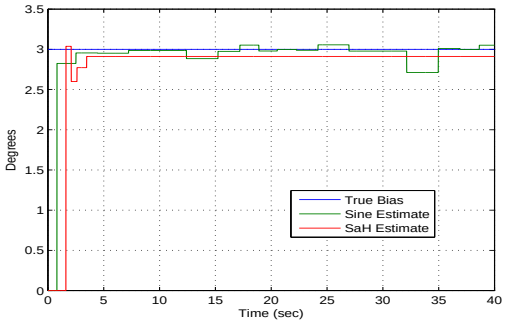

Figure 4.5: Bias Calculation for Sinusoid and Step-and-Hold Maneuvers

The Sinusoid and Step-and-Hold maneuvers were combined to form a ± 85 degree pitch doublet maneuver with each doublet lasting 20 seconds and the second doublet occur-

ring 20 seconds after the end of the first. Figure 4.6 displays the attitude estimation results, left plot, and the error between the true attitude and the Full Compensation estimate, right plot. Both plots in the figure have the first 5 seconds truncated to increase comparison resolution due to an initial large error resulting from Butterworth filter implementation.

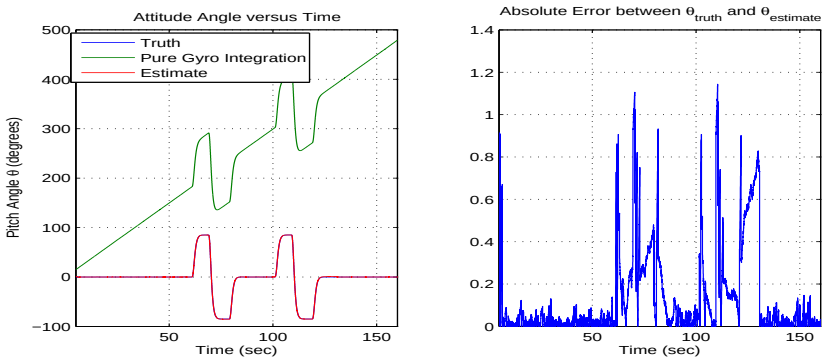

Figure 4.6: Pitch Doublet Attitude Estimates and Absolute Error

Figure 4.7 displays the estimated rate gyro bias for the pitch doublet simulation with bias estimate excursions of 1 degree or more are due to the discrete nature of the dynamic triggers. Since the algorithm back-differences the last dynamic attitude estimate with the present dynamic attitude estimate then divides by the time between the two, error arises as the time between trigger increases. Reducing the angular displacement between the accelerometers from 7.5 degrees to 3.25 degrees the calculated bias would deviate less from the true bias since additional triggering will occur with less of a time gap between triggers. Figure E.4 in Appendix E displays the accelerometer measurements for the doublet maneuver.

For evaluation of a ramping bias, the pitch doublet maneuver was simulated with the bias increasing at a rate of 0.5 degree per second per hour in addition to prior bias and noise parameters corrupting the attitude estimate. This rate equates to a slope of 1.4×10^{-4}deg/sec^2, the small magnitude is a result of rate gyro parameters remaining relatively constant once the rate gyro reaches operating temperature until the gyro fails. The pitch doublet maneuvers occurred during a simulation run length of 3600 seconds for observance of the bias slope on attitude estimation with the maneuvers executed at 1200 and 2400 seconds. Figures G.1 and G.2 in Appendix G display zoomed plots of the attitude estimates and resulting error from the pitch doublet maneuvers. Figure 4.8 and 4.9 plot the attitude error and rate gyro bias estimate over the 3600 second simulation to demonstrate the algorithm's attitude and bias tracking ability. The bias error and

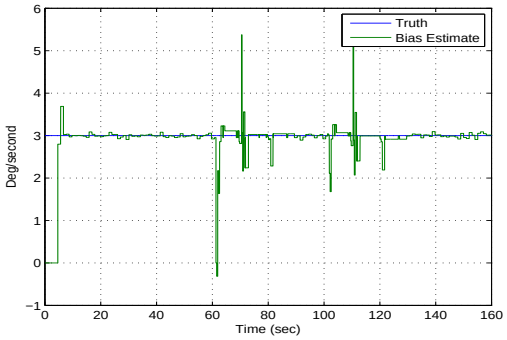

Figure 4.7: Rate Gyro Bias Estimate from Full Compensation

thus attitude error spikes occur when the vehicle is in the middle of the pitch doublet maneuver and can rely on only dynamic triggers for attitude estimation.

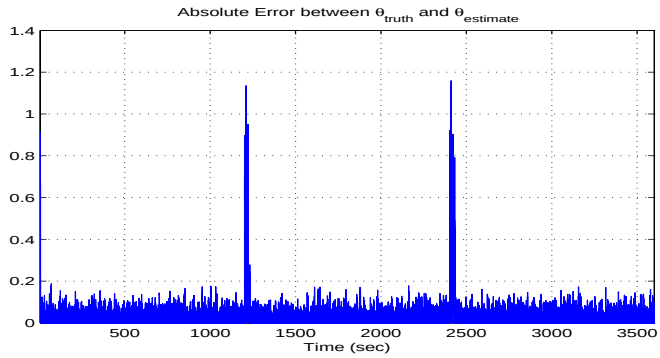

Figure 4.8: Pitch Doublet Attitude Absolute Error

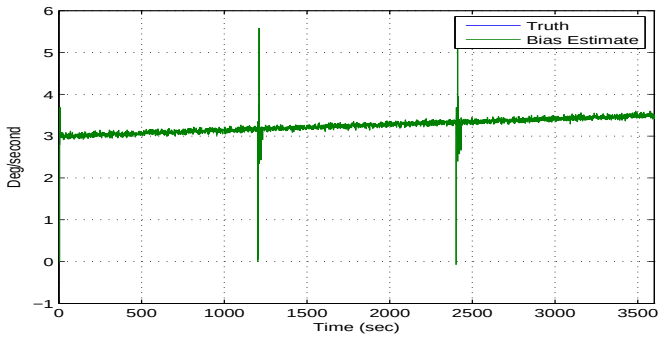

Figure 4.9: Rate Gyro Bias Estimate from Full Compensation

4.2.3 Kalman Filter Bias Estimation

To minimize the impact of outlying discrete dynamic trigger bias estimates shown in Figures 4.8 and 4.9, prior knowledge of the bias estimate must be utilized more effectively. The new estimate is less susceptible to large bias estimate excursions resulting from dynamic maneuvers or oscillating between static and dynamic environments. A polynomial or sinusoid least-squares fit of simulations could effectively compensate for the outlier bias estimates but requires a large amount of data storage, knowledge of the gyro signal form, and can only be performed offline. Additionally, modeling the signal using a polynomial can be a vast undertaking due to the variance of the noise associated with the signal. A least-squares recursive algorithm can be of use since it can be performed in real-time but requires a large amount of memory for data storage with an a priori rate gyro signal general equation. A Kalman Filter is a good candidate for this an application because it relies on a state-space model of the system, uses only the previous system output and measurement data, and has the ability to deal with input signal variances.

A linear discrete Kalman Filter was implemented for estimation of the gyro bias for the pitch doublet maneuver according to Section 2.3.3 over a 160 second time interval. The process and measurement noise standard deviations were assumed to be the same as those given in [8] and are listed in Table 4.1 at the end of this section. The sample time of the Kalman Filter was set to 0.01 seconds with the attitude measurement coming from the accelerometer measurements. The sample rate was constant since there was no imposed acceleration loading on the device allowing for continuous resolution of the accelerometer signals to an attitude estimate over both static and dynamic operating conditions. However, when a dynamic trigger occurred it overrode the resolved estimate because it was instantaneous and not averaged. The simulation time was 160 seconds with a double pitch doublet starting at 60 seconds with the same rate gyro bias and bias slope as the previous section. The Kalman Filter possesses a time-to-converge transient based on its recursive nature and initial parameters and was found to be approximately 6 seconds for the attitude estimate to be within 0.5 degrees of the true attitude. The Kalman Filter was used to estimate the rate gyro bias using attitude estimates from accelerometer measurements while providing filtered initial conditions for rate gyro integration during static conditions and dynamic trigger points. The post-transient bias estimate and pitch attitude tracking plots are shown in Figures 4.10 and 4.11. The bias estimate converges to within ± 0.15 degrees per second within 10 seconds and is shown as Figure G.3 in Appendix G.

From the attitude and bias error plots, the filter appears to be performing correctly due to relative accuracy. To make sure the filter is operating properly the 1σ and 3σ values from the state covariance matrix were plotted against the error of the estimated state

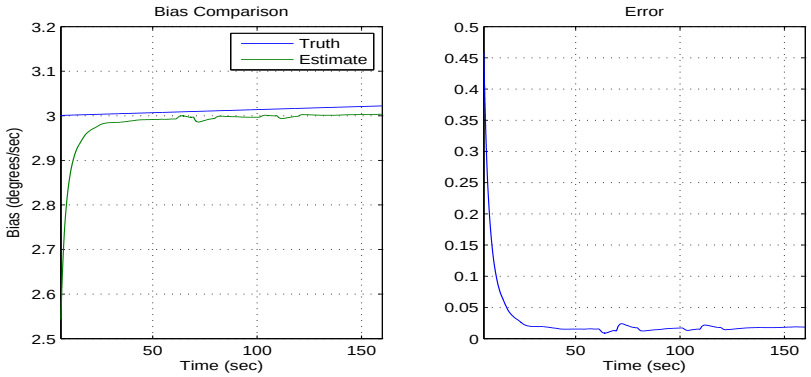

Figure 4.10: LDKF Bias Estimate - First Iteration of Parameters

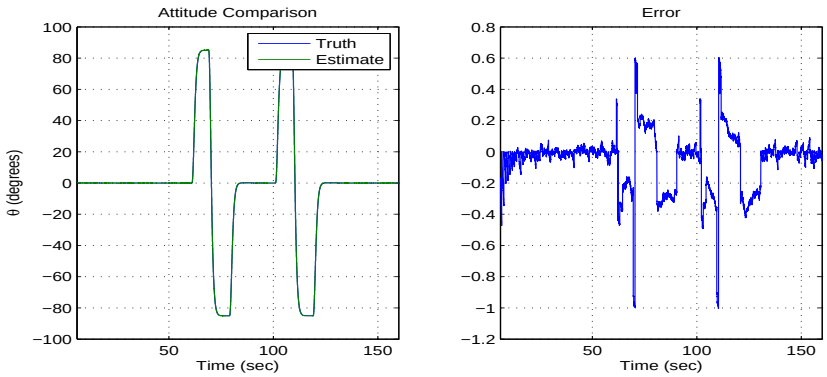

Figure 4.11: LDKF Attitude Estimate - First Iteration of Parameters

and the incoming accelerometer measurement. The results are plotted in Figure 4.12 with the attitude error divided by 1000 for scaling. For checking of proper bias estimation operation, the 1σ and 3σ bounds from the covariance matrix are compared to the difference of the bias estimate and the true bias and plotted in Figure 4.13, with the error divided by 1000 for scaling purposes. The true bias is used in this case for error calculation because there are no bias measurements available.

Figures 4.12 and 4.12 show the filter is not optimally operating due to continued excursions outside the 3σ bounds by the scaled attitude error and the scaled bias error outside the 3σ bounds. The scaled errors are outside the acceptable bounds for proper filter operation since the initial noise parameters assume the signal variances to be relatively small outside of the proposed model. The initial state covariance estimates do possess a small effect on the operation of the filter but as stated prior, the Kalman filter will converge even when badly initialized as long as the state model and variances are relatively accurate. A simulation was run with the same noise variances as the first iteration but

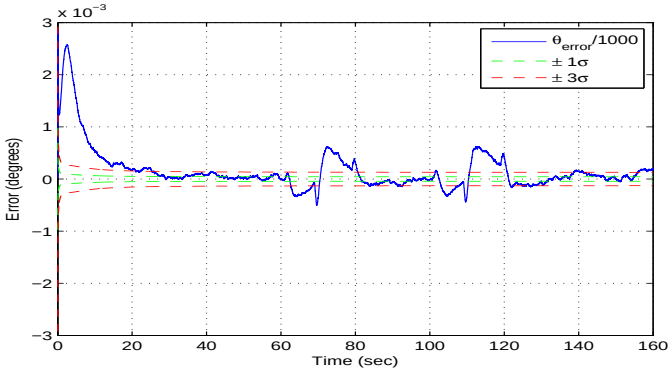

Figure 4.12: Attitude Error and Covariance - First Iteration of Parameters

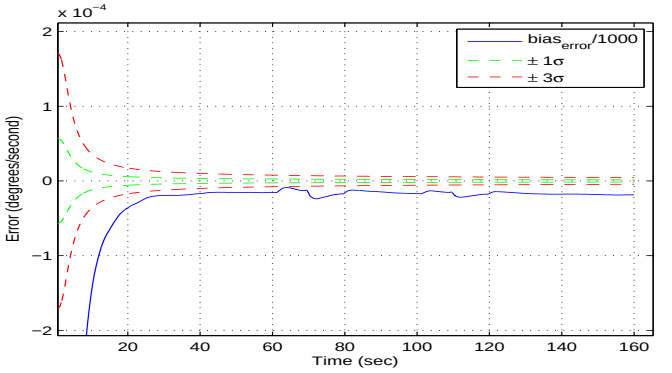

Figure 4.13: Bias Error and Covariance - First Iteration of Parameters

with the state covariance matrix initialized with diagonal elements of 9×10^9 to represent infinity. The estimate errors were reduced but the state errors were still well outside the covariance matrix bounds, these plots are given as Figures G.4 and G.5 in Appendix G.

The filter performs well as shown in Figures 4.10 and 4.11 but it is desirable to reduce the steady state bias error and the attitude error during dynamic maneuvers. The initial state estimate should remain the same but the noise variances should be tuned for improved convergence of the rate gyro bias and tracking of the pitch attitude. The noise variances were tuned according to the sensitivity analysis presented in Section 2.3.3. The variances were altered to reflect more trust in the accelerometer measurements due to the averaging of several unsaturated accelerometers and less trust in rate gyro precision. Due to variance tweaking, the state covariance matrix was increased to allow for higher uncertainty in the initial state values.

The state covariance matrix was altered with diagonal elements changed to 1×10^{-3}

while the off-diagonal elements were kept as zeros. The measurement noise standard deviation, σ_A, was decreased to reflect a more accurate measurement of pitch attitude based on the fusion of unsaturated accelerometer signals. The rate gyro bias process noise standard deviation, σ_B, was increased, $1 \times 10^{-8}\text{rad/sec}^{3/2}$, to account for a larger bias variance and the presence of a time varying bias. The standard deviation of process noise associated with the rate gyro pitch estimate, σ_G, was increased, $1 \times 10^{-6}\text{rad/sec}^{1/2}$, for consideration of additional gyro inaccuracies due to higher levels of signal noise. The standard deviation values for the process and measurement noise result from examining the impact of σ_A with other variances held constant, then holding σ_A constant while the other parameters were changed at the same time or one was changed while the other was constant. Figures 4.14 and 4.15 display the results of the tuning with Table 4.1 comparing the results of the initial Kalman Filter and tuned Kalman Filter with respect to the integral of the square of the bias error as well as the attitude error from start-up transient end to the simulation end. The integral of the errors for Quaternion Back-Differencing Algorithm is listed for comparison.

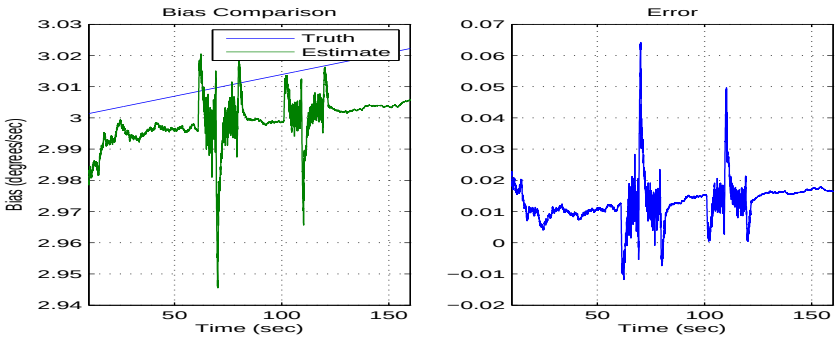

Figure 4.14: LDKF Bias Estimate - Second Iteration of Parameters

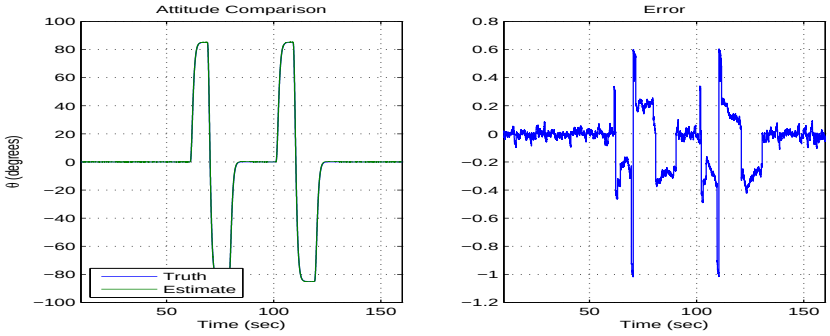

Figure 4.15: LDKF Theta Estimate - Second Iteration of Parameters

From Figures 4.14 and 4.15, tuning of the Kalman Filter in accordance with the sensitivity analysis and assumptions resulted in a more robust bias estimator and attitude observer and performs better than the Quaternion Back-Differencing algorithm which was relatively accurate. Additionally, plots of the bias estimates from both the Kalman Filter and Quaternion Back-Differencing are provided for comparison with the $\pm 1\sigma$ and $\pm 3\sigma$ bounds on the rate gyro. The rate gyro variance was set to 0.15 $(\text{deg/sec})^2$, yielding $\sigma = 0.3873\text{deg/sec}$. Figures 4.16 and 4.17 illustrate how the Kalman Filter is more accurate and more well behaved throughout the simulation by comparison of the bias error with the rate gyro signal variance bounds.

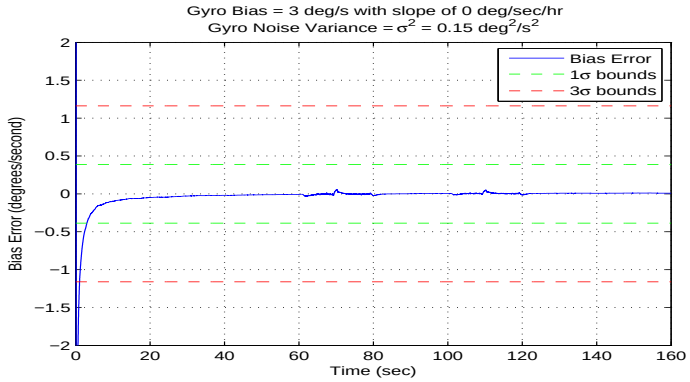

Figure 4.16: LDKF Second Iteration Bias Estimate with Gyro Deviation Bounds

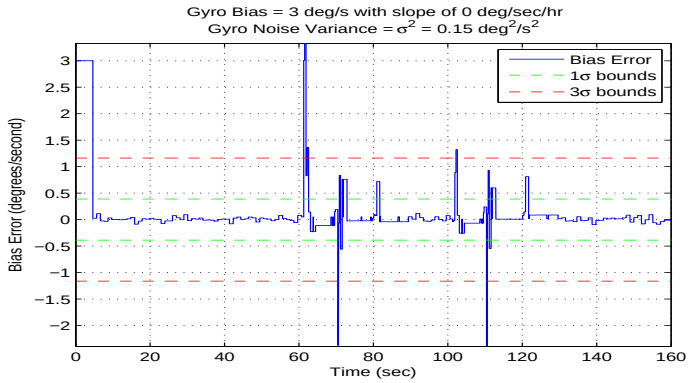

Figure 4.17: Quaternion Bias Estimate with Gyro Deviation Bounds

The Kalman Filter does not deviate outside the rate gyro bias 1σ bound after initial convergence whereas the Quaternion Back-Differencing algorithm exceeds the 3σ bounds in the middle of the doublet maneuver. Staying inside these bounds is key because 99.7% of a normally distributed random number lies within the $\pm 3\sigma$ bounds and 68.3% of a

normally distributed random number lies within the $\pm 1\sigma$ bounds [20]. Thus, both bias estimation algorithms are acceptable but the Kalman filter yields more accurate and desirable results.

Parameter	1st Iteration KF	2nd Iteration KF
P_0	$\begin{bmatrix} 1\times10^{-4} & 0 \\ 0 & 1\times10^{-12} \end{bmatrix}$	$\begin{bmatrix} 1\times10^{-3} & 0 \\ 0 & 1\times10^{-3} \end{bmatrix}$
σ_A (rad)	17×10^{-6}	1×10^{-7}
σ_B $\left(\text{rad/sec}^{3/2}\right)$	$\sqrt{10}\times10^{-10}$	1×10^{-8}
σ_G $\left(\text{rad/sec}^{1/2}\right)$	$\sqrt{10}\times10^{-7}$	1×10^{-6}
$\int_6^{160}\left(bias_{truth}-bias_{est}\right)^2\,\text{dt}$ $\left(\text{deg}^2/\text{sec}\right)$	0.40808	0.1484
$\int_6^{160}\left(\theta_{truth}-\theta_{est}\right)^2\,\text{dt}$ $\left(\text{deg}^2*\text{sec}\right)$	6.1688	5.7822
Maximum $\lvert\theta_{error}\rvert_{t=6}^{t=160}$ (deg)	1.0040	1.0178
Maximum $\lvert\text{bias}_{error}\rvert_{t=6}^{t=160}$ (deg/sec)	0.4598	0.1569
Quaternion Back-Differencing		
$\int_6^{160}\left(bias_{truth}-bias_{est}\right)^2\,\text{dt}$ $\left(\text{deg}^2/\text{sec}\right)$	13.7324	
$\int_6^{160}\left(\theta_{truth}-\theta_{est}\right)^2\,\text{dt}$ $\left(\text{deg}^2*\text{sec}\right)$	9.4908	
Maximum $\lvert\theta_{error}\rvert_{t=6}^{t=160}$ (deg)	1.1433	
Maximum $\lvert\text{bias}_{error}\rvert_{t=6}^{t=160}$ (deg/sec)	3.3285	

Table 4.1: LDKF Parameter Changes & Error for Double Pitch Doublet

Using the second iteration of LDKF parameters, the rate gyro bias magnitude was varied between zero and ten degrees/second with the slope varied between 0 and 1 degree/second/hour, to examine the LDKF post-transient sensitivity to the rate gyro bias magnitude and slope change. The integral of the squared error results are listed in Table 4.2, showing the bias magnitude has little effect on the bias estimate and a negligible effect on the attitude estimate. The gyro bias magnitude only affects the bias error integral at the 1×10^{-9} decimal place which shows why the errors appear equal to the fifth decimal place in the last column.

Impact of Changing Slope with Same Bias Magnitude			
Gyro Bias (deg/sec)	Gyro Bias Slope (deg/sec/hr)	$\int_6^{160} (\theta_{error})^2 \, dt$ (deg^2*sec)	$\int_6^{160} (b_{error})^2 \, dt$ (deg^2/sec)
0	0.0	5.7266	0.15326
	0.5	5.8723	0.14839
	1.0	6.0833	0.15401
1	0.0	5.6192	0.15326
	0.5	5.7654	0.14839
	1.0	5.9768	0.15401
3	0.0	5.6362	0.15326
	0.5	5.7822	0.14839
	1.0	5.9935	0.15401
5	0.0	5.6218	0.15326
	0.5	5.7680	0.14839
	1.0	5.9794	0.15401
10	0.0	5.7322	0.15326
	0.5	5.8771	0.14839
	1.0	6.0854	0.15401
Impact of Changing Bias Magnitude with Same Slope			
Gyro Bias Slope (deg/sec/hr)	Gyro Bias (deg/sec)	$\int_6^{160} (\theta_{error})^2 \, dt$ (deg^2*sec)	$\int_6^{160} (b_{error})^2 \, dt$ (deg^2/sec)
0.0	0	5.7266	0.15326
	1	5.6192	0.15326
	3	5.6362	0.15326
	5	5.6218	0.15326
	10	5.7322	0.15326
0.5	0	5.8723	0.14839
	1	5.7654	0.14839
	3	5.7822	0.14839
	5	5.7680	0.14839
	10	5.8771	0.14839
1.0	0	6.0833	0.15401
	1	5.9768	0.15401
	3	5.9935	0.15401
	5	5.9794	0.15401
	10	6.0854	0.15401

Table 4.2: Sensitivity of Kalman Filter to Rate Gyro Bias Magnitude and Slope

The second iteration of the LDKF was implemented in the sinusoid and step-and-hold maneuvers to illustrate filter tuning is independent of maneuver type. The filter is required to be tuned when the linearity of the plant model is altered or additional variances are observed in the system, such as additional sensor noise or small oscillations of the vehicle about it trim attitude while still remaining in a static environment. Figures 4.18 and 4.19 display the attitude and bias tracking error during the simulations. The convergence transient was approximately 10 seconds for the sinusoid maneuver since it began immediately at zero seconds while the Step-and-Hold maneuver transient remained 5 seconds. Table 4.3 compares the post-transient attitude error square and post-transient bias error square for the second iteration of the Kalman Filter with the Quaternion Back-Differencing algorithm. The bias error bound plots for both maneuvers for the Kalman Filter and Quaternion Back-Differencing are given in Appendix G as Figures G.6 and G.7.

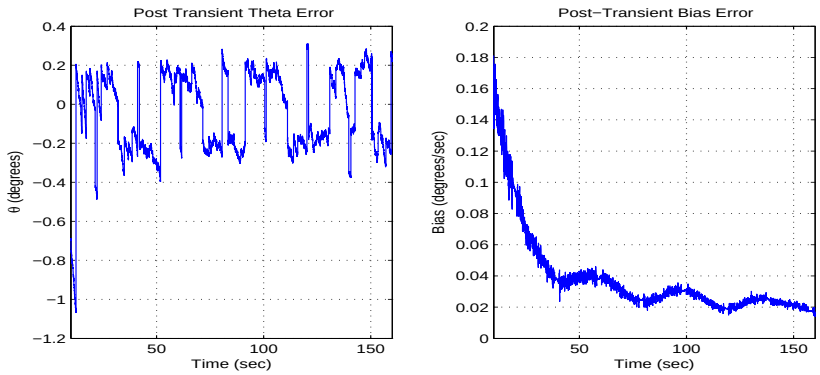

Figure 4.18: Second Iteration LDKF - Linear Sinusoid Maneuver

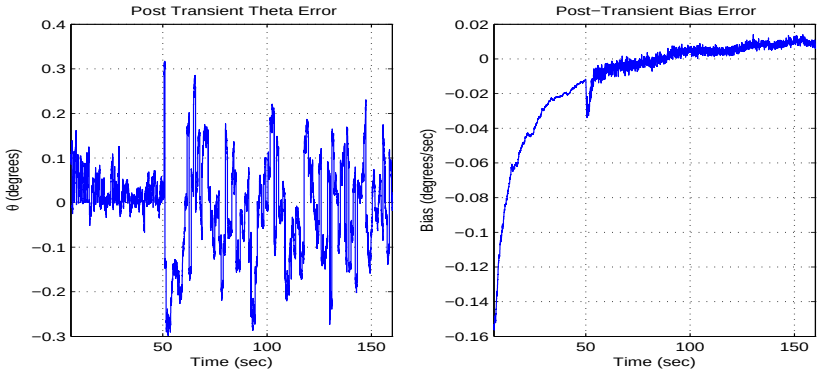

Figure 4.19: Second Iteration LDKF - Linear Step-and-Hold Maneuver

Maneuver	Error	2nd Iteration KF	Quaternion Back-Difference
Sinusoid	$\int_{10}^{160} (\theta_{error})^2 \, dt$ $\left(\text{deg}^2\text{*sec}\right)$	7.2204	10.505
	$\int_{10}^{160} (bias_{error})^2 \, dt$ $\left(\text{deg}^2/\text{sec}\right)$	0.329	9.3201
Step-and-Hold	$\int_{6}^{160} (\theta_{error})^2 \, dt$ $\left(\text{deg}^2\text{*sec}\right)$	1.6831	3.8766
	$\int_{6}^{160} (bias_{error})^2 \, dt$ $\left(\text{deg}^2/\text{sec}\right)$	0.14318	9.2558

Table 4.3: Algorithm Error Comparison of other Linear Maneuvers

4.3 Nonlinear Aircraft Model - Phase I

4.3.1 Utilized Model

The nonlinear six degree of freedom aircraft model developed using Section 3.1.2 and Appendix F is used to assess the performance of the observer in a simulated real world environment. Longitudinal motion was performed using elevator step inputs into a linear actuator model. The implementation of the device was performed over two phases to more quickly resolve issues arising from the nonlinear model and then imposed inertial loading. Phase 1 consisted of using the nonlinear plant to produce nonlinear attitude and pitch rate with gravity being the only applied translational load to the accelerometers. The resulting accelerometer measurements were then calculated using Equation 3.11 derived in Section 3.2.2 again shown in Equation 4.1. The equation is identical to the one used for simulating the accelerometer measurements for the linear plant model but using nonlinear inputs of pitch and pitch rate. The simulated accelerometer measurements for the simulation are shown in Figure E.5 in Appendix E. The simulations contained the identical sensor noise, bias, and bias slope as the linear plant model simulation.

$$gA_{z,i} = g\cos\left(\theta_{Maneuver} + \theta_i\right) - r_d q^2 \tag{4.1}$$

4.3.2 Back-Differencing Bias Estimation

The back-differencing algorithm using quaternions and gyro reinitialization was implemented in the nonlinear aircraft model serving as a baseline for observer performance. The maneuver performed was an elevator Step-and-Hold input producing an initial 87 degree pitch up maneuver at 60 seconds and allowing the aircraft to oscillate for the simulation. The simulation was performed over a 200 second interval with a time history

of aircraft trim conditions provided in Appendix F for comparison. The simulation signal contamination parameters consisted of a constant rate gyro bias of 3 degrees/second with accelerometer and rate gyro sensor noise. Figures 4.21 and 4.20 display the Quaternion Back-Differencing, Q.B.D, observer results for an attitude estimate and a bias estimate.

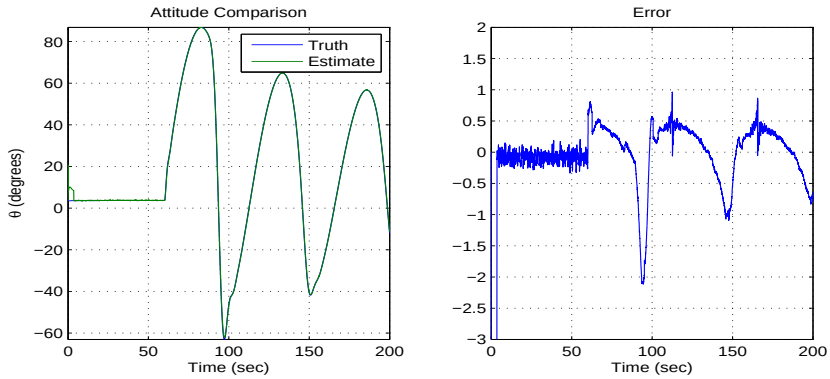

Figure 4.20: Nonlinear Model with Q.B.D Attitude Results

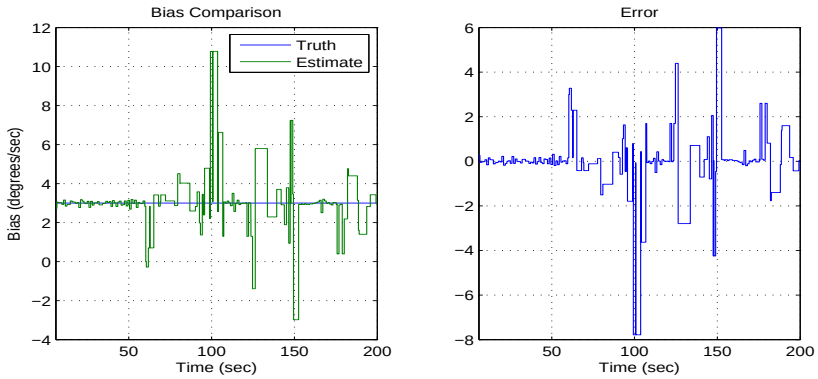

Figure 4.21: Nonlinear Model with Q.B.D. Bias Results

Figure 4.20 shows the attitude tracking error exceeds ±1 degree accuracy during the first pitch down maneuver then stays within the ±1 bounds on the subsequent oscillations. However, Figure 4.21 shows a maximum bias error of 8 degrees/second with the bias error mainly within the ±2 degrees/second regime. The maximum bias error is unacceptable due to extreme violations of the 1σ and 3σ bounds of ± 0.387degrees/second and $\pm$ 1.161degrees/second imposed from the assigned rate gyro noise variance. The plot of the observer bias estimate with the imposed bounds is given in Figure 4.22.

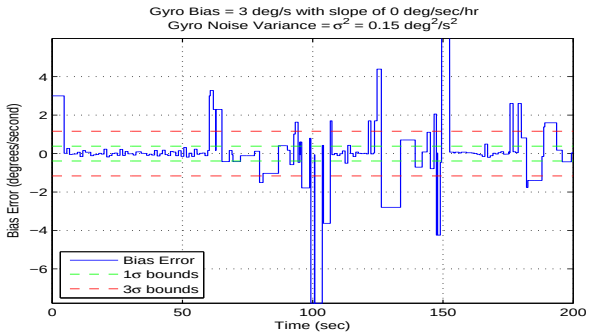

Figure 4.22: Nonlinear Model Quaternion Bias Error with Bounds

Figure 4.22 displays the static bias estimate possessing acceptable accuracy while dynamic bias estimation is highly inaccurate. The inaccuracy of the algorithm results from accelerometer measurement noise causing missed triggers and the 7.5 degree resolution of the accelerometer array. Therefore, the Kalman Filter tuned from previous linear simulations would be a good candidate for increasing dynamic accuracy of the observer since the estimate considers the previous estimate compared to a system model estimate and a measured estimate.

4.3.3 Kalman Filter Bias Estimation

The linear discrete Kalman Filter derived in Section 2.3.3 with the tuned parameters arrived at in Section 4.2 was implemented as an observer to the nonlinear aircraft model to improve rate gyro bias estimation and attitude tracking. A comparison of the true attitude and rate gyro bias with the observer estimate utilizing the linear discrete Kalman Filter with the second iteration of parameters from Section 4.2.3 is shown in Figures 4.23 and 4.24.

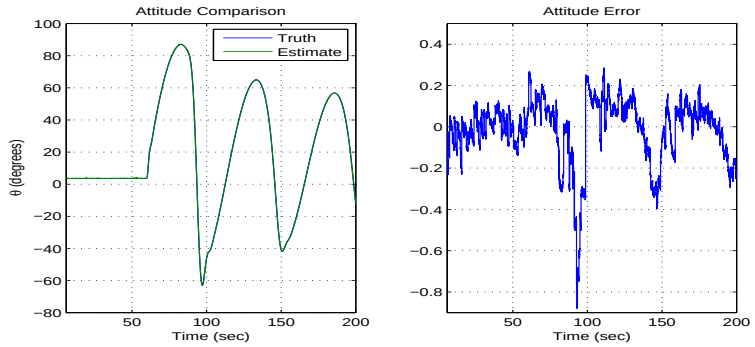

Figure 4.23: Nonlinear Attitude Results - Second LDKF Iteration

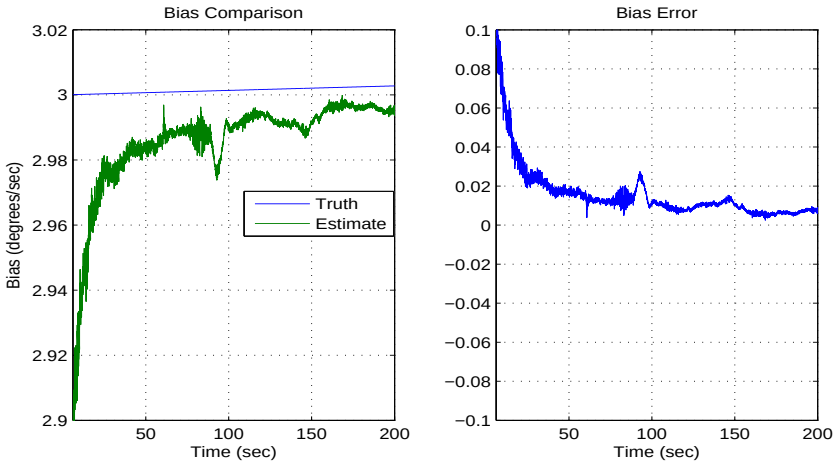

Figure 4.24: Nonlinear Bias Results - Second LDKF Iteration

For the Phase I Nonlinear Simulation, the bias estimate is reasonable and the attitude estimate does not drift outside an acceptable range of ±1 degree based on the accuracy of other instruments from [6] and [31]. Table 4.4 lists the results of the Nonlinear Phase 1 simulation with integrals of the squared error for the attitude and bias estimates.

Parameter	2nd Iteration LDKF
P_0	$\begin{bmatrix} 1\times10^{-3} & 0 \\ 0 & 1\times10^{-3} \end{bmatrix}$
σ_A (rad)	1×10^{-7}
σ_B (rad/sec$^{3/2}$)	1×10^{-8}
σ_G (rad/sec$^{1/2}$)	1×10^{-6}
$\int_6^{200}(bias_{truth}-bias_{est})^2\,\mathrm{dt}$ $(\mathrm{deg}^2/\mathrm{sec})$	0.090287
$\int_6^{200}(\theta_{truth}-\theta_{est})^2\,\mathrm{dt}$ $(\mathrm{deg}^2*\mathrm{sec})$	4.8622
Maximum Absolute θ_{error} (deg)	0.87915
Maximum Absolute bias_{error} (deg/sec)	0.12916

Table 4.4: LDKF Parameters and Simulation Results

Due to the nonlinear nature of the simulation plant model, the second iteration of LDKF parameters were checked ensuring proper operation by comparing the attitude and bias errors to the $\pm1\sigma$ and $\pm3\sigma$ values from the diagonal elements of the filter's covariance

matrix, P.

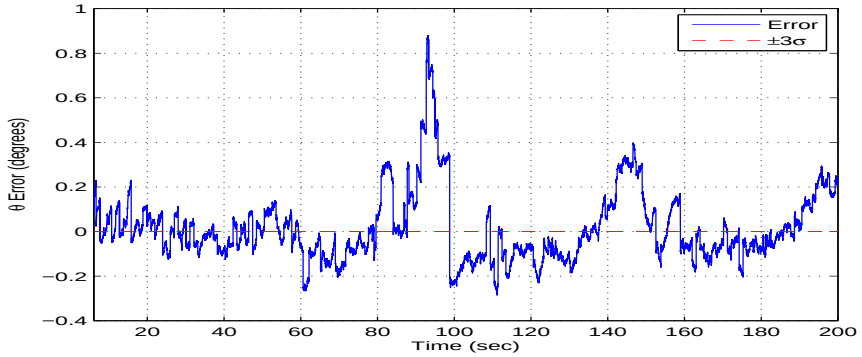

Figure 4.25: Nonlinear Attitude Error Covariance Check - Second LDKF

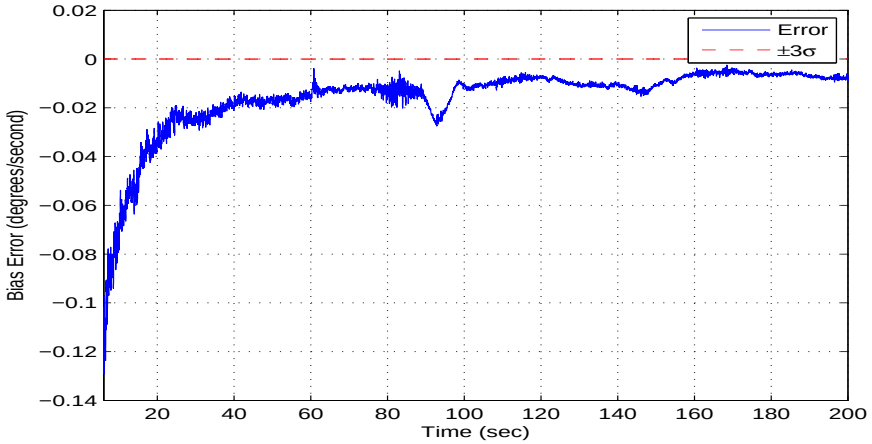

Figure 4.26: Nonlinear Bias Error Covariance Check - Second LDKF

Figures 4.25 and 4.26 show the filter's noise variances and initial state covariance estimate are constrictive for the corrupted nonlinear input signals to the filter because of the constant deviation outside of the $\pm 3\sigma$ bounds. A third iteration of filter tuning was formulated per the second iteration by increasing the measurement variances in the static and dynamic domains, increasing the bias process noise, and introducing dynamic and static gyro process noise variances. The initial state estimates remained the same while the initial state covariance matrix was given diagonal elements of 9×10^9 to allow the filter to converge on the proper covariance matrix. The bias process noise variance has the same value over both static and dynamic operating environments because its values are independent of the operating environments unlike the accelerometer measurements and rate gyro. The simulation results of the second and third Kalman Filter iterations

are given in Table 4.5. The third iteration has lower bias and attitude error-squared integrals and possesses lower maximum error deviations than the second iteration.

Parameter		LDKF 2nd Iteration	LDKF 3rd Iteration
P_0		$\begin{bmatrix} 1\times10^{-3} & 0 \\ 0 & 1\times10^{-3} \end{bmatrix}$	$\begin{bmatrix} 9\times10^{9} & 0 \\ 0 & 9\times10^{9} \end{bmatrix}$
σ_A(rad)	Static	1×10^{-5}	1×10^{-2}
	Dynamic	1×10^{-5}	1×10^{-1}
$\sigma_B(\text{rad/sec}^{3/2})$		1×10^{-8}	1×10^{-5}
$\sigma_G(\text{rad/sec}^{1/2})$	Static	1×10^{-6}	1×10^{-3}
	Dynamic		1×10^{-2}
$\int_6^{200}(bias_{truth}-bias_{est})^2\,\text{dt}$ $\left(\text{deg}^2/\text{sec}\right)$		0.090287	0.013413
$\int_6^{200}(\theta_{truth}-\theta_{est})^2\,\text{dt}$ $\left(\text{deg}^2*\text{sec}\right)$		4.8622	3.8448
Maximum Absolute θ_{error} (deg)		0.87915	0.66468
Maximum Absolute bias_{error} (deg/sec)		0.12916	0.093477

Table 4.5: Nonlinear Plant Second and Third LDKF Comparison

Figures 4.27 and 4.28 demonstrate the third iteration of linear discrete Kalman filter parameters yields a properly operating filter due to error versus variance comparison. In addition, by tuning the parameters to yield a properly operating filter, the calculated squared error integrals and maximum absolute error deviations have decreased considerably in comparison to their magnitude.

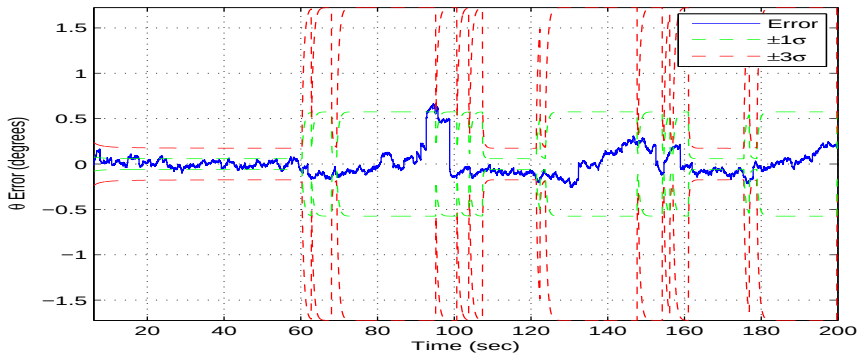

Figure 4.27: Nonlinear Attitude Error Covariance Check - Third LDKF

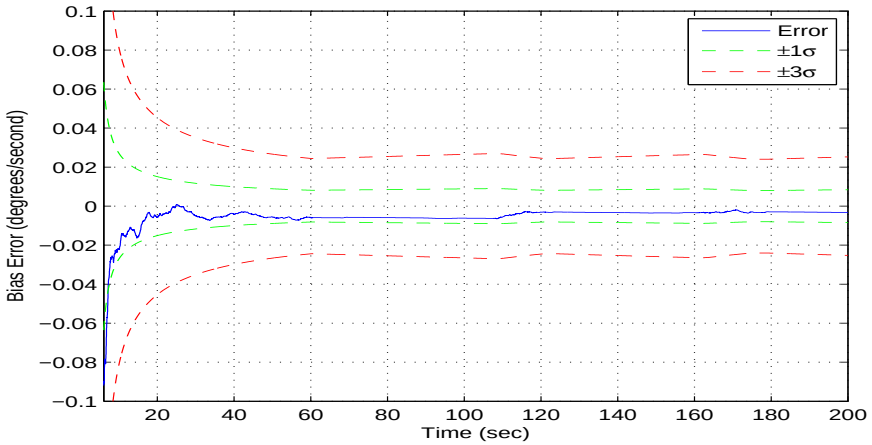

Figure 4.28: Nonlinear Bias Error Covariance Check - Third LDKF

4.4 Nonlinear Aircraft Model - Phase II

4.4.1 Utilized Model

A full nonlinear simulation of the device is performed in this section using the nonlinear model developed in the previous section and using Equations 3.9 and 3.6 from Section 3.2.2. The imposed translational acceleration loads are calculated from the forces experienced by the aircraft in flight given by Equations F.10 and F.11 in Appendix F.

$$\begin{aligned} gA_{z,i} &= (A_{X,imp} - g\sin\theta_{Man})\sin\theta_i + (A_{Z,Imp} + g\cos\theta_{Man}\cos\phi_{Man})\cos\theta_i - r_d q^2 \\ &= A_{X,CG}\sin\theta_i + A_{Z,CG}\cos\theta_i - r_d q^2 \end{aligned} \quad (4.2)$$

Implementation of Equation 4.2 for simulation of accelerometer measurements results in accelerometer measurements mimicking those of the linear plant model and nonlinear

plant model Phase I for static conditions but radically different measurements during dynamic operation as shown by comparing Figure 4.29 with those in Appendix Section E.3. The reason for the discrepancy is consideration of the imposed translational loads along the vehicle's primary and tertiary axes resulting from vehicle thrust and aerodynamic forces during dynamic maneuvers. In static conditions, the lift force of the vehicle negates the weight of the vehicle along with the vehicle thrust negating the vehicle drag. However, during abrupt maneuvers or maneuvers where quasi-static equilibrium cannot be assumed, the forces become unbalanced resulting in non-constant accelerations and accelerations radically more or less than 1 gee of acceleration are shown in Figure 4.29.

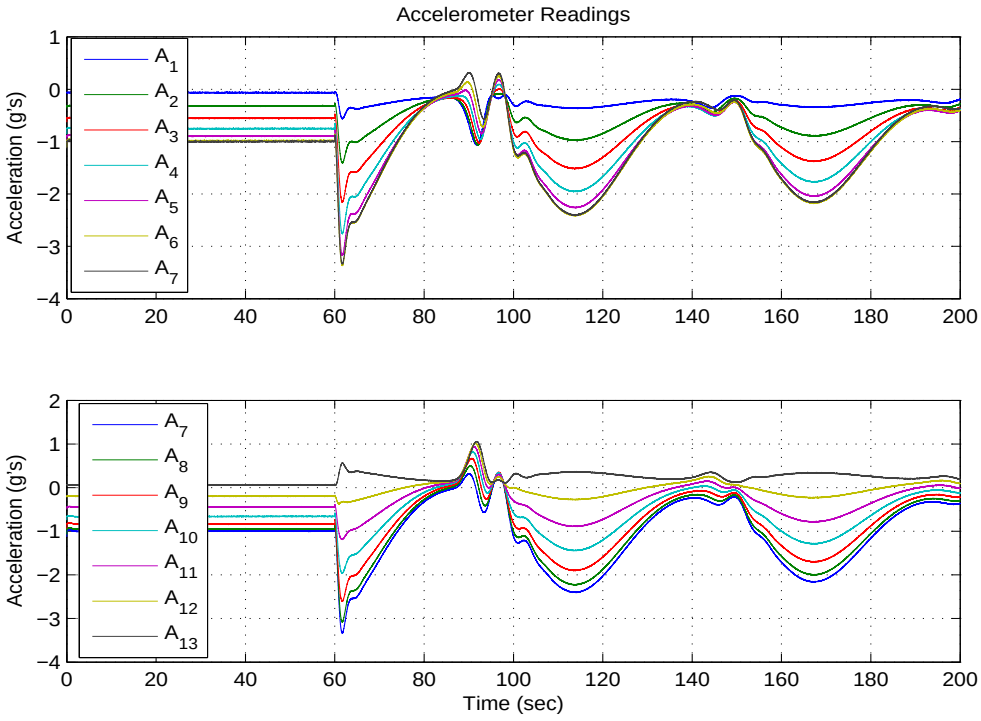

Figure 4.29: Accel Measurements - Nonlinear Model Full Loading

For attitude estimation in full longitudinal loading, two additional accelerometers are required at the vehicle center of gravity for measuring the translational accelerations along the vehicle's primary and tertiary axes. Augmenting the accelerometer array with two additional accelerometers is required as shown in Equation 3.6 where the sum of the imposed inertial loads and weight of the aircraft is sensed by accelerometers. With knowledge of these values, the vehicle attitude can be estimated using the accelerometer array measurements and Equation 4.2.

Algorithm for Imposed Load Calculations and Attitude Estimate

For this work, the vehicle is assumed to maneuver in the longitudinal plane only allowing for Equation 4.2 to be reduced to Equation 4.3 since the maneuver yaw angle is zero. Equation 4.3 displays the contributions for each translational and rotational acceleration component with the translational components dependent on the accelerometers offset angle from the vehicle's tertiary axis and the rotational component dependent on the accelerometers offset radius from the vehicle's center of gravity.

$$gA_{z,i} = \underbrace{A_{X,CG}\sin\theta_i}_{\text{X Acceleration Component}} + \underbrace{A_{Z,CG}\cos\theta_i}_{\text{Z Acceleration Component}} - \underbrace{r_d q^2}_{\text{Rotational Acceleration Component}} \tag{4.3}$$

From Equation 3.6 the accelerometers located at the center of gravity of the vehicle register the sum of the imposed motion and gravitational accelerations. The total acceleration, in gees, along the primary axis, $A_{X,CG}$, and tertiary axis, $A_{Z,CG}$, are shown in Equations 4.4 and 4.5 respectively.

$$A_{X,CG} = \frac{A_{X,Imp}}{g} - \sin\theta_{Man} \tag{4.4}$$

$$A_{Z,CG} = \frac{A_{Z,Imp}}{g} + \cos\theta_{Man} \tag{4.5}$$

The imposed translational and rotational acceleration loading due to vehicle maneuvers is not directly measured and must be estimated using measurements from the accelerometer array and the accelerometers mounted at the vehicle's center of gravity. When the imposed loadings are calculated, a vehicle orientation attitude can be calculated using the trigonometric relationships given in Equations 4.4 and 4.5.

The acceleration due to rotation motion in gees, $r_d q^2/g$, can be solved for by using the reading of Accelerometer 7, located along the tertiary axis a distance, r_d, away from the center of gravity, and the accelerometer measuring acceleration along the vehicle's tertiary axis at the center of gravity, $A_{Z,CG}$. The sensed acceleration of Accelerometer 7 is not affected by acceleration along the vehicle's primary axis due to the orientation of the accelerometer along the vehicle's tertiary axis. This leads to the primary axis sensed acceleration tending towards zero and the tertiary axis sensed acceleration to be equal to that registered at the center of gravity with the rotation acceleration term remaining present. Equation 4.3 can be simplified and solved for the rotational acceleration component in gees experienced by all accelerometers with radius r_d shown in Equation 4.6.

$$\frac{r_d q^2}{g} = A_{Z,CG} - A_{z,7} \tag{4.6}$$

Substituting Equations 4.5 and 4.6 into Equation 4.2 allows for a solution of the imposed tertiary axis acceleration loading. Accelerometers 2 through 12 are used to avoid a divide

by zero singularity due to the location of Accelerometers 1 and 13. The attitude estimate produced by the observer is a continuous signal, thus the previous estimated pitch angle, $\theta_{Man,Prev}$, is known and is used to produce an estimate of the present imposed translational acceleration. The result is valid because the vehicle attitude deviates minimally over a small time interval and is empirically shown by Figure 4.30 where the maximum deviation of the true vehicle attitude deviates by a maximum magnitude of 0.27 degrees from one time step to the next for the evaluation maneuver. Since the algorithm relies on a delayed attitude estimate, Equations 4.7 and 4.8 are approximations.

$$\cos\theta_i \left(\frac{A_{Z,Imp}}{g}\right) \approx A_{z,i} - A_{X,CG}\sin\theta_i + A_{Z,CG} - A_{z,7} - \cos\theta_{Man,Prev}\cos\theta_i \tag{4.7}$$

$$\frac{A_{Z,Imp}}{g} \approx \frac{A_{z,i} - A_{X,CG}\sin\theta_i + A_{Z,CG} - A_{z,7} - \cos\theta_{Man,Prev}\cos\theta_i}{\cos\theta_i}\Big|_{For\ i\in[2,12]} \tag{4.8}$$

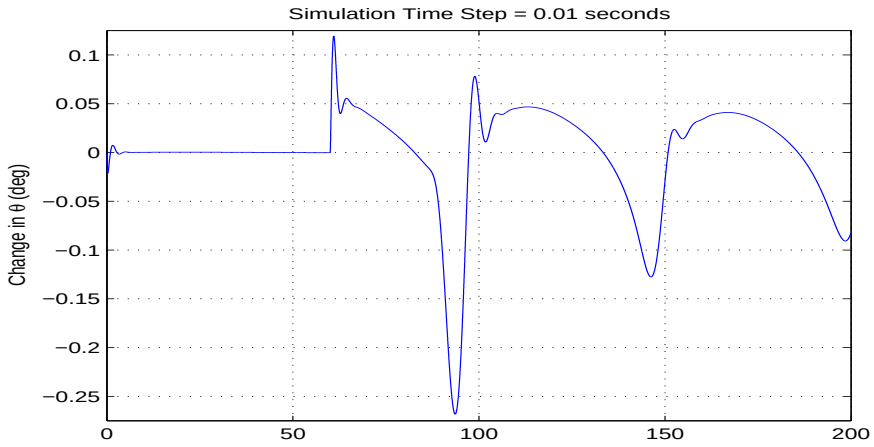

Figure 4.30: Longitudinal Attitude Change over Sequential Time Samples

Substituting Equations 4.4 and 4.6 into Equation 4.2 allows for a solution of the imposed primary axis acceleration loading. Accelerometers 1 through 6 and 8 through 13 are used to avoid a divide by zero singularity due to the location of Accelerometer 7. The previous estimated pitch angle is used under the same assumptions for the tertiary axis imposed loading solution. Reliance on a time delayed attitude estimate results in Equations 4.9 and 4.10 being approximations.

$$\sin\theta_i \left(\frac{A_{X,Imp}}{g}\right) \approx A_{z,i} - A_{Z,CG}\cos\theta_i + A_{Z,CG} - A_{z,7} + \sin\theta_{Man,Prev}\sin\theta_i \tag{4.9}$$

$$\frac{A_{X,Imp}}{g} \approx \frac{A_{z,i} - A_{Z,CG}\cos\theta_i + A_{Z,CG} - A_{z,7} + \sin\theta_{Man,Prev}\sin\theta_i}{\sin\theta_i}\Big|_{For\ i\in[1,6]\ and\ [8,13]} \tag{4.10}$$

With the imposed translational and rotational acceleration approximations an estimate for the present vehicle pitch attitude can be calculated using the tangent trigonometric function with Equations 4.4 and 4.5.

$$\theta_{Man,Present} \approx \arctan\left(\frac{-\left(A_{X,CG} - \frac{A_{X,Imp}}{g}\right)}{A_{Z,CG} - \frac{A_{Z,Imp}}{g}}\right) \tag{4.11}$$

The present attitude estimate is then used in conjunction with the present pitch rate from the gyro for estimation of the gyro bias. When the vehicle is static, the attitude estimate is used as the rate gyro integration initial condition and when the vehicle is dynamic the dynamic trigger estimate is used as the initial condition at discrete points. The dynamic triggers occur when the difference between two accelerometer measurements falls below the defined threshold as performed in previous simulations. However, the imposed loadings must be subtracted from the accelerometer signals to produce a pure rotation acceleration estimate before the differencing can be performed. Equation 4.2 is rearranged to subtract the calculated imposed translational acceleration loadings from the accelerometer readings leaving only the gravity and rotational components as shown in Equation 4.12.

$$A_{z,i} - \frac{A_{X,Imp}}{g}\sin\theta_i - \frac{A_{Z,Imp}}{g}\cos\theta_i = \cos\theta_{Man}\cos\theta_i - \sin\theta_{Man}\sin\theta_i - \frac{r_d q^2}{g} \tag{4.12}$$

The left hand side of Equation 4.12 is calculated using the accelerometer readings along with Equations 4.8 and 4.10, then used in the differencing of accelerometer measurements during dynamic operating conditions. Figure 4.31 displays the flow chart for algorithm operation in conjunction with the bias estimator. The initial estimate of the vehicle's attitude was set to zero for the simulation.

$$A_{z,i,Pure\ Rotation\ Approx} = A_{z,i} - \frac{A_{X,Imp}}{g}\sin\theta_i - \frac{A_{Z,Imp}}{g}\cos\theta_i \tag{4.13}$$

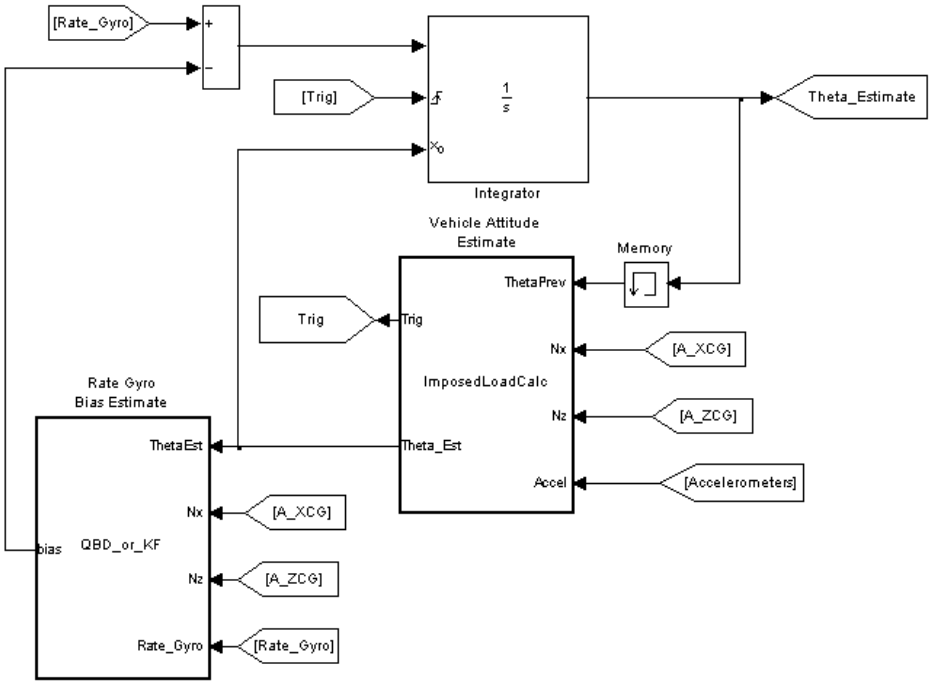

Figure 4.31: Flowchart of Full Loading Algorithm with Bias Estimation

4.4.2 Back-Differencing Bias Estimation

The quaternion back-differencing bias estimation in conjunction with the imposed loading estimation algorithm in Section 4.4.1 did not yield a desirable bias or attitude estimation result due to the radical fluctuation of the bias calculation as shown previously in Figure 4.21. Since the present attitude estimate is dependent on a relatively accurate previous attitude estimate, a large deviation in the calculated bias results in a large deviation from true attitude. As the vehicle remains in the dynamic regime, the bias error fluctuates radically leading to an imprecise attitude estimate that compounds as dynamic operation continues. Figures 4.32 and 4.33 show the Quaternion back-differencing algorithm can only be implemented with the imposed loading calculation algorithm during vehicle static conditions where the bias error is minimal resulting in a relatively accurate attitude estimate. The simulation was run for 200 seconds with the figures limited to 75 seconds showing how a large fluctuation in bias estimation in Figure 4.32 creates a larger deviation from attitude truth in Figure 4.33. From these results, a Kalman Filter must be implemented accounting for past state values of attitude and bias so the estimated attitude does not deviate significantly from the true vehicle attitude.

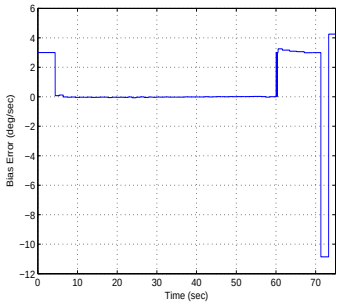

Figure 4.32: Bias Error for Q.B.D. in Nonlinear Model Phase II

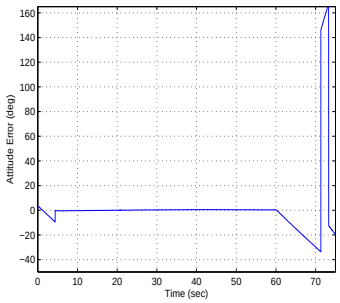

Figure 4.33: Attitude Error for Q.B.D. in Nonlinear Model Phase II

4.4.3 Kalman Filter Bias Estimation

The third iteration of the linear discrete Kalman filter from Section 4.3.3 was instituted with the imposed loading estimation algorithm derived in Section 4.4.1. Figures 4.34 and 4.35 display the attitude and bias estimation results for the implemented Kalman Filter.

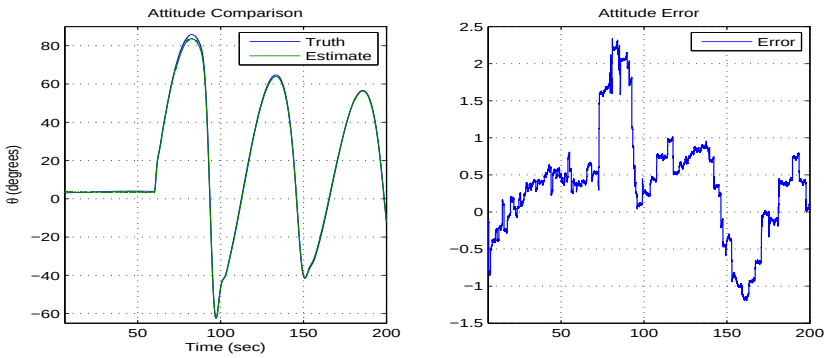

Figure 4.34: Attitude Results Third Iteration LDKF - Nonlinear Model Phase II

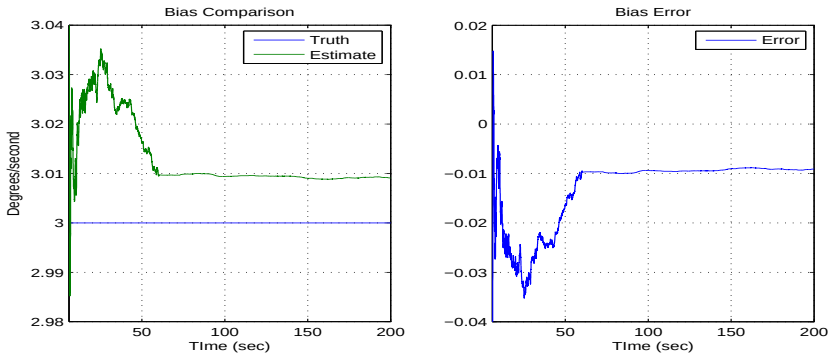

Figure 4.35: Bias Results Third Iteration LDKF - Nonlinear Model Phase II

Although the filter appears to operating appropriately, the attitude error is outside of the target ±1 degree attitude error regime. Figure 4.36 displays the filter is not operating within the imposed covariance bounds during static operation necessitating an additional iteration of Kalman Filter tuning. Figure G.8 in Appendix G displays the covariance analysis for the filter's bias error.

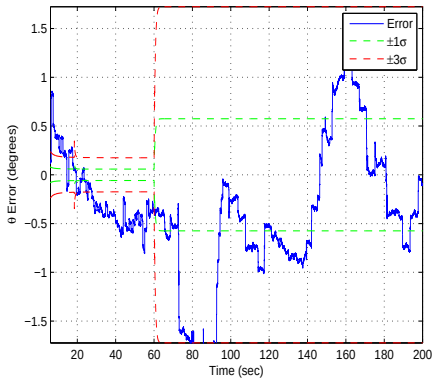

Figure 4.36: Third Iteration LDKF Attitude Covariance Analysis - Nonlinear Phase II

A fourth iteration of Kalman Filter tuning was performed for the steady state behavior of the filter's attitude error to lie within the imposed covariance bounds. The bias variance and initial covariance estimates were held constant while the static and dynamic noise variances for the rate gyro and accelerometers were increased by approximate factor of 10. Figures 4.37 and 4.38 display the attitude and bias estimation results respectively. The covariance analysis for the attitude and bias error is shown in Figure 4.39.

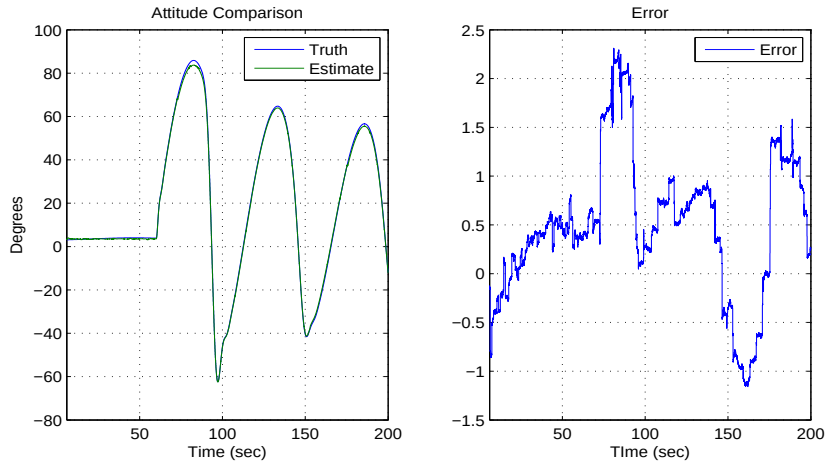

Figure 4.37: Attitude Results Fourth Iteration LDKF - Nonlinear Model Phase II

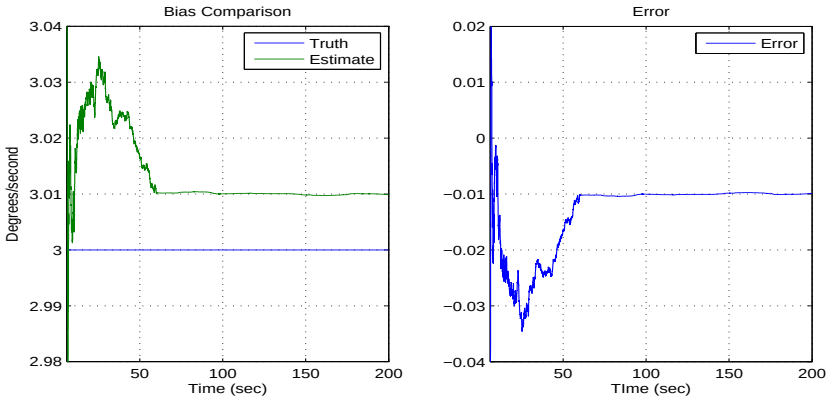

Figure 4.38: Bias Results Fourth Iteration LDKF - Nonlinear Model Phase II

For checking proper steady-state filter operation in real time, the attitude estimate residual calculated using Equations 2.78 and 2.79 was compared with the $\pm 1\sigma$ and $\pm 3\sigma$ values of the first diagonal element within the generated state covariance matrix during static operation. Figure 4.40 displays the steady-state operation of the fourth iteration of the LDKF and shows the filter is operating properly within the covariance bound constraints. The filter can only be check for proper operation with one state because the bias is not directly measurable. Table 4.6 compares the parameter differences and error results of both the third and fourth Kalman filter iterations. The fourth iteration has a higher integral square attitude error, but is properly operating within the imposed and possesses lower absolute error magnitudes.

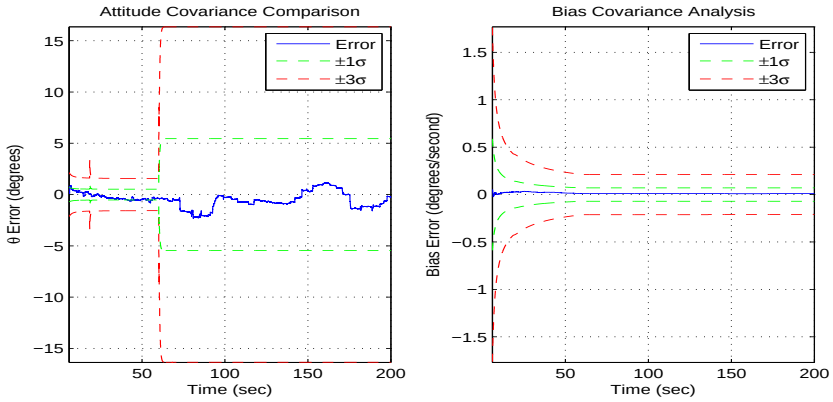

Figure 4.39: Fourth Iteration LDKF Covariance Analysis - Nonlinear Phase II

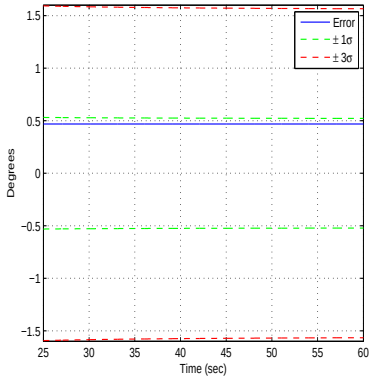

Figure 4.40: Fourth Iteration LDKF Residual Covariance Analysis

The results of the Kalman filter tuning iterations were found to possess an attitude accuracy of ±2.3 degrees at best which is outside the imposed accuracy bound of ±1degree. However, the imposed rate gyro and accelerometer noise standard deviations using in the simulations were found to be 13 and 19 times greater than the standard deviations of available low-cost rate gyro and accelerometers respectively [15].

Parameter		LDKF 3rd Iteration	LDKF 4th Iteration
P_0		$\begin{bmatrix} 9\times10^9 & 0 \\ 0 & 9\times10^9 \end{bmatrix}$	$\begin{bmatrix} 9\times10^9 & 0 \\ 0 & 9\times10^9 \end{bmatrix}$
σ_A(rad)	Static	1×10^{-2}	9×10^{-2}
	Dynamic	1×10^{-1}	9×10^{-1}
$\sigma_B(\text{rad/sec}^{3/2})$		1×10^{-5}	1×10^{-5}
$\sigma_G(\text{rad/sec}^{1/2})$	Static	1×10^{-3}	9×10^{-3}
	Dynamic	1×10^{-2}	1×10^{-1}
$\int_6^{200}(bias_{truth}-bias_{est})^2\,\text{dt}$ $\left(\text{deg}^2/\text{sec}\right)$		0.041597	0.041762
$\int_6^{200}(\theta_{truth}-\theta_{est})^2\,\text{dt}$ $\left(\text{deg}^2*\text{sec}\right)$		128.25	152.43
Maximum Absolute θ_{error} (deg)		2.3372	2.3106
Maximum Absolute bias_{error} (deg/sec)		0.066934	0.055016

Table 4.6: Nonlinear Phase II Third and Fourth LDKF Comparison

4.5 Algorithm Comparison with published Results

The published sensor noise standard deviations in [15] were instituted for the nonlinear model Phase II simulation with the fourth iteration of Kalman filter parameters. Table 4.7 compares the updated parameters, the rate gyro bias remained set at 3 degrees/second since the algorithm has already been shown in Section 4.2.3 to be indifferent to the magnitude of the sensor bias within a certain interval. The accelerometer biases from [15] were not instituted because during ground initialization of the algorithm, the accelerometer biases can be found directly since their locations are known with respect to the local gravity vector.

Parameter	Prior Simulation Value	Published Values
Accelerometer (gees)	$\sqrt{0.000015}$	$2 \times 10^{-3} \left(\mathrm{m/s^2}\right) * \frac{1}{9.81\left(\mathrm{m/s^2}\right)}$
Rate Gyro (deg/sec)	$\sqrt{0.15}$	0.03

Table 4.7: Comparison of Prior Noise Parameters with Published [15]

Using the above published values in the nonlinear plant model Phase II simulation with the fourth iteration of Kalman filter parameters yields the following attitude and bias results shown in Figures 4.41 and 4.42 respectively. Figure 4.43 displays the off-line covariance analysis of the attitude and bias errors, showing the filter is operating properly. Figure 4.44 displays the on-line covariance analysis for the attitude error showing the filter is in proper working order.

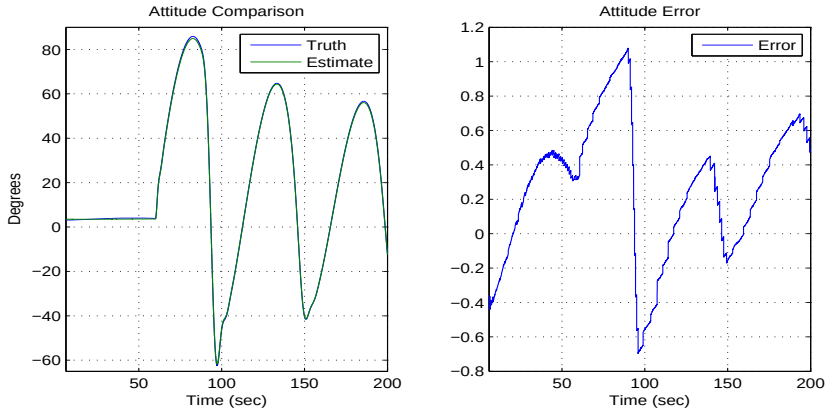

Figure 4.41: Attitude Results using Published Noise Parameters - Fourth LDKF

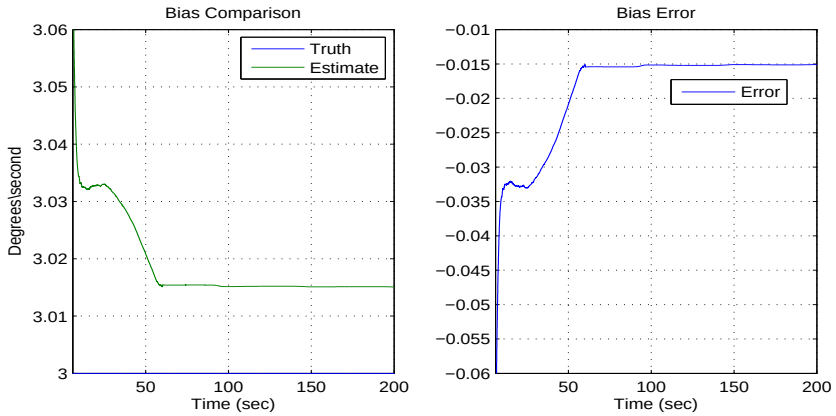

Figure 4.42: Bias Results using Published Noise Parameters - Fourth LDKF

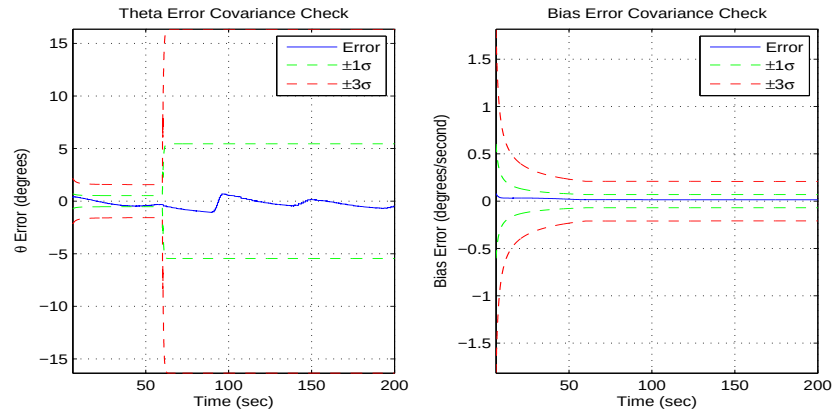

Figure 4.43: Covariance Results using Published Noise Parameters - Fourth LDKF

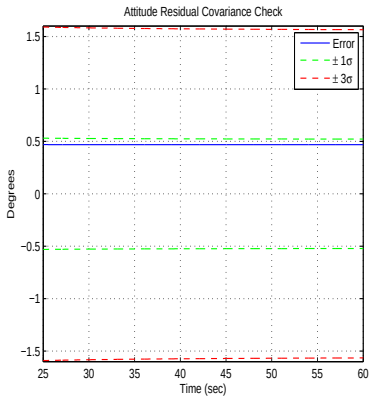

Figure 4.44: Residual Results using Published Noise Parameters - Fourth LDKF

From Figure 4.44, the filter is shown to converge during on-line steady-state operation. The implication of the on-line check is when the vehicle returns to static operation after dynamic maneuvers. The filter is able to detect a failed sensor if the filter does not converge back to inside the covariance bounds during steady-state operation. This adds an extra degree of robustness by allowing for alert of failed sensors.

The analysis plots of the third iteration of the Kalman filter are omitted since the fourth iteration has a slight edge in accuracy shown in Table 4.8 and the third iteration deviates outside the off-line covariance analysis bound. The omitted plots are included in Appendix G for completeness. The third iteration of the Kalman filter was considered since it performed similar to the fourth iteration in the previous simulation. Table 4.9 compares the standard deviations of the attitude and bias error between the published results and the algorithm proposed in this work.

Parameter		LDKF 3rd Iteration	LDKF 4th Iteration
P_0		$\begin{bmatrix} 9\times10^9 & 0 \\ 0 & 9\times10^9 \end{bmatrix}$	$\begin{bmatrix} 9\times10^9 & 0 \\ 0 & 9\times10^9 \end{bmatrix}$
σ_A(rad)	Static	1×10^{-2}	9×10^{-2}
	Dynamic	1×10^{-1}	9×10^{-1}
$\sigma_B(\text{rad/sec}^{3/2})$		1×10^{-5}	1×10^{-5}
$\sigma_G(\text{rad/sec}^{1/2})$	Static	1×10^{-3}	9×10^{-3}
	Dynamic	1×10^{-2}	1×10^{-1}
$\int_6^{200}(bias_{truth}-bias_{est})^2\,\text{dt}$ $\left(\text{deg}^2/\text{sec}\right)$		0.080532	0.080772
$\int_6^{200}(\theta_{truth}-\theta_{est})^2\,\text{dt}$ $\left(\text{deg}^2*\text{sec}\right)$		44.524	44.475
Maximum Absolute θ_{error} (deg)		1.097	1.0779
Maximum Absolute bias_{error} (deg/sec)		0.090691	0.082562

Table 4.8: Third and Fourth LDKF Comparison using Published Noise Parameters

The simulations conducted in this work and in [15] are different, however, the published results simulated a maximum pitch maneuver of 20 degrees and used relatively low pitch rates leading to negligible imposed translational loads. The derived algorithm in this work has already proved incredibly accurate over static operating conditions, near zero imposed loading, with bias and attitude estimation errors very close to zero as shown by the provided plots. Additionally, the proposed algorithm addresses accurate and robust dynamic attitude and bias estimation when subjected to extreme maneuvers imposed

Parameter	Kingston et al. 1σ value	Proposed Algorithm 1σ value
Pitch Attitude (degrees)	2.33	0.39567
Pitch Rate Bias (degrees/second)	0.84	0.0074945

Table 4.9: Error Standard Deviation Comparison

large acceleration loads such as the maneuver used for the nonlinear plant simulations. The algorithm proved to be robust and accurate in a large imposed loading environment and coupled with the algorithm performing near perfectly in static environments, it can be intuited that the algorithm will possess similarly if not better results when subjected a low imposed loading simulated environment.

Chapter 5

Conclusion and Future Work

5.1 Conclusion

In this work, the feasibility of an accelerometer-based device to estimate and eliminate a rate gyro bias in real-time for accurate longitudinal attitude estimation was assessed. This device and derived algorithm are a departure from conventional sensor parameter identification and attitude estimation since only the measurement of one inertial reference vector, gravity, is used. Formulation of such a device is beneficial because other inertial reference frame sensors, e.g. magnetometers, GPS, and inclinometers, are susceptible to environment induced errors, loss-of-signal, or possess slow-dynamics.

The developed algorithm expanded on previous research by fusing cost-effective accelerometers and a rate gyro with a two-state Kalman Filter for rate gyro bias estimation yielding accurate longitudinal attitude estimation. The accelerometer and rate gyro measurements were simulated using rotational displacement, rotation rate, and center-of-gravity acceleration outputs from a constructed nonlinear six degree-of-freedom aircraft model. Simulated flight conditions were composed of a quasi-stationary, static, condition and a dynamic condition with maneuvers resulting in imposed acceleration loads up to 3.5 gees. The sensor measurements were corrupted using white Gaussian noise along with a 3 degree per second rate gyro bias to simulate cost-effective sensors for unmanned vehicle applications. Using published cost-effective sensor variances, the algorithm produced a bias estimate error range of ± 0.09 degrees per second resulting in an attitude estimate error range of ± 1.08 degrees when subjected to the generated flight conditions and sensor signal corruption.

The end result is a feasible device utilizing a derived algorithm composed of simple mathematical operations requiring knowledge of sensor operation characteristics, found easily via hardware testing or data sheets, and the device location relative to the vehicle

center-of-gravity. These characteristics allow the proposed device to be cost-effective and easily implemented in a variety of unmanned applications, aerial, terrestrial, or marine.

5.2 Future Work

The research conducted in this work considered the feasibility of estimating a longitudinal rate sensor bias using an accelerometer array to yield reliable longitudinal aircraft attitude estimation during static and dynamic flight conditions. This work consisted of system modeling and signal simulation to evaluate device feasibility, but a test-platform consisting of a prototype device attached to a rotating mount secured to a translating platform is needed for a evaluation of the algorithm's operation under static and imposed loading conditions.

The next research phase is development of a rate bias and attitude estimation algorithm in the vehicle roll plane based off the completed longitudinal research utilizing the gravity vector. The test-bed developed for the longitudinal device can be adapted for evaluation of the roll device. After development of the roll algorithm, the roll and longitudinal algorithms must be fused to provide full, three-dimensional, vehicle attitude estimation utilizing measurement of the local gravity vector.

Upon development of an acceptable full attitude estimator, construction of the device as well as a ground test platform able to simulate translational motion in two dimensions and rotational motion in three dimensions should be carried out. Development of the test bed will aid in assessment of nuances that may arise prior to aircraft testing of the device's attitude and rate gyro bias estimation capability.

Bibliography

[1] M.A. Abid. Spacecraft Sensors. John Wiley and Sons, 2005.

[2] Y.I. Akcayir and Y. Ozkazanc. gyroscope drift estimation analysis in land navigation systems . In *Proceedings of IEEE Conference on Control Applications*. Institute of Electrical and Electronics Engineers, 2003.

[3] M.R. Akella, J.T. Halbert, and G.R. Kotamraju. rigid body attitude control with inclinometer and low-cost gyro measurements. *Systems and Control Letters*, 49:151–159, 2003.

[4] R.L. Allen and D.W. Mills. Signal Analysis - Time, Frequency, Scale, and Structure . John Wiley & Sons, 2004.

[5] H.G. Campbell. Matrices with Applications . Meredith Corporation, 1968.

[6] K.R. Cheatle. Fundamentals of Test Measurement Instrumentation . ISA, 2006.

[7] A.L. Crassidis and W.W. Walter. attitude estimation using an accelerometer and rate gyro based device . In *Proceedings at AIAA Atmospheric Flight Mechanics Conference and Exhibit*, August 2006.

[8] J.L. Crassidis and J.L. Junkins. Optimal Estimation of Dynamic Systems . Chapman & Hall/CRC, 2004.

[9] R.L. Farrenkopf. generalized results for precision attitude reference systems using gyros. *AIAA Paper 74-903*, 1974.

[10] R.L. Farrenkopf. analytic steady-state accuracy solutions for two common spacecraft attitude estimators. *Journal of Guidance, Navigation, and Control*, 1(4):282–284, 1978. Engineering Notes.

[11] B. Friedland. Control System Design: An Introduction to State-Space Methods . McGraw-Hill, 1986.

[12] W. Gao, Q. Nie, G. Zai, and H. Jia. gyroscope drift estimation in tightly-coupled ins/gps navigation system . In *Proceedings of IEEE Conference on Industrial Electronics and Applications*. Institute of Electrical and Electronics Engineers, 2007.

[13] A. Gelb. Applied Optimal Estimation. The Analytic Sciences Corporation, 1974.

[14] S.M. Herman and A.B. Poore. nonlinear least-squares estimation for sensor and navigation biases . In *Proceedings of SPIE Conference on Signal and Data Processing of Small Targets*. International Society for Optical Engineering, 2006.

[15] D. Kingston and R.W. Beard. real-time attitude and position estimation for small uavs using low-cost sensors. In *AIAA 3rd Unmanned Unlimited Technical Conference*, Chicago, Illinois, 2004. AIAA.

[16] J.B. Kuipers. Quaternions and Rotation Sequences: A Primer with Applications to Orbits, Aerospace, and Virtual Reality . Princeton University Press, 1999.

[17] E.J. Lefferts, F.L. Markley, and M.D. Shuster. kalman filtering for spacecraft attitude control . *Journal of Guidance and Control*, 5(5):417–429, 1982.

[18] The MathWorks Inc., http://www.mathworks.com/. Coordinate Systems for Modeling, 2008.

[19] N. Metni, J. Pflimlin, T. Hamel, and P. Soueres. attitude and gyro bias estimation for vtol uav . *Control Engineering Practice*, 14:1511–1520, 2006.

[20] D.C. Montgomery and G.C. Runger. Applied Statistics and Probability for Engineers . John Wiley & Sons, 1994.

[21] R.C. Nelson. Flight Stability and Automatic Control . McGraw-Hill, 1998.

[22] W.F. Phillips. Mechanics of Flight . John Wiley & Sons, 2004.

[23] W.F. Phillips, C.E. Hailey, and G.A. Gerbert. review of attitude representations used for aircraft kinematics. *Journal of Aircraft*, 38(4):718–737, 2001.

[24] J.G. Prokakis and D.G.Manolakis. Digital Signal Processing - Principles, Algorithms, and Applications . Pearson Prentice Hall, 4th edition, 2007.

[25] H. Rehbinder and X. Hu. nonlinear state estimation for rigid body motion with low-pass sensors . *Systems and Control Letters*, 40:183–190, 2000.

[26] H. Rehbinder and X. Hu. drift free attitude estimation for accelerated bodies . *Automatica*, 40:653–659, 2004.

[27] A.P. Sage and C.C. White. Optimum Systems Control. Prentice-Hall, Inc, 2nd edition, 1977.

[28] M.D. Shuster and W.F. Dellinger. spacecraft attitude determination and control. *Fundamentals of Space Systems*, pages 2nd Edition. 236–325, Ed. V.L. Pisacane. 2005. Oxford University Press.

[29] J.E. Slotine and W. Li. Applied Nonlinear Control. Prentice-Hall, 1991.

[30] R.F. Stengel. Optimal Control and Estimation. Dover Publications, Inc, 1994.

[31] D.H. Titterton. Strapdown Inertial Navigation Technology . Institution of Engineering and Technology, 2nd edition, 2004.

[32] B. Wie. Space Vehicle Dyanmics and Control . American Institute of Aeronautics and Astronautics, 1998.

[33] S. Ying. Advanced Dynamics . American Institute of Aeronautics and Astronautics, 1997.

[34] P. Zarchan and H. Musoff. Fundamentals of Kalman Filtering: A Practical Approach . Progress in Astronautics and Aeronautics. American Institute of Aeronautics and Astronautics, 2nd edition, 2005.

Appendices

Appendix A

Aerospace Transformation Sequence

A.1 Translational Vector [22, 33]

The following figures and trigonometric identities provide the derivation of the rotation matrices for resolving displacements in a reference frame to a secondary frame via a rotation angle about a frame axis. The aerospace sequence of rotations is given to derive the displacements performed in a reference frame to a secondary rotated frame.

Consider an angle rotation, ϕ, about the tertiary axis as shown in Figure A.1. Equation, A.1 relates the displacements in reference frame to the x'-y'-z' frame.

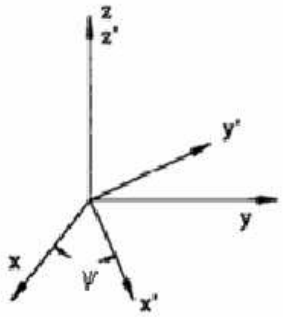

Figure A.1: Rotation about the Tertiary Axis [33]

$$R3 = \begin{bmatrix} \cos\psi & \sin\psi & 0 \\ -\sin\psi & \cos\psi & 0 \\ 0 & 0 & 1 \end{bmatrix} \tag{A.1}$$

Consider an angle rotation, θ, about the secondary axis as shown in Figure A.2. Equation, A.2 relates the displacements in reference frame to the x'-y'-z' frame.

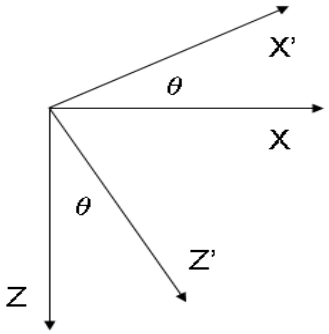

Figure A.2: Rotation about the Secondary Axis

$$R2 = \begin{bmatrix} \cos\theta & 0 & -\sin\theta \\ 0 & 1 & 0 \\ \sin\theta & 0 & \cos\theta \end{bmatrix} \tag{A.2}$$

Consider an angle rotation, ϕ, about the primary axis as shown in Figure A.3. Equation, A.3 relates the displacements in reference frame to the x'-y'-z' frame.

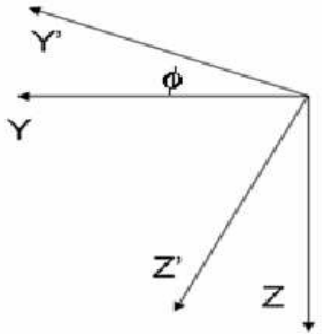

Figure A.3: Rotation about the Primary Axis

$$R1 = \begin{bmatrix} 1 & 0 & 0 \\ 0 & \cos\psi & \sin\psi \\ 0 & -\sin\psi & \cos\psi \end{bmatrix} \tag{A.3}$$

The general equation for a rotation angle, β about a particular normalized axis, $\hat{\mathbf{a}}$, is given by Equation A.4 found in [28].

$$R(\beta, \hat{\mathbf{a}}) = \cos\beta\ \mathbf{I} + (1 - \cos\beta)\,\hat{\mathbf{a}}\hat{\mathbf{a}}^T - \sin\beta\,[\mathbf{a}\times] \tag{A.4}$$

$$Where:\ [\hat{\mathbf{a}}\times] = \begin{bmatrix} 0 & -a_3 & a_2 \\ a_3 & 0 & -a_1 \\ -a_2 & a_1 & 0 \end{bmatrix}$$

A.2 Rotation Rate Vector [22]

In a similar fashion the time rate change of the Euler Angles can be related to the vehicle's experienced rotation rates. Consideration must be taken because the bank angle, ϕ is relative to the rotation about the primary axis, θ is relative to the rotations about the secondary and then primary axes, and ψ is relative to rotations about the tertiary, secondary, and primary axes. This results in Equation A.5 yielding the transformation between the Euler angular rates and the vehicle rates.

$$\begin{Bmatrix} p \\ q \\ r \end{Bmatrix} = \begin{bmatrix} 1 & 0 & 0 \\ 0 & C\phi & S\phi \\ 0 & -S\phi & C\phi \end{bmatrix} \begin{Bmatrix} \dot{\phi} \\ 0 \\ 0 \end{Bmatrix} + \begin{bmatrix} 1 & 0 & 0 \\ 0 & C\phi & S\phi \\ 0 & -S\phi & C\phi \end{bmatrix} \begin{bmatrix} C\theta & 0 & -S\theta \\ 0 & 1 & 0 \\ S\theta & 0 & C\theta \end{bmatrix} \begin{Bmatrix} 0 \\ \dot{\theta} \\ 0 \end{Bmatrix} + \begin{bmatrix} 1 & 0 & 0 \\ 0 & C\phi & S\phi \\ 0 & -S\phi & C\phi \end{bmatrix} \begin{bmatrix} C\theta & 0 & -S\theta \\ 0 & 1 & 0 \\ S\theta & 0 & C\theta \end{bmatrix} \begin{bmatrix} C\psi & S\psi & 0 \\ -S\psi & C\psi & 0 \\ 0 & 0 & 1 \end{bmatrix} \begin{Bmatrix} 0 \\ 0 \\ \dot{\psi} \end{Bmatrix} \tag{A.5}$$

Equation A.5 can be reduced to Equation A.6

$$\begin{Bmatrix} p \\ q \\ r \end{Bmatrix} = \begin{bmatrix} 1 & 0 & -S\theta \\ 0 & C\phi & S\phi C\theta \\ 0 & -S\phi & C\phi C\theta \end{bmatrix} \begin{Bmatrix} \dot{\phi} \\ \dot{\theta} \\ \dot{\psi} \end{Bmatrix} \tag{A.6}$$

The 3 element by 3 element matrix in Equation A.6 is nonorthogonal requiring execution of matrix inverse operations to attain the transform relating vehicle rates to Euler rates. Equation A.7 displays the transform and mathematically shows the phenomenon of Gimbal Lock where $\dot{\phi}$ and $\dot{\psi}$ cannot be computed due to a divide by zero error since the two axes are aligned with each other. The matrix inverse operation can be carried out using the steps listed in any linear algebra textbook such as [5] and thus are not explicitly stated here.

$$\begin{Bmatrix} \dot{\phi} \\ \dot{\theta} \\ \dot{\psi} \end{Bmatrix} = \begin{bmatrix} 1 & S\phi S\theta/C\theta & C\phi S\theta/C\theta \\ 0 & C\phi & -S\phi \\ 0 & -S\phi/C\theta & C\phi/C\theta \end{bmatrix} \begin{Bmatrix} p \\ q \\ r \end{Bmatrix} \tag{A.7}$$

Appendix B

Quaternion Mathematics

This Appendix section provides additional mathematical background of quaternion operations and relationships taken from [16] and [22].

B.1 Quaternion Algebra

Given two quaternions, denoted $\mathbf{P}$ and $\mathbf{Q}$, their representative elements are given in Equation B.1 the hypercomplex form.

$$\begin{aligned} \mathbf{P} &= p_0 + p_1\hat{\mathbf{i}} + p_2\hat{\mathbf{j}} + p_3\hat{\mathbf{k}} = p_0 + \mathbf{p} \\ \mathbf{Q} &= q_0 + q_1\hat{\mathbf{i}} + q_2\hat{\mathbf{j}} + q_3\hat{\mathbf{k}} = q_0 + \mathbf{q} \end{aligned} \tag{B.1}$$

Given a scalar constant, C, multiplication of a quaternion by a scalar constant is shown in Equation B.2.

$$C\mathbf{P} = Cp_0 + Cp_1\hat{\mathbf{i}} + Cp_2\hat{\mathbf{j}} + Cp_3\hat{\mathbf{k}} = Cp_0 + C\mathbf{p} \tag{B.2}$$

The derivation of the quaternion inverse is shown below:

Given $\mathbf{Q}^{-1}\mathbf{Q} = \mathbf{Q}\mathbf{Q}^{-1} = 1$ *by definition of the inverse*
Multiply by quaternion conjugate $\mathbf{Q}^*$
$\mathbf{Q}^{-1}\mathbf{Q}\mathbf{Q}^* = \mathbf{Q}^*\mathbf{Q}\mathbf{Q}^{-1} = \mathbf{Q}^*$
Since $\mathbf{Q}\mathbf{Q}^*$ *equals the square of the norm,* $N(\mathbf{Q})$
$\mathbf{Q}^{-1} = \frac{\mathbf{Q}^*}{N^2(\mathbf{Q})}$
Since the unit quaternion is used the norm is equal to 1 *thus..*
$\mathbf{Q}^{-1} = \mathbf{Q}^* = q_0 - \mathbf{q}$

B.2 Equating Euler Angles with Aerospace Sequence Quaternion

We begin by equating the reference to vehicle transforms of 2.29 to 2.15

$$\begin{bmatrix} 2q_0^2 - 1 + 2q_1^2 & 2q_1q_2 + 2q_0q_3 & 2q_1q_3 - 2q_0q_2 \\ 2q_1q_2 - 2q_0q_3 & 2q_0^2 - 1 + 2q_2^2 & 2q_2q_3 + 2q_0q_1 \\ 2q_1q_3 + 2q_0q_2 & 2q_2q_3 - 2q_0q_1 & 2q_0^2 - 1 + 2q_3^2 \end{bmatrix} =$$
$$\begin{bmatrix} C\theta C\psi & C\theta S\psi & -S\theta \\ S\phi S\theta C\psi - C\phi S\psi & S\phi S\theta S\psi + C\phi C\psi & S\phi C\theta \\ C\phi S\theta C\psi + S\phi S\psi & C\phi S\theta S\psi - S\phi C\psi & C\phi C\theta \end{bmatrix} \tag{B.3}$$

By understanding the magnitude of the quaternion must be equal to 1 and make the substitution into the diagonal elements of the quaternion transformation matrix, the diagonal elements of both transforms can be equated as follows:

$$\begin{bmatrix} 1 & 1 & -1 & -1 \\ 1 & -1 & 1 & -1 \\ 1 & -1 & -1 & 1 \\ 1 & 1 & -1 & -1 \end{bmatrix} \begin{Bmatrix} q_0^2 \\ q_1^2 \\ q_2^2 \\ q_3^2 \end{Bmatrix} = \begin{Bmatrix} C\theta C\psi \\ S\phi S\theta S\psi + C\phi C\psi \\ C\phi C\theta \\ 1 \end{Bmatrix} \tag{B.4}$$

The above matrix equation can be directly solved yielding:

$$\begin{Bmatrix} q_0^2 \\ q_1^2 \\ q_2^2 \\ q_3^2 \end{Bmatrix} = \begin{Bmatrix} \left(C_{\phi/2}C_{\theta/2}C_{\psi/2} + S_{\phi/2}S_{\theta/2}S_{\psi/2}\right)^2 \\ \left(S_{\phi/2}C_{\theta/2}C_{\psi/2} - C_{\phi/2}S_{\theta/2}S_{\psi/2}\right)^2 \\ \left(C_{\phi/2}S_{\theta/2}C_{\psi/2} + S_{\phi/2}C_{\theta/2}S_{\psi/2}\right)^2 \\ \left(S_{\phi/2}S_{\theta/2}C_{\psi/2} - C_{\phi/2}C_{\theta/2}S_{\psi/2}\right)^2 \end{Bmatrix} \tag{B.5}$$

There are two possible solutions for each element in Equation B.5, thus the off-diagonal elements of Equation B.3 are set equal to each to provide additional information.

$$\begin{Bmatrix} q_0q1 \\ q_0q2 \\ q_0q3 \\ q_1q2 \\ q_1q3 \\ q_2q3 \end{Bmatrix} = \frac{1}{4} \begin{Bmatrix} S_\phi C_\theta - C_\phi S_\theta S_\psi + S_\phi C_\psi \\ C_\phi S_\theta C_\psi + S_\phi S_\psi + S_\theta \\ S_\psi C_\theta - S_\phi S_\theta C_\psi + C_\phi S_\psi \\ S_\psi C_\theta + S_\phi S_\theta C_\psi - C_\phi S_\psi \\ C_\phi S_\theta C_\psi + S_\phi S_\psi - S_\theta \\ S_\phi C_\theta + C_\phi S_\theta S_\psi - S_\phi C_\psi \end{Bmatrix} \tag{B.6}$$

Using the trigonometric half-angle formulas to extract element signs, Equation B.6 provides information that $s_0s_1 = 1,\ s_0s_2 = 1,$ and $s_0s_3 = -1$, where $s_\#$ indicates the sign of $q_\#$.

Using this information in Equation B.5 becomes Equation 2.36 and is shown again below:

$$\left\{ \begin{array}{c} q_0 \\ q_1 \\ q_2 \\ q_3 \end{array} \right\} = \pm \left\{ \begin{array}{c} \cos\frac{\phi}{2}\cos\frac{\theta}{2}\cos\frac{\psi}{2} + \sin\frac{\phi}{2}\sin\frac{\phi}{2}\sin\frac{\phi}{2} \\ \sin\frac{\phi}{2}\cos\frac{\theta}{2}\cos\frac{\psi}{2} - \cos\frac{\phi}{2}\sin\frac{\phi}{2}\sin\frac{\phi}{2} \\ \cos\frac{\phi}{2}\sin\frac{\theta}{2}\cos\frac{\psi}{2} + \sin\frac{\phi}{2}\cos\frac{\phi}{2}\sin\frac{\phi}{2} \\ \cos\frac{\phi}{2}\cos\frac{\theta}{2}\sin\frac{\psi}{2} - \sin\frac{\phi}{2}\sin\frac{\phi}{2}\cos\frac{\phi}{2} \end{array} \right\} \tag{B.7}$$

B.3 Quaternion Calculus

Quaternion Derivative Derivation

From Section 2.1.4 and Equation 2.23.

$$\mathbf{Q} = \left\{ \begin{array}{c} q_0 \\ q_1 \\ q_2 \\ q_3 \end{array} \right\} = \left\{ \begin{array}{c} \cos\frac{\Theta}{2} \\ E_x \sin\frac{\Theta}{2} \\ E_y \sin\frac{\Theta}{2} \\ E_z \sin\frac{\Theta}{2} \end{array} \right\} = q_0 + q_1\mathbf{i} + q_2 + \mathbf{j} + q_3\mathbf{k} = \left\{ \begin{array}{c} q_0 \\ \mathbf{q} \end{array} \right\} \tag{B.8}$$

Equation B.8 can be differentiated to yield the following:

$$\left\{ \begin{array}{c} \dot{q_0} \\ \dot{q_1} \\ \dot{q_2} \\ \dot{q_3} \end{array} \right\} = \left\{ \begin{array}{c} -\sin\frac{\Theta}{2} \\ E_x \cos\frac{\Theta}{2} \\ E_y \cos\frac{\Theta}{2} \\ E_z \cos\frac{\Theta}{2} \end{array} \right\} \frac{\dot{\Theta}}{2} + \left\{ \begin{array}{c} 0 \\ \dot{E}_x \sin\frac{\Theta}{2} \\ \dot{E}_y \sin\frac{\Theta}{2} \\ \dot{E}_z \sin\frac{\Theta}{2} \end{array} \right\} \tag{B.9}$$

Using Equation 2.22 for expression of the time rate change of the Euler axis parameters, Equation B.9 can be combined to yield the following:

$$\left\{ \begin{array}{c} \dot{q_0} \\ \dot{q_1} \\ \dot{q_2} \\ \dot{q_3} \end{array} \right\} = \frac{1}{2} \left[\begin{array}{ccc} -q_1 & -q_2 & -q_3 \\ q_0 & -q_3 & q_2 \\ q_3 & q_0 & -q_1 \\ -q_2 & q_1 & -q_0 \end{array} \right] \left\{ \begin{array}{c} p \\ q \\ r \end{array} \right\} \tag{B.10}$$

Because Equation B.10 is linear in both the Euler symmetric parameters and the noninertial angular rates, it can also be written as the form given in Equations 2.40 and 2.41 :

$$\left\{ \begin{array}{c} \dot{q_0} \\ \dot{q_1} \\ \dot{q_2} \\ \dot{q_3} \end{array} \right\} = \frac{1}{2} \left[\begin{array}{cccc} 0 & -p & -q & -r \\ p & 0 & r & -q \\ q & -r & 0 & p \\ r & q & -p & 0 \end{array} \right] \left\{ \begin{array}{c} q_0 \\ q_1 \\ q_2 \\ q_3 \end{array} \right\} \tag{B.11}$$

Quaternion Integral Derivation with Constant Rotation

From Equation 2.40 we have:

$$\dot{\mathbf{Q}} = \Omega\mathbf{Q} \tag{B.12}$$

Where:

$$\Omega = \frac{1}{2}\begin{Bmatrix} 0 & -\vec{\omega}^T \\ \vec{\omega} & -[\vec{\omega}\times] \end{Bmatrix} = \frac{1}{2}\begin{Bmatrix} 0 & -p & -q & -r \\ p & 0 & r & -q \\ q & -r & 0 & p \\ r & q & -p & 0 \end{Bmatrix} \tag{B.13}$$

$$With\ :\qquad \vec{\omega} = \begin{bmatrix} p & q & r \end{bmatrix}^T$$

$$[\vec{\omega}\times] = \begin{bmatrix} 0 & -r & q \\ r & 0 & -p \\ -q & p & 0 \end{bmatrix} \tag{B.14}$$

Which can then be solved via first order separable homogeneous differential equation techniques:

$$\frac{\dot{\mathbf{Q}}}{\mathbf{Q}} = \Omega \tag{B.15}$$

$$\int \frac{\dot{\mathbf{Q}}}{\mathbf{Q}} dt = \int \Omega\ dt \tag{B.16}$$

$$\mathbf{ln}\left(\mathbf{Q}\right) = \Omega t + C \tag{B.17}$$

$$\mathbf{Q} = C\mathbf{exp}\left[\Omega t\right] \tag{B.18}$$

Where C is a constant with the value of $\mathbf{Q}_{t=t_0}$ and **exp** is the matrix exponential. The scalar and matrix exponential series expansions are given by the following:

Scalar:

$$e^x = \mathbf{exp}\left[x\right] = 1 + x + \frac{x^2}{2!} + \frac{x^3}{3!}\cdots + \frac{x^n}{n!} \tag{B.19}$$

Matrix:

$$e^{\mathbf{A}} = \mathbf{exp}\left[\mathbf{A}\right] = \mathbf{I}_{n\times n} + \mathbf{A} + \frac{\mathbf{AA}}{2!} + \frac{\mathbf{AAA}}{3!} + \ldots \tag{B.20}$$

$$Where:\ \mathbf{I}\ is\ the\ Identity\ Matrix$$

Letting **A**=Ωt gives the following by way of direct matrix multiplication of Equation 2.41 or Equation B.13:

$$\Omega\Omega = -\frac{1}{4}|\vec{\omega}|^2\mathbf{I}_{4\times 4} \tag{B.21}$$

$$Where:\ |\vec{\omega}| = \sqrt{p^2+q^2+r^2}$$

Grouping odd and even power terms from the power series expansion of the matrix exponential and using Equation B.21's relationship:

$$e^{\Omega t} = \mathbf{I}_{4\times4}\left(1 - \frac{\lambda^2}{2!} + \frac{\lambda^4}{4!} + \dots\right) + \frac{2}{\omega}\Omega\left(\lambda - \frac{\lambda^3}{3!} + \frac{\lambda^5}{5!} + \dots\right) \tag{B.22}$$

$$Where:\ \lambda = \frac{|\vec{\omega}|t}{2}$$

Using substituting in the trigonometric terms for the power series expansions, Equation B.22 becomes:

$$e^{\Omega t} = \left[\mathbf{I}_{4\times4}\cos\left(\frac{\omega t}{2}\right) + \frac{2\Omega}{\omega}\sin\left(\frac{\omega t}{2}\right)\right] \tag{B.23}$$

Equation B.18 then becomes Equation 2.42:

$$\mathbf{Q} = \left[\mathbf{I}_{4\times4}\cos\left(\frac{\omega t}{2}\right) + \frac{2\Omega}{\omega}\sin\left(\frac{\omega t}{2}\right)\right]\mathbf{Q}_{t=t_0} \tag{B.24}$$

Integration of Quaternion Example

The integration of a Quaternion, $\mathbf{Q}_{t=t_0}$ with initial conditions of all Euler angles equal to zero, experiencing a constant generic rotation vector, $\vec{\omega}$, over a time period, t, results in the following solution:

$$\mathbf{Q}_{t=t_0} = \pm\begin{Bmatrix} \cos\frac{\phi}{2}\cos\frac{\theta}{2}\cos\frac{\psi}{2} + \sin\frac{\phi}{2}\sin\frac{\phi}{2}\sin\frac{\phi}{2} \\ \sin\frac{\phi}{2}\cos\frac{\theta}{2}\cos\frac{\psi}{2} - \cos\frac{\phi}{2}\sin\frac{\phi}{2}\sin\frac{\phi}{2} \\ \cos\frac{\phi}{2}\sin\frac{\theta}{2}\cos\frac{\psi}{2} + \sin\frac{\phi}{2}\cos\frac{\phi}{2}\sin\frac{\phi}{2} \\ \cos\frac{\phi}{2}\cos\frac{\theta}{2}\sin\frac{\psi}{2} - \sin\frac{\phi}{2}\sin\frac{\phi}{2}\cos\frac{\phi}{2} \end{Bmatrix} = \begin{Bmatrix} 1 \\ 0 \\ 0 \\ 0 \end{Bmatrix}$$

$$\vec{\omega} = [p\ q\ r]^T$$

$$\omega = \left(p^2 + q^2 + r^2\right)^{1/2}$$

$$\mathbf{Q} = \left[\mathbf{I}_{4\times4}\cos\left(\frac{\omega t}{2}\right) + \frac{2\Omega}{\omega}\sin\left(\frac{\omega t}{2}\right)\right]\mathbf{Q}_{t=t_0}$$

$$\mathbf{Q} = \begin{Bmatrix} cos\,(\omega t/2) \\ (p/\omega)\,sin\,(\omega t/2) \\ (q/\omega)\,sin\,(\omega t/2) \\ (r/\omega)\,sin\,(\omega t/2) \end{Bmatrix}$$

Appendix C

Analog Filter Derivations

Using the resistor-inductor-capacitor,RLC, circuit shown in Figure C.1, the transfer functions of first and second order low-pass and high-pass filters are derived. Additionally a second order bandpass filter is derived for completeness. The derivation for the first order filters requires only an RC circuit so the inductor of Figure C.1 is shorted.

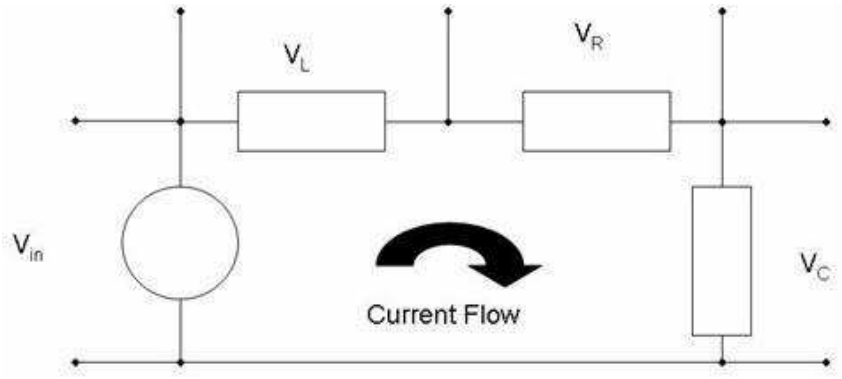

Figure C.1: Series RLC Circuit Diagram

C.1 First Order Filters

The following filters are derived with the inductor shorted in Figure C.1.

Low-Pass Filter

The low-pass filter transfer function is the ratio between the voltage across the capacitor, V_C, and the total voltage in the circuit, V_{IN}. The total voltage in the circuit is given by Equation C.1 with the voltage across the resistor and capacitor given by Equations C.2

and C.3 respectively.

$$V_{IN} = V_R + V_C \tag{C.1}$$
$$V_R = Ri \tag{C.2}$$
$$\dot{V_C} = \frac{1}{C} i \tag{C.3}$$

Taking the Laplace transform of Equation C.1 and substituting in for the resistor and capacitor voltages yields Equation C.4.

$$V_{IN}(s) = RI(s) + V_C(s) = RI(s) + \frac{I(s)}{Cs} \tag{C.4}$$

Substituting in for the $I(s)$ term in the resistor voltage by rearranging the Laplace transform of Equation C.3 yields Equation C.5 which can be rearranged to yield the low-pass filter transfer function given in Equation C.6.

$$V_{IN}(s) = RCV_C(s) + V_C(s) \tag{C.5}$$
$$\frac{V_C}{V_{IN}}(s) = \frac{1}{RCs + 1} \tag{C.6}$$

The time constant, τ, is equal to the product of the resistor and capacitor values and is equal to the inverse of the product of the damping ratio and the system natural frequency. Equation C.6 can then be rearranged to given Equation 2.46.

$$\tau = RC = \frac{1}{\zeta\omega_n}$$
$$\frac{V_C}{V_{IN}}(s) = \frac{\zeta\omega_n}{s + \zeta\omega_n}$$

High-Pass Filter

This derivation is similar to the low-pass filter except the Laplace transform of the current is substituted into the voltage across the capacitor instead of the voltage across the resistor in Equation C.4 to yield Equation C.7. Equations C.2 and C.3 are rearranged after their Laplace transform is taken and then substituted into Equation C.4

$$I(s) = V_C(s)\,Cs$$
$$I(s) = \frac{V_R}{R}$$
$$V_{IN}(s) = V_R(s) + \frac{V_R(s)}{RCs} \tag{C.7}$$

This leads to the high-pass filter transfer function as the ratio of the voltage across the resistor to the voltage across the entire circuit. Again the time constant is the same as the low-pass filter, yielding Equation 2.47.

$$\frac{V_R}{V_{IN}} = \frac{RCs}{RCs + 1} = \frac{s}{s + \zeta\omega_n}$$

C.2 Second Order Filters

The second order filters are derived using the full RLC circuit given in Figure C.1. Table C.1 summarizes the time domain and Laplace domain equations governing the voltage across each element.

Element	Time Domain	Laplace Domain	Current in Laplace Domain
Resistor	$V_R = Ri$	$V_R(s) = RI(s)$	$I(s) = \frac{V_R(s)}{R}$
Inductor	$V_L = L\frac{di}{dt}$	$V_L(s) = LI(s)\,s$	$I(s) = \frac{V_L(s)}{Ls}$
Capacitor	$\frac{dV_C}{dt} = \frac{i}{C}i$	$V_C(s)\,s = \frac{1}{C}I(s)$	$I(s) = V_C(s)\,Cs$

Table C.1: Voltage Equations: Time and Laplace Domain

Summing the voltage drops throughout the circuit and setting them equal to the circuit voltage gives Equation C.8.

$$V_{IN} = V_L + V_R + V_C \tag{C.8}$$

Low-Pass Filter

Transforming Equation C.8 into the Laplace domain with the inductor and resistor voltages in terms of the current and then substituting current in terms of capacitor voltage yields the second order low-pass filter given in Equation C.9 for a Low-Pass Filter.

$$\begin{aligned} (Ls + R)\,I(s) + V_C(s) &= V_{IN}(s) \\ (Ls + R)\,V_C(s)\,Cs + V_C(s) &= V_{IN}(s) \\ \frac{V_C}{V_{IN}}(s) = \frac{1}{LCs^2 + RCs + 1} &= \frac{\frac{1}{LC}}{s^2 + \frac{R}{L}s + \frac{1}{LC}} \end{aligned} \tag{C.9}$$

High-Pass Filter

Doing the same as above only solving for the voltage across the inductor, Equation C.10 for the high-pass filter is derived.

$$\begin{aligned} V_L + \left(\frac{1}{Cs} + R\right) I(s) &= V_{IN} \\ V_L + \left(\frac{1}{Cs} + R\right) \frac{V_L(s)}{Ls} &= V_{IN} \\ \frac{V_L}{V_{IN}}(s) = \frac{1}{1 + \frac{1}{LCs^2} + \frac{R}{Ls}} = \frac{LCs^2}{LCs^2 + RCs + 1} &= \frac{s^2}{s^2 + \frac{R}{L}s + \frac{1}{LC}} \end{aligned} \tag{C.10}$$

Bandpass Filter

Repeating again but solving for the voltage across the resistor yields Equation C.11 for a bandpass filter.

$$V_R + \left(Ls + \frac{1}{Cs}\right) I(s) = V_{IN}$$
$$V_R + \left(Ls + \frac{1}{Cs}\right) \frac{V_R(s)}{R} = V_{IN}$$
$$\frac{V_R}{V_{IN}}(s) = \frac{1}{1 + \frac{L}{R}s + \frac{1}{RCs}} = \frac{RCs}{LCs^2 + RCs + 1} = \frac{\frac{R}{L}s}{s^2 + \frac{R}{L}s + \frac{1}{LC}} \tag{C.11}$$

Filter Form Character

From the characteristic second order equation given in terms of damping ratio and natural frequency:

$$Characteristic\ Equation = s^2 + 2\zeta\omega_n s + \omega_n^2$$

We can define the following:

$$\omega_n^2 = \frac{1}{LC}$$
$$2\zeta\omega_n = \frac{R}{L}$$
$$\tau = \frac{1}{\zeta\omega_n} = \frac{2L}{R}$$

The low, high, and bandpass filter equations can then be put in terms of the general second order characteristic equation using the above defined relationships. Table C.2 summarizes these equations.

Filter Type	Derived	General 2^{nd} Order
Low-Pass	$\frac{\frac{1}{LC}}{s^2+\frac{R}{L}s+\frac{1}{LC}}$	$\frac{\omega_n^2}{s^2+2\zeta\omega_n+\omega_n^2}$
High-Pass	$\frac{s^2}{s^2+\frac{R}{L}s+\frac{1}{LC}}$	$\frac{s^2}{s^2+2\zeta\omega_n+\omega_n^2}$
Bandpass	$\frac{\frac{R}{L}s}{s^2+\frac{R}{L}s+\frac{1}{LC}}$	$\frac{2\zeta\omega_n s}{s^2+2\zeta\omega_n+\omega_n^2}$

Table C.2: 2^{nd} Order Filter Equations

C.3 Butterworth Filter

The analog Butterworth Filter is a type of low-pass analog filter that does not possess any oscillations when rolling off from the passband frequencies. The calculation of the denominator coefficients in the Laplace domain is given by Equation C.12. [24]

$$c_k = \Omega_c e^{j\pi/2} e^{j(2k+1)\pi/(2N)} \tag{C.12}$$

Where Ω_c is the cutoff frequency of the filter in radians, N is the order of the filter, c is the coefficient magnitude, and k is the power of s in the Laplace domain associated with the coefficient going from 0 to N-1. The Butterworth filter has a unity DC gain of 1, thus the coefficient of the numerator is equivalent to the coefficient of the denominator associated with the s^0 term in the Laplace domain.

A MATLaB®script was written to output the numerator and denominator of the filter based upon the desired order and cutoff frequency and is given below.

```
function [num,den]=mybuttercompute(n,wc)
ii=1;
for ii=1:n
    sk(ii)=wc*exp((2*ii+n-1)*j*pi/(2*n));
    if ii==1
        den=[1 -sk(ii)];
    else
        den=conv(den,[1 -sk(ii)]);
    end
end
num=den(end);
num=real(num);
den=real(den);
```

The following two examples show that the above code produces the same output for the Butterworth transfer function as the MATLab command "butter".

Example 1

For a second order filter with a cutoff frequency of 15 radians per second, the following output is produced:

```
num = [225]
den = [1.0000 21.2132 225.0000]
```

The following output is produced using the "butter"command in MATLaB:

n = [0 0 225]
d = [1.0000 21.2132 225.0000]

Example 2

For a fourth order filter with a cutoff frequency of 15 radians per second, the following output is produced:

num = [5.0625e+004]
den = 1.0e+004*[0.0001 0.0039 0.0768 0.8819 5.0625]

The following output is produced using the "butter"command in MATLaB:

n =1.0e+004*[0 0 0 0 5.0625]
d =1.0e+004*[0.0001 0.0039 0.0768 0.8819 5.0625]

Appendix D

Kalman Filter Supplement

D.1 Statistic Information Supplement [8, 20]

Table D.1 summarizes the calculation of the statistic variables used in the construction of a Kalman Filter.Note the variables can be either scalar or column vectors for the covariance matrices.

Variable	Calculation	Description
$\mathbf{x}$	Measured/Estimated	State Vector - 2 rows×1 column
x	Measured/Estimated	State Scalar
$\mathbf{w} \sim N(0, \mathbf{Q})$	Random Number	$\mathbf{w}$ is normally distributed between 0 and $\mathbf{Q}$
$\mu = \mathrm{E}\{x\}$	$\int_{-\infty}^{\infty} x \mathrm{pdf}[x,t]\, dx$	Mean or Scalar Expectation of x given its probability density function
$\sigma^2 = \mathrm{V}\{x\}$	$\int_{-\infty}^{\infty} (x-\mu)^2 \mathrm{pdf}[x,t]\, dx$	Variance or expected variability of x given its probability density function
σ	$[V\{x\}]^{1/2}$	Standard Deviation of x
P	$\mathrm{E}\left\{(\hat{\mathbf{x}}-\mathbf{x})(\hat{\mathbf{x}}-\mathbf{x})^T\right\}$	State Error Covariance Matrix
Q	$\begin{bmatrix} E\{p^2\} & E\{pq\} \\ E\{pq\} & E\{q^2\} \end{bmatrix}$	Process Noise Covariance where p and q are power spectral densities of $\mathbf{x}$ states
R	$\mathrm{E}\left\{(x-\mu_x)(x-\mu_x)^T\right\}$	Measurement Noise Covariance

Table D.1: Statistic Variable Definitions

For a scalar, x, Gaussian variable the probability density function is given in Equation

D.1 and for a vector, $\mathbf{x}$, Equation D.2 holds true.

$$pdf\,[x,t] = \frac{1}{\sigma\sqrt{2\pi}}\exp\left[-\frac{(x-\mu)^2}{2\sigma^2}\right] \tag{D.1}$$

$$pdf\,[\mathbf{x},t] = \frac{1}{[det\,(2\pi R)]^{1/2}}\exp\left[-\frac{1}{2}(\mathbf{x}-\mu)^T R^{-1}(\mathbf{x}-\mu)\right] \tag{D.2}$$

For a zero mean Gaussian white noise processes the following hold true:

$$\mathbf{E}\{x\} = \mu = 0 \tag{D.3}$$

$$\sigma^2 = \mathbf{E}\left\{(x-\mu)^2\right\} \tag{D.4}$$

For a Gaussian or Normal Distribution with a given mean and standard deviation has its data distributed about the mean according to Table D.2.

Bounds	Percentage of produced data lying within bounds
$\mu \pm 1\sigma$	68.3%
$\mu \pm 2\sigma$	95.5%
$\mu \pm 3\sigma$	99.7%

Table D.2: Data Dispersion of Normal Distribution with given μ and σ^2

Central Limit Theorem. *If $X_1, X_2, \ldots, X_n$ is a random sample of size n take from a population (either finite or infinite) with mean μ and finite variance σ^2, and if $\bar{X}$ is the sample mean, then the limiting form of the distribution is*

$$Z = \frac{\bar{X}-\mu}{\sigma/\sqrt{n}}$$

as $n \to \infty$, the normal distribution is produced with mean, μ, and variance,$\frac{\sigma^2}{n}$, no matter the shape of the original distribution.

D.2 Continuous to Discrete Transformation [24, 34]

In the continuous time domain, a continuous data stream exists which completely resembles what is being measured, such as analog measurement of voltage via a voltmeter. However digital computers sample this continuous stream at discrete points separated by a sampling time interval resulting in nonexistent data in between samples. Reproduction of a continuous signal from discrete data points requires the data to be extrapolated using recursive techniques or held constant. The latter is known as a zero-order hold with the

former being the basis for a first-order hold, a second-order hold and so on depending on the recursive extrapolation technique based upon a priori knowledge of the data form.

The conversion from continuous time matrices to discrete time matrices can be done using several methods, the most common are derivative approximations and the bilinear or "Tustin"transformation [24]. Both make approximations of the relationship between the Laplace domain variable, s, and the discrete domain variable, z, given by Equation D.5 with sampling interval T using the first order Padé approximant given in Equation D.6. The discrete matrix, $\mathbf{T}_k$, is found by substituting the "s"as a function of "z"relationship into the Laplace transform of the continuous matrix, $\mathbf{T}$(t), shown in Equation D.7.

$$z = e^{sT} \tag{D.5}$$

$$z = e^{sT} \approx \frac{1}{1 - sT} \tag{D.6}$$

$$\mathbf{T}_k = \mathbf{T}\left(s\right)|_{s=f(z)} \tag{D.7}$$

The derivative methods rearranges the Padé approximation shown in Equation D.8 for the "s"substitution of the nth derivative. For a *Zero-Order Hold* n=1 and for a *First-Order Hold* n=2.

$$s^n = \left(\frac{1 - z^{-1}}{T}\right)^n \tag{D.8}$$

If the transfer function resembles a high pass filter, the derivative approximation is unable to convert the function from the Laplace to discrete domain due to the restricted pole locations. The Bilinear transformation manipulates the "z"to "s"transform shown in Equation D.9 and then applies the first order Padé approximant as shown in Equation D.10 which is then substituted for "s"in Equation D.7.

$$z = e^{sT} = \frac{e^{sT/2}}{e^{-sT/2}} \tag{D.9}$$

$$z = \frac{e^{sT/2}}{e^{-sT/2}} \approx \frac{\frac{1}{1-sT/2}}{\frac{1}{1+sT/2}} \Rightarrow s = \frac{2}{T}\frac{1 - z^{-1}}{1 + z^{-1}} \tag{D.10}$$

Another approach summarized in [34] uses a Taylor Series Expansion and the *Fundamental Matrix*, Φ, for a system which has a time invariant state transition matrix, textbfF, with no external input or noise. The state-space equation is given as:

$$\dot{\mathbf{x}} = \mathbf{F}\mathbf{x} \tag{D.11}$$

The fundamental matrix, Φ, can then be used to propagate the state forward as the other transforms do from any time t_0 to time t_f from the following equations using the inverse Laplace transform, $\mathscr{L}^{-1}$:

$$\mathbf{x}(t) = \Phi(t - t_0)\,\mathbf{x}(t_0) \tag{D.12}$$

$$Where \;:\; \Phi(t) = \mathscr{L}^{-1}\left[(s\mathbf{I} - \mathbf{F})^{-1}\right] \tag{D.13}$$

In lieu of taking the inverse Laplace transform, the fundamental matrix in continuous time can be approximated with a Taylor series expansion:

$$\Phi(t) = e^{\mathbf{F}t} = \mathbf{I} + \mathbf{F}t + \frac{(\mathbf{F}t)^2}{2!} + \cdots + \frac{(\mathbf{F}t)^n}{n!} \tag{D.14}$$

The discrete fundamental matrix, Φ_k can be found by evaluating the continuous fundamental matrix expansion at the sampling time, T_s, with a reasonable approximation given by using only the first two terms in the Taylor series expansion.

$$\Phi_k = \Phi(T_s) \tag{D.15}$$

Appendix E

Accelerometer Device Supplement

E.1 Accelerometer Offsets

Accelerometer	Offset from Accelerometer 7 - Deg (rad)
1	-90(-1.5708)
2	-75(-1.3090)
3	-60(-1.0472)
4	-45(-0.7854)
5	-30(-0.5236)
6	-15(-0.2618)
7	0(0)
8	15(0.2618)
9	30(0.5236)
10	45(0.7854)
11	60(1.0472)
12	75(1.3090)
13	90(1.5708)

Table E.1: Accelerometer Offsets with 13 Accelerometers

E.2 Resolution of Center of Gravity Acceleration to Device Location

To resolve the acceleration of the vehicle center of gravity to the device accelerometer locations, consider the inertial system to be **XYZ**, the vehicle system to be **xyz**, the distance from inertial frame origin to vehicle frame center of gravity to be **R**, the distance from the inertial frame origin to a particular accelerometer of the device to be **r**, the angular rotation rate of the vehicle to be $\vec{\omega}$ and the distance from the vehicle center of gravity to the same accelerometer as $\mathbf{r}'$. This is shown in Figure E.1 taken from [33]. For each accelerometer there will be a new $\mathbf{r}'$ vector. This derivation assumes the vehicle to be a rigid body with respect to how the device is mounted in the vehicle.

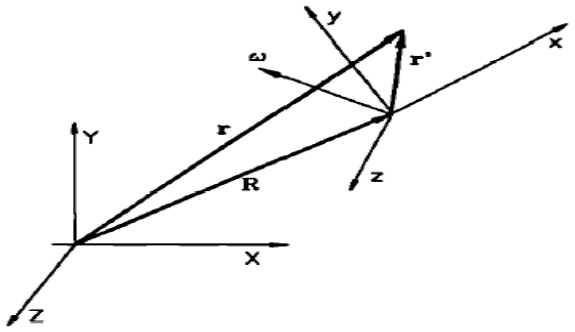

Figure E.1: Coordinate Systems from [33]

From vector algebra, we can express the distance between the inertial system center of gravity and the device center of gravity as Equation E.1.

$$\mathbf{r} = \mathbf{R} + \mathbf{r}' \tag{E.1}$$

Differentiating Equation E.1 yields Equation E.2 which is the velocity of the device in reference frame.

$$\begin{aligned} \dot{\mathbf{r}} &= \dot{\mathbf{R}} + \dot{\mathbf{r}}' + \vec{\omega} \times \mathbf{r}' \\ \mathbf{v}_i = \dot{\mathbf{r}} &= \dot{\mathbf{R}} + \dot{\mathbf{r}}' + \vec{\omega} \times \mathbf{r}' \end{aligned} \tag{E.2}$$

Where $\mathbf{v}_i$ represents the linear velocity experienced by the i^{th} accelerometer in the inertial coordinate system frame. The $\omega \times \mathbf{r}'$ term arises due to the rotation of the vehicle about the vehicle's center of gravity where ω is the rotation rate vector of the vehicle. Differentiating Equation E.2 yields the acceleration of the device in reference frame, Equation E.3 results from collecting terms and introducing acceleration as the second

derivative of position.

$$\ddot{\mathbf{r}} = \ddot{\mathbf{R}} + \ddot{\mathbf{r}'} + \vec{\omega} \times \dot{\mathbf{r}'} + \dot{\vec{\omega}} \times \mathbf{r}' + \vec{\omega} \times \dot{\mathbf{r}'} + \vec{\omega} \times \vec{\omega} \times \mathbf{r}'$$
$$\mathbf{a}_i = \ddot{\mathbf{r}} = \ddot{\mathbf{R}} + \ddot{\mathbf{r}'} + 2\left(\vec{\omega} \times \dot{\mathbf{r}'}\right) + \dot{\vec{\omega}} \times \mathbf{r}' + \vec{\omega} \times \vec{\omega} \times \mathbf{r}' \tag{E.3}$$

Where $\mathbf{a}_i$ represents the acceleration measured by the i^{th} accelerometer in the inertial coordinate system frame. The subsequent derivatives of the $\mathbf{R}$ vector are the velocity and acceleration vectors experienced by the center of gravity, origin, of the vehicle. Applying Newton's Second Law and assuming there is no change in mass of the vehicle:

$$\mathbf{F} = \frac{d}{dt}(m\mathbf{v}) = \cancelto{0}{\dot{m}\mathbf{v}} + m\dot{\mathbf{v}} = m\mathbf{a} \tag{E.4}$$

Since the vehicle is a rigid body $\mathbf{r}'$ is constant because it is the distance from the vehicle's center of gravity to the accelerometer locations of the device. Thus, the subsequent derivatives are zero and Equations E.5 and E.6 are brought about from Equations E.2 and E.3 respectively.

$$\mathbf{v}_i = \mathbf{v}_{veh} + \vec{\omega} \times \mathbf{r}' \tag{E.5}$$
$$\mathbf{a}_i = \ddot{R} + \dot{\vec{\omega}} \times \mathbf{r}' + \vec{\omega} \times \vec{\omega} \times \mathbf{r}' = \mathbf{a}_{veh} + \dot{\vec{\omega}} \times \mathbf{r}' + \vec{\omega} \times \vec{\omega} \times \mathbf{r}' \tag{E.6}$$

These equations define the velocity and acceleration at the accelerometer locations in inertial frame when the vehicle's center of gravity translational velocity and translational acceleration as well as the vehicle rotation rate and distance from vehicle center of gravity to device center of gravity are known. The last term of Equation E.5 and the last two terms of Equation E.6 represent the moment arm contributions to the measured velocity and acceleration of a displaced sensor.

Resolution of the vehicle accelerations at the center of gravity to the instrument location is only considered so Equation E.5 is not used. The sensor coordinate frame system is assumed to be orthogonal and only translated along the vehicle coordinate system axes. Carrying out the first cross-product for the i^{th} accelerometer we have:

$$\dot{\vec{\omega}} \times \mathbf{r}' = \begin{Bmatrix} \dot{p} \\ \dot{q} \\ \dot{r} \end{Bmatrix} \times \begin{Bmatrix} \bar{x}_i \\ \bar{y}_i \\ \bar{z}_i \end{Bmatrix} = \begin{Bmatrix} (\dot{q}\bar{z} - \dot{r}\bar{y})\,\hat{\mathbf{i}} \\ -(\dot{p}\bar{z} - \dot{r}\bar{x})\,\hat{\mathbf{j}} \\ (\dot{p}\bar{y} - \dot{q}\bar{x})\,\hat{\mathbf{k}} \end{Bmatrix} \tag{E.7}$$
$$Where: \begin{Bmatrix} \bar{x}_i \\ \bar{y}_i \\ \bar{z}_i \end{Bmatrix} = \begin{Bmatrix} x_{Accel,i} - x_{VehCG} \\ y_{Accel,i} - y_{VehCG} \\ z_{Accel,i} - z_{VehCG} \end{Bmatrix}$$

Carrying out the vector triple product we have:

$$\vec{\omega} \times \vec{\omega} \times \mathbf{r}' = \begin{Bmatrix} [(-q^2 - r^2)\,\bar{x}_i + pq\bar{y}_i + rp\bar{z}_i]\,\hat{\mathbf{i}} \\ -[-pq\bar{x}_i + (p^2 + r^2)\,\bar{y}_i - rq\bar{z}_i]\,\hat{\mathbf{j}} \\ [rp\bar{x}_i + rq\bar{y}_i + (-p^2 - q^2)\,\bar{z}_i]\,\hat{\mathbf{k}} \end{Bmatrix} \tag{E.8}$$

To resolve the accelerations of the vehicle's center of gravity to a the i^{th} accelerometer that is only translated along the vehicle's axes, Equations E.7 and E.8 are substituted into Equation E.6 to produce Equation E.9.

$$\mathbf{a}_i = \left\{ \begin{array}{c} a_x \\ a_y \\ a_z \end{array} \right\}_i = \left\{ \begin{array}{c} a_x \\ a_y \\ a_z \end{array} \right\}_{CG} + \left[\begin{array}{ccc} -(r^2+q^2) & (-\dot{r}+pq) & (\dot{q}+rp) \\ (\dot{r}+pq) & -(p^2+r^2) & (-\dot{p}+rq) \\ (-\dot{q}+rp) & (\dot{p}+rq) & -(p^2+q^2) \end{array} \right] \left\{ \begin{array}{c} \bar{x} \\ \bar{y} \\ \bar{z} \end{array} \right\}_i \tag{E.9}$$

Since the accelerometer array of the proposed device possesses accelerometers rotated about the vehicle's secondary coordinate axis, a transformation must be applied to Equation E.9 to account for axis misalignment. The angular displacements of the accelerometer from the vehicle axes are known, allowing for use of the reference frame to body frame transformation where the vehicle coordinate system is the reference frame and the accelerometer is the body rotated from the reference frame. Equations E.5 and E.6 now become:

$$\mathbf{v}_{i,misalign} = \mathbf{T}_{E2B} * \left[\mathbf{v}_i + \vec{\omega} \times \mathbf{r}'\right] \tag{E.10}$$

$$\mathbf{a}_{i,misalign} = \mathbf{T}_{E2B} * \left[\mathbf{a}_i + \dot{\vec{\omega}} \times \mathbf{r}' + \vec{\omega} \times \vec{\omega} \times \mathbf{r}'\right] \tag{E.11}$$

The transform $\mathbf{T}_{E2B}$ is known from Equation 2.15 but is stated again using the misalignment angles of the ith accelerometer:

$$\mathbf{T}_{E2B} = \left[\begin{array}{ccc} C\theta_i C\psi_i & C\theta_i S\psi_i & -S\theta_i \\ S\phi_i S\theta_i C\psi_i - C\phi_i S\psi_i & S\phi_i S\theta_i S\psi_i + C\phi_i C\psi_i & S\phi_i C\theta_i \\ C\phi_i S\theta_i C\psi_i + S\phi_i S\psi_i & C\phi_i S\theta_i S\psi_i - S\phi_i C\psi_i & C\phi_i C\theta_i \end{array} \right] \tag{E.12}$$

The accelerations of the vehicle center of gravity can now be resolved to the i^{th} accelerometer for each vehicle axis using Equations E.13, E.14, and E.15.

$$a_{X,i,misalign} = a_{x,i} C\left(\theta_{x,i}\right) C\left(\psi_{x,i}\right) + a_{y,i} C\left(\theta_{x,i}\right) S\left(\psi_{x,i}\right) - a_{z,i} S\left(\theta_{x,i}\right) \tag{E.13}$$

$$\begin{aligned} a_{Y,i,misalign} = {} & a_{x,i}\left[S\left(\phi_{y,i}\right) S\left(\theta_{y,i}\right) C\left(\psi_{y,i}\right) - C\left(\phi_{y,i}\right) S\left(\psi_{y,i}\right)\right] \\ & + a_{y,i}\left[S\left(\phi_{y,i}\right) S\left(\theta_{y,i}\right) S\left(\psi_{y,i}\right) + C\left(\phi_{y,i}\right) C\left(\psi_{y,i}\right)\right] \\ & + a_{z,i} S\left(\phi_{y,i}\right) C\left(\theta_{y,i}\right) \end{aligned} \tag{E.14}$$

$$\begin{aligned} a_{Z,i,misalign} = {} & a_{x,i}\left[C\left(\phi_{z,i}\right) S\left(\theta_{z,i}\right) C\left(\psi_{z,i}\right) + S\left(\phi_{z,i}\right) S\left(\psi_{z,i}\right)\right] \\ & + a_{y,i}\left[C\left(\phi_{z,i}\right) S\left(\theta_{z,i}\right) S\left(\psi_{z,i}\right) - S\left(\phi_{z,i}\right) C\left(\psi_{z,i}\right)\right] \\ & + a_{z,i} C\left(\phi_{z,i}\right) C\left(\theta_{z,i}\right) \end{aligned} \tag{E.15}$$

Where $C\left(\alpha_{\beta,i}\right)$ is the cosine of misalignment angle, β, from the respective vehicle axis for the i^{th} accelerometer and $S\left(\alpha_{\beta,i}\right)$ is the sine of the term inside the parentheses. The accelerations of $a_{x,i},\ a_{y,i},$ and $a_{z,i}$ have units of distance per second squared.

E.3 Accelerometer Measurements for Simulations

The following are the accelerometer measurements with white Gaussian noise for each accelerometer for each maneuver performed.

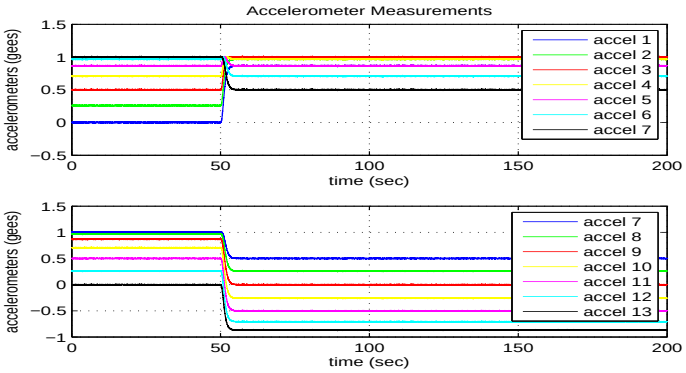

Figure E.2: Accel Measurements - Linear Model Step-and-Hold Maneuver

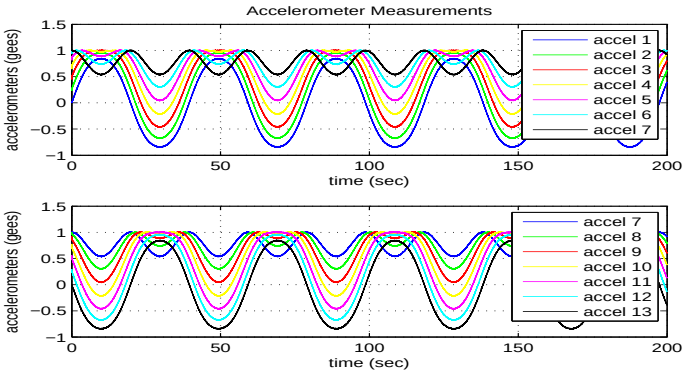

Figure E.3: Accel Measurements - Linear Model Sinusoid Maneuver

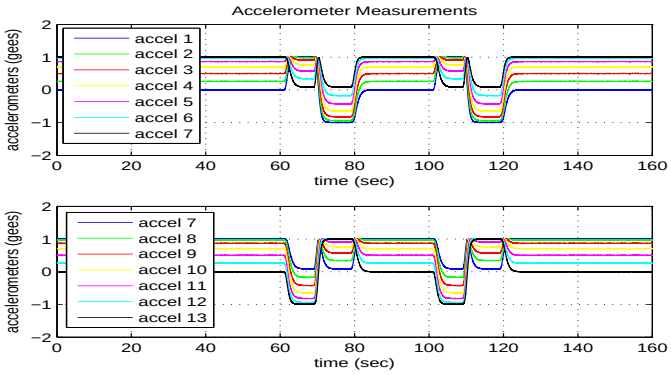

Figure E.4: Accel Measurements - Linear Model Pitch Doublet Maneuver

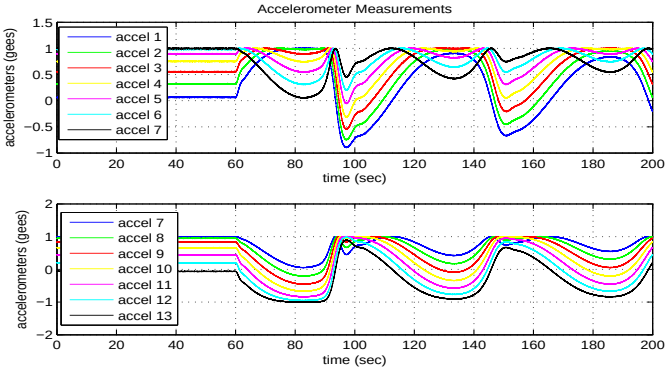

Figure E.5: Accel Measurements - Nonlinear Model with Rotational Only Maneuver

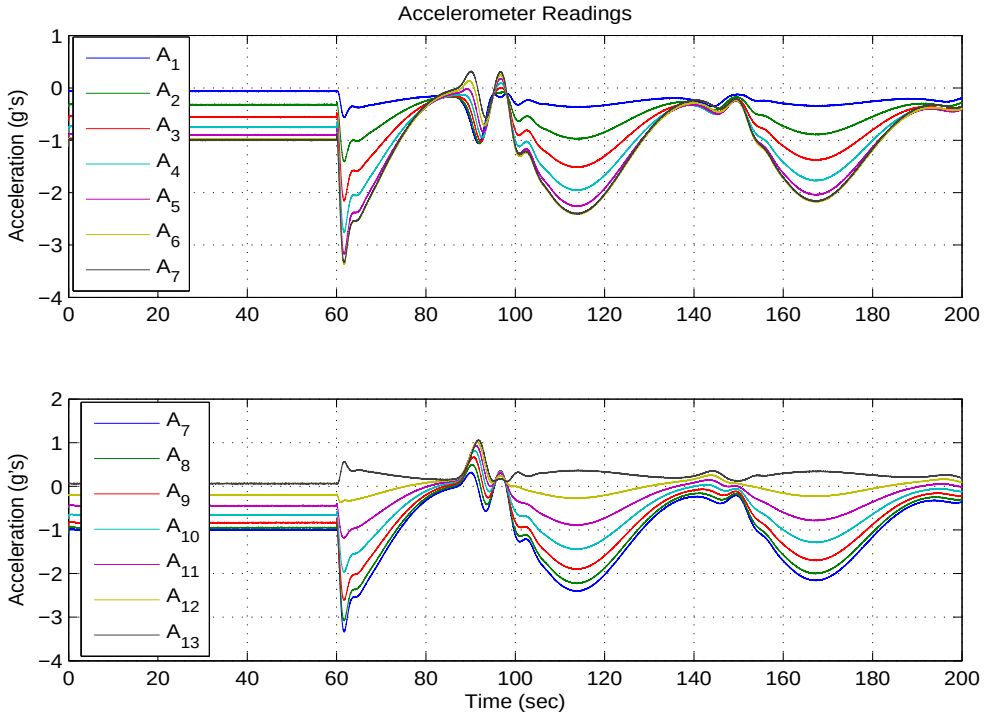

Figure E.6: Accel Measurements - Nonlinear Model Full Loading

Appendix F

Nonlinear Aircraft Model

F.1 Additional Modeling Equations

Additional equations besides the rigid body equations of motion 2.9, 2.10, 2.17, and 2.20 , given in Section 2.1.2 are needed to describe the motion of an aircraft. References [22], [21], and [33] provide added insight into derivation of the rigid-body nonlinear model.

Equations of Motion for Aircraft Stability Axes Coordinate System

The stability axes coordinate systems uses the true velocity of the aircraft, V_T, which is the magnitude of the body axes velocities along with the angle of attack, α which is the pitch angle of the aircraft relative to the oncoming wind, and β which is the yaw angle of the aircraft relative to the oncoming wind. The transformation equations from vehicle axes to stability axes are and vice-versa are:

Body to Stability:

$$\alpha = \tan^{-1} \frac{w}{u} \tag{F.1}$$

$$\beta = \sin^{-1} \frac{v}{V_T} \tag{F.2}$$

$$V_T = \sqrt{u^2 + v^2 + w^2} \tag{F.3}$$

Stability to Body:

$$u = V_T \cos\alpha \cos\beta \tag{F.4}$$

$$v = V_T \sin\beta \tag{F.5}$$

$$w = V_T \sin\alpha \cos\beta \tag{F.6}$$

The resulting force equations are:

$$\dot{\alpha} = q - (p\cos\alpha + r\sin\alpha)\tan\beta - \frac{LOM}{V_T\cos\beta} + \frac{g}{V_T\cos\beta}(\cos\theta\cos\phi\cos\alpha + \sin\theta\sin\alpha) \tag{F.7}$$

$$\dot{\beta} = p\sin\alpha - r\cos\alpha + \frac{1}{V_T}(YOM\cos\beta + DOM\sin\beta) + \frac{g}{V_T}(\cos\theta\sin\phi\cos\beta + \sin\theta\sin\beta\cos\alpha - \cos\theta\cos\phi\sin\beta\sin\alpha) \tag{F.8}$$

$$\dot{V}_T = YOM\sin\beta - DOM\cos\beta + g\left[(\cos\theta\cos\phi\sin\alpha - \sin\theta\cos\alpha)\cos\beta + \cos\theta\sin\phi\sin\beta\right] \tag{F.9}$$

$$DOM = \frac{D - T\cos\alpha}{m},\ YOM = \frac{Y}{m},\ LOM = \frac{L + T\sin\alpha}{m}$$

Where m is the mass of the vehicle and L, Y, D, T are lift, side, drag, and thrust forces respectively. It is assumed that the accelerations due to forces are in the stability coordinates, L, Y, D and that the thrust force, T, acts along the vehicle primary axis, x_b, and in the positive direction. For longitudinal acceleration loading of the accelerometers, the primary and tertiary acceleration loads at the vehicle's center of gravity must be defined. Figure F.1 displays all normal and axial forces along with angle of attack and lift and drag force directions.

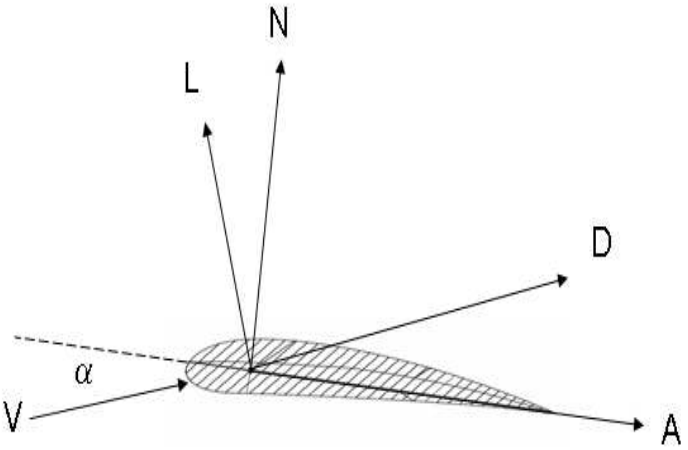

Figure F.1: Forces on Airfoil in Normal and Axial Directions

The drag force, $\vec{\mathbf{D}}$, is collinear with the velocity, $\vec{\mathbf{V}}$, flowing over the airfoil with the lift force, $\vec{\mathbf{L}}$ perpendicular to the drag force. The vehicle primary axis, x_b, is antiparallel with the axial direction of the airfoil, $\vec{\mathbf{A}}$, and the vehicle tertiary axis, z_b is antiparallel with the airfoil normal vector, $\vec{\mathbf{N}}$. The angle of attack, α, is the angle between the vehicle's

velocity vector and the vehicle's primary axis. Using Figure F.1 to sum the lift and drag forces directed along the vehicle's primary and tertiary axes result in the following imposed, inertial, accelerations measured by the accelerometers placed at the vehicle's center of gravity.

$$A_{X,CG} = -\vec{F}_{\vec{A}} = T + L\sin\alpha - D\cos\alpha = F_{X,Imposed} + W_X \tag{F.10}$$

$$A_{Z,CG} = -\vec{F}_{\vec{N}} = -L\cos\alpha - D\sin\alpha = F_{Z,Imposed} + W_Z \tag{F.11}$$

Equations F.10 and F.11 summarize the results of the vehicle imposed loading and the weight of the vehicle. The imposed inertial loads, $F_{X,Imposed}$ and $F_{Z,Imposed}$, result from thrust and aerodynamic imposed forces due to vehicle maneuvers. The effect of weight on vehicle defined using the vehicle's Euler attitude angles and scalar weight, product of mass and local acceleration of gravity, of the aircraft.

$$\mathbf{W} = mg \begin{Bmatrix} \sin\theta \\ \sin\phi\cos\theta \\ \cos\phi\cos\theta \end{Bmatrix} \tag{F.12}$$

Aircraft Stability Derivative Equations

The aerodynamic force vector, $\mathbf{F}_{Aerodynamic}$, given in Equation 2.9 and the external moment vector, $\mathbf{M}_{ext}$, given in Equation 2.10 are defined by the following equations:

$$\mathbf{F}_{Aerodynamic} = \begin{Bmatrix} Lift \\ Drag \\ Side \end{Bmatrix} = \begin{Bmatrix} \bar{q}SC_L \\ \bar{q}SC_D \\ \bar{q}SC_Y \end{Bmatrix} \tag{F.13}$$

$$\mathbf{M}_{ext} = \begin{Bmatrix} M_{Xaxis} \\ M_{Yaxis} \\ M_{Zaxis} \end{Bmatrix} = \begin{Bmatrix} \bar{q}SbC_l \\ \bar{q}ScC_m \\ \bar{q}SbC_n \end{Bmatrix} \tag{F.14}$$

The force and moment coefficients are given below with the constants and stability derivatives defined in Tables F.2 and F.1.

Force Coefficients

$$C_L = C_{L_0} + C_{L_\alpha}\alpha + \frac{c}{2V_T}\left(C_{L_q}q + C_{L_{\dot{\alpha}}}\dot{\alpha}\right) + C_{L_{\delta e}}\delta e + C_{L_{\delta f}}\delta f \tag{F.15}$$

$$C_D = C_{D_0} + C_{D_\alpha}\alpha + \frac{c}{2V_T}\left(C_{D_q}q + C_{D_{\dot{\alpha}}}\dot{\alpha}\right) + C_{D_{\delta e}}\delta e + C_{D_{\delta f}}\delta f \tag{F.16}$$

$$C_Y = C_{Y_0} + C_{Y_\beta}\beta + \frac{b}{2V_T}\left(C_{Y_p}p + C_{Y_r}r\right) + C_{Y_{\delta a}}\delta a + C_{Y_{\delta r}}\delta r \tag{F.17}$$

$$Where\ \delta e = elevator\ deflection,\ \delta a = aileron\ deflection,\ \delta f = flap\ deflection,\ and\ \delta r = rudder\ deflection$$

Moment Coefficients

$$C_l = C_{l_0} + C_{l_\beta}\beta + \frac{b}{2V_T}\left(C_{l_p}p + C_{l_r}r\right) + C_{l_{\delta a}}\delta a + C_{l_{\delta r}}\delta r \tag{F.18}$$

$$C_m = C_{m_0} + C_{m_\alpha}\alpha + \frac{c}{2V_T}\left(C_{m_q}q + C_{m_{\dot\alpha}}\dot\alpha\right) + C_{m_{\delta e}}\delta e + C_{m_{\delta f}}\delta f \tag{F.19}$$

$$C_n = C_{n_0} + C_{n_\beta}\beta + \frac{b}{2V_T}\left(C_{n_p}p + C_{n_r}r\right) + C_{n_{\delta a}}\delta a + C_{n_{\delta r}}\delta r \tag{F.20}$$

F.2 Aircraft Nomenclature and Stability Derivatives

Tables F.1 and F.2 give the values of the aircraft constants and stability derivatives used in the nonlinear aircraft model of this work as well as their respective values. The values used in both tables were calculated from flight data of an aircraft in trimmed flight conditions or known a priori about the aircraft. To verify trimmed flight of the aircraft due to the used values, Figure F.2 displays the aircraft response parameters showing the aircraft is in stable trimmed flight. The units of Table F.1 are per degree except for dimensionless "naught"terms.

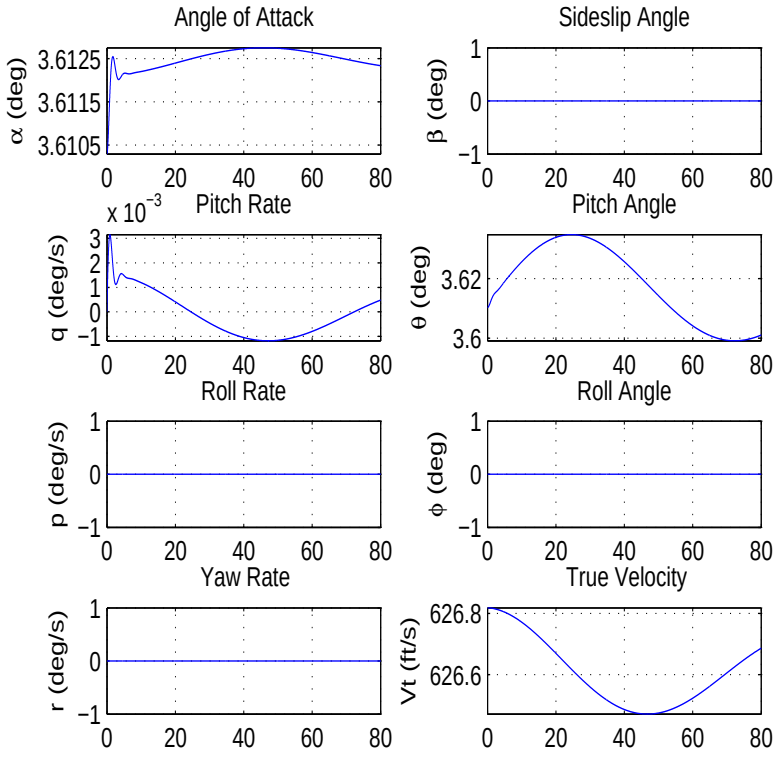

Figure F.2: Nonlinear Simulation Trimmed Flight

Variable	Meaning	Value
C_L	Total Lift Coefficient	Equation F.15
C_{L_0}	Initial Lift	0.004608463
C_{L_α}	Lift Change with respect to α	0.0794655
C_{L_q}	Lift Change with respect to pitch rate	0.0508476
$C_{L_{\dot{\alpha}}}$	Lift Change with respect to $\dot{\alpha}$	0.0
$C_{L_{\delta e}}$	Lift Change with respect to δe	0.0121988
$C_{L_{\delta f}}$	Lift Change with respect to δf	0.0144389
C_D	Total Drag Coefficient	Equation F.16
C_{D_0}	Initial Drag	0.01192128
C_{D_α}	Drag Change with respect to α	0.00550063
C_{D_q}	Drag Change with respect to pitch rate	0.00315057
$C_{D_{\dot{\alpha}}}$	Drag Change with respect to $\dot{\alpha}$	0.0
$C_{D_{\delta e}}$	Drag Change with respect to δe	-0.000587647
$C_{D_{\delta f}}$	Drag Change with respect to δf	0.00136385
C_Y	Total Side Force Coefficient	Equation F.17
C_{Y_0}	Initial Side Coefficient	0.0
C_{Y_β}	Side Force Change with respect to β	-0.0219309
C_{Y_p}	Side Force Change with respect to roll rate	0.00133787
C_{Y_r}	Side Force Change with respect to yaw rate	0.0094053
$C_{Y_{\delta a}}$	Side Force Change with respect to δa	0.00049355
$C_{Y_{\delta r}}$	Side Force Change with respect to δr	0.00293048
C_l	Total Rolling Moment Coefficient	Equation F.18
C_{l_0}	Initial rolling moment	0.0
C_{L_β}	Rolling moment Change with respect to β	-0.00173748
C_{l_p}	Rolling moment Change with respect to roll rate	-0.00739342
C_{l_r}	Rolling moment Change with respect to yaw rate	0.0000699792
$C_{l_{\delta a}}$	Rolling moment change with respect to δa	-0.00213984
$C_{l_{\delta r}}$	Rolling moment change with respect to δr	0.000479021
C_m	Total Pitching Moment Coefficient	Equation F.19
C_{m_0}	Initial pitching moment	-0.02092347
C_{L_α}	Pitching moment Change with respect to α	-0.0041873
C_{m_q}	Pitching moment Change with respect to pitch rate	-0.110661

Table F.1: Aircraft Stability Derivatives

Aircraft Stability Derivatives *(continued)*

Variable	Meaning	Value
$C_{m_{\dot{\alpha}}}$	Pitching moment Change with respect to $\dot{\alpha}$	0.0
$C_{m_{\delta e}}$	Rolling moment change with respect to δe	-0.0115767
$C_{m_{\delta f}}$	Rolling moment change with respect to δf	0.000580220
C_n	Total Yawing Moment Coefficient	Equation F.20
C_{n_0}	Initial Yawing moment	0.0
C_{n_β}	Yawing moment Change with respect to β	0.00320831
C_{n_p}	Yawing moment Change with respect to roll rate	-0.000432575
C_{n_r}	Yawing moment Change with respect to yaw rate	-0.00886783
$C_{n_{\delta a}}$	Yawing moment change with respect to δa	-0.000206591
$C_{n_{\delta r}}$	Yawing moment change with respect to δr	-0.00144865

Table F.1: Aircraft Stability Derivatives

Variable	Meaning	Value
$\bar{q}$	Dynamic Pressure	$0.5\rho V_T^2$
S	Wing Platform Area	300 ft^2
b	Wingspan	30 ft
c	Wing Chord	11.32 ft
m	Aircraft Mass	762.85 slug
ρ	Air Density	0.001496 slug/ft^3
g	Force of Gravity	32.175619 ft/sec^2
I_{xx}	Primary Axis Mass Moment of Inertia	8890.63 slug-ft^2
I_{yy}	Secondary Axis Mass Moment of Inertia	71973.5 slug-ft^2
I_{zz}	Tertiary Axis Mass Moment of Inertia	77141.1 slug-ft^2
I_{xz}	Cross Product Mass Moment of Inertia	181.119 slug-ft^2
I_{xy}	Cross Product Mass Moment of Inertia	0 slug-ft^2
I_{yz}	Cross Product Mass Moment of Inertia	0 slug-ft^2

Table F.2: Aircraft Constants

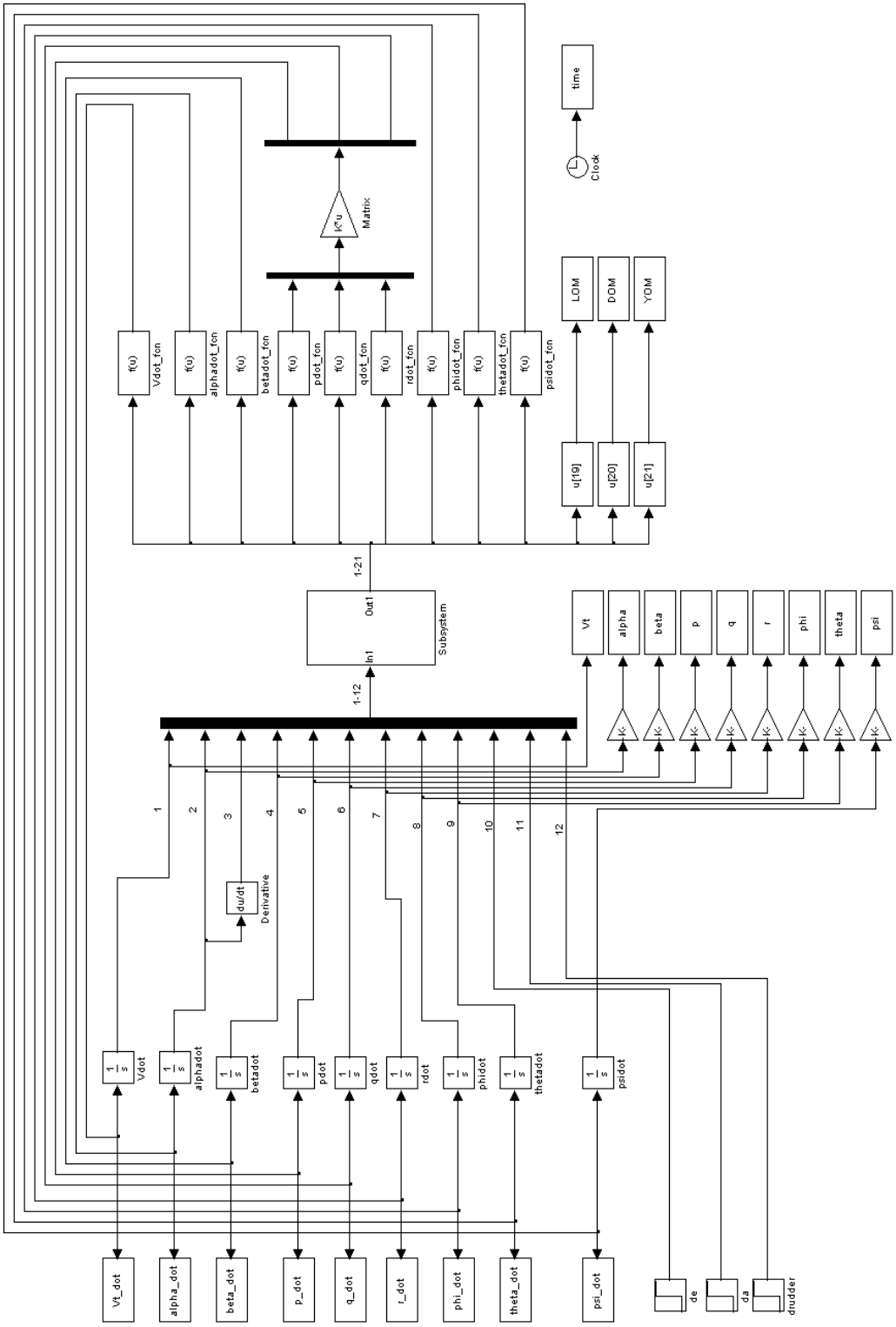

Figure F.3: Aircraft Simulink Model

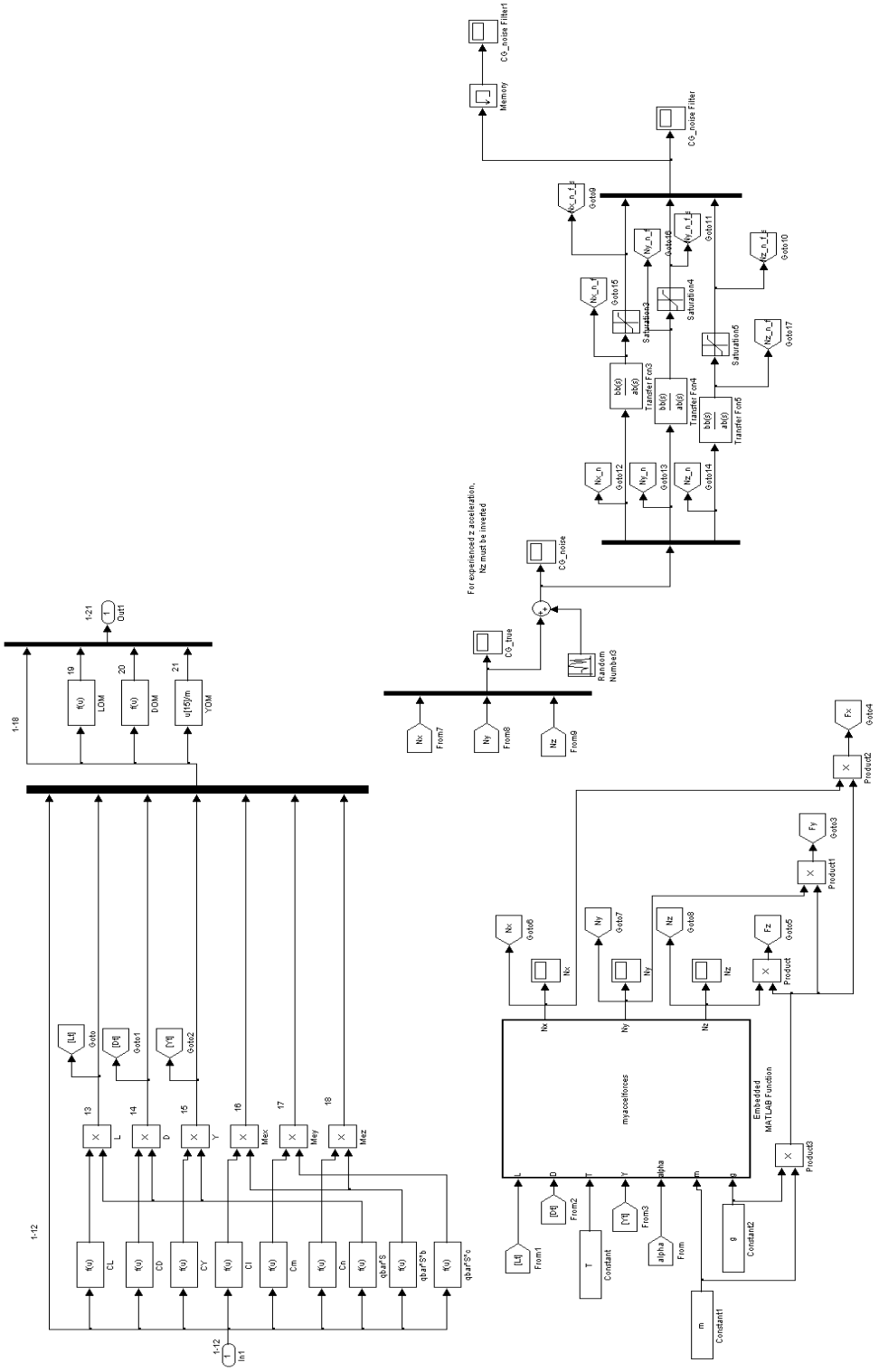

Figure F.4: Simulink Equations of Motion for Aircraft Model

Appendix G

Supplemental Figures

This Appendix displays additional figures in support of the work conducted.

G.1 From Section 4.2 - Back-Difference Estimation

For the linear simulation with the double pitch doublet maneuvers conducted over a simulation time of 3600 seconds with one doublet at 1200 seconds and one doublet at 2400 seconds.

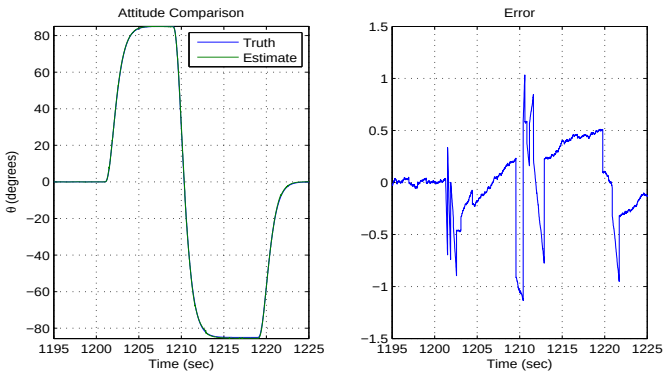

Figure G.1: Attitude Estimate and Error Plots at 1200 seconds

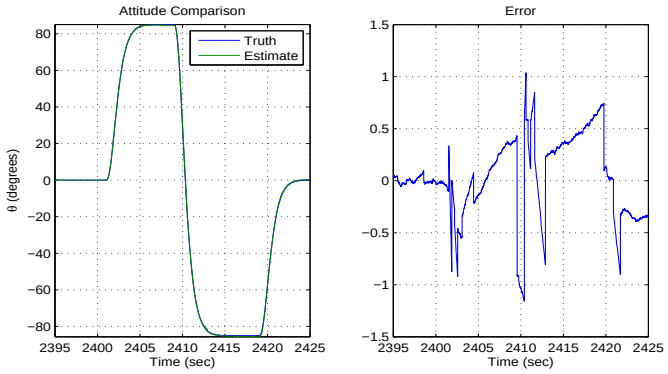

Figure G.2: Attitude Estimate and Error Plots at 2400 seconds

G.2 From Section 4.2 - Kalman Filter Estimation

G.2.1 First Iteration of KF Parameters

The following is a zoomed in plot of Figure 4.10 showing the bias estimate converges to within ±0.15 degrees/second after 10 seconds.

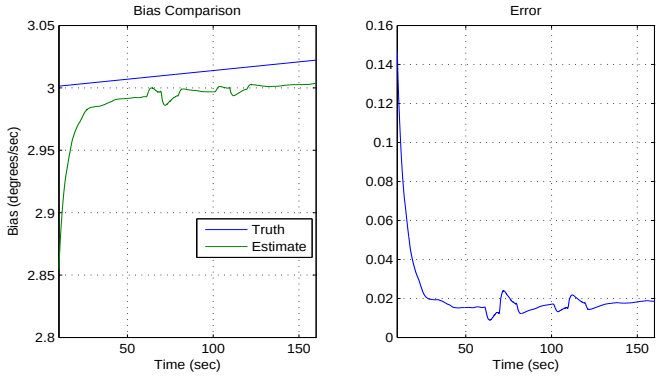

Figure G.3: Zoom of Figure 4.10

The following are the comparison of the state error with the imposed bounds of the state covariance matrix using the first iteration of noise variances with the state covariance matrix set essentially at infinity.

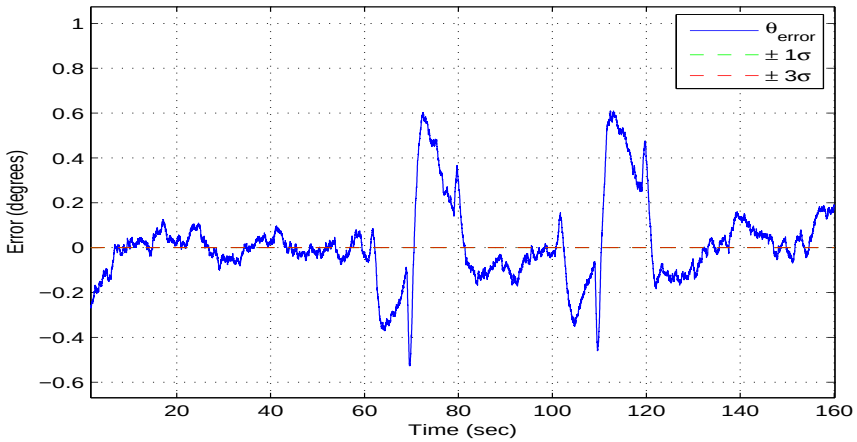

Figure G.4: Attitude Error and Covariance - Covariance Matrix Increased

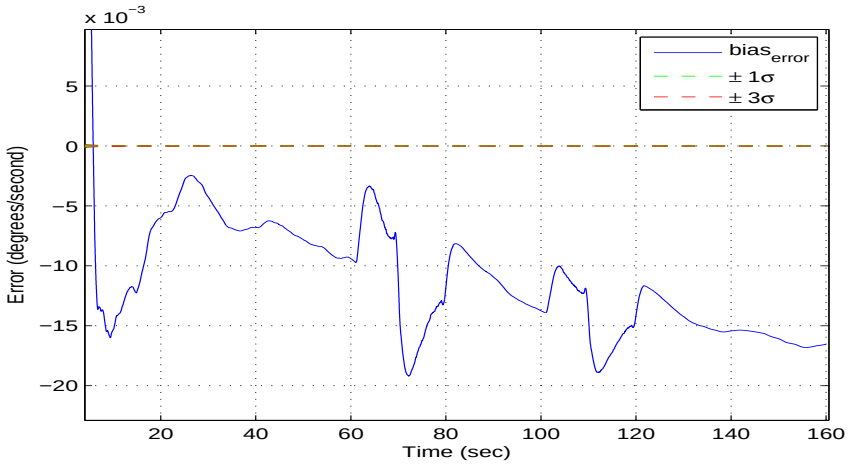

Figure G.5: Bias Error and Covariance - Covariance Matrix Increased

G.2.2 Second Iteration of KF Parameters

The following two plots compare the bias errors of both the second iteration of the Kalman Filter and the Quaternion Back-difference algorithm for the sinusoid and Step-and-Hold maneuvers. The Y-Axis scales are set to ± 3 degrees/second because that is the magnitude of the largest Quaternion Back-Difference excursion.

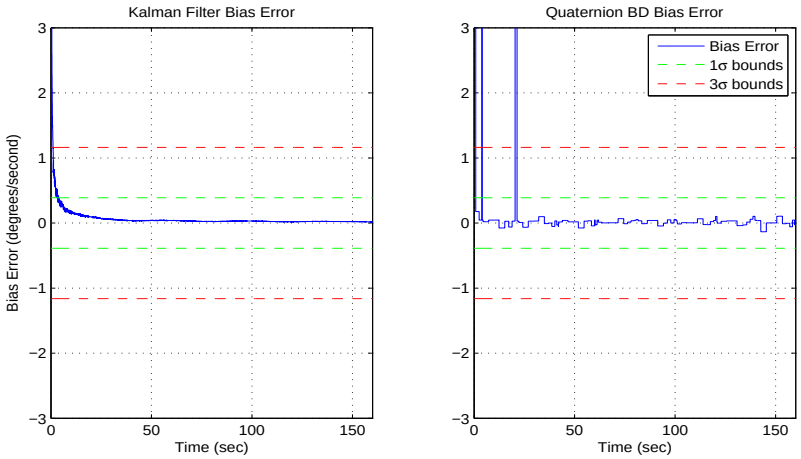

Figure G.6: 2nd Iteration LDFK Sinusoid Bound Comparison

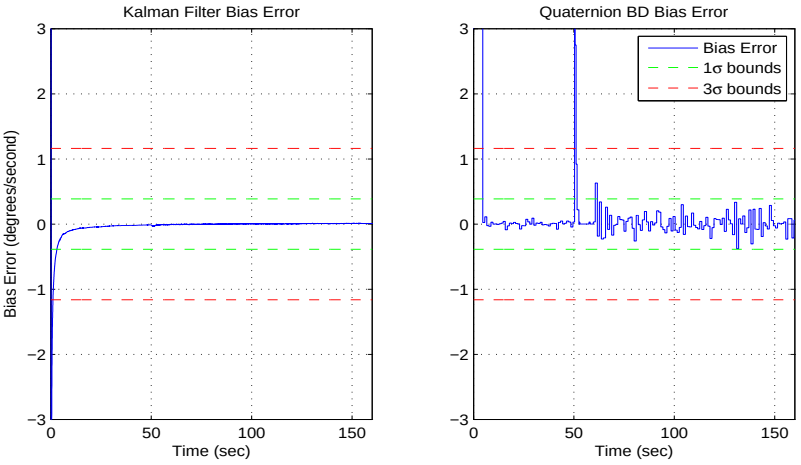

Figure G.7: 2nd Iteration LDKF Step-and-Hold Bound Comparison

G.3 From Section 4.4 - Kalman Filter Estimation

Third Iteration of KF Parameters

The following plot is the covariance analysis of the bias error from the third iteration of Kalman Filter parameters for the phase II nonlinear model simulation.

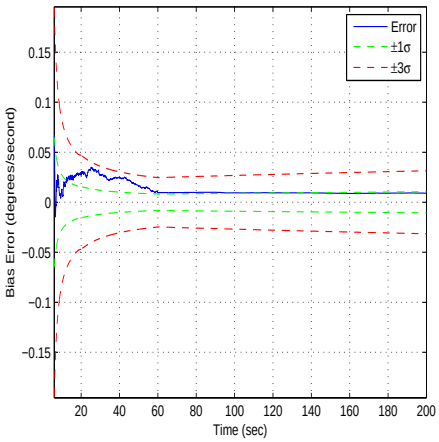

Figure G.8: 3rd Iteration LDKF Bias Covariance Analysis - Nonlinear Phase II

G.4 From Section 4.5 - Algorithm Comparison with Published Results

Omitted Plots for 3rd Iteration of LDKF

The subsequent plots were omitted from Section 4.5 for brevity and the filter fails correctly operate within the imposed covariance bounds for off-line operation checks.

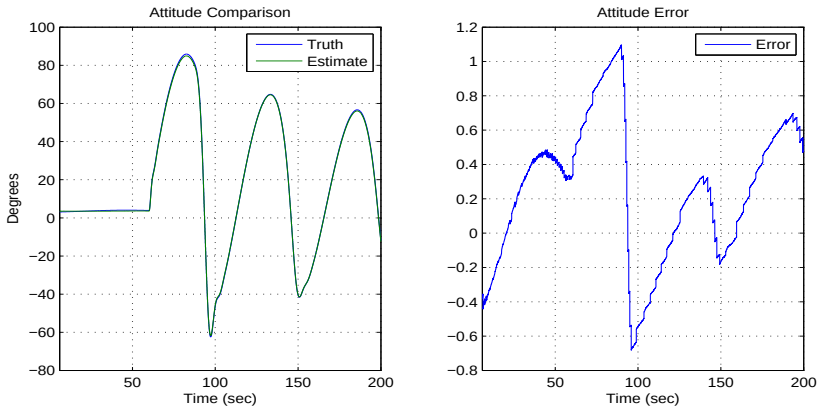

Figure G.9: Attitude Results using Published Noise Parameters - 3rd LDKF

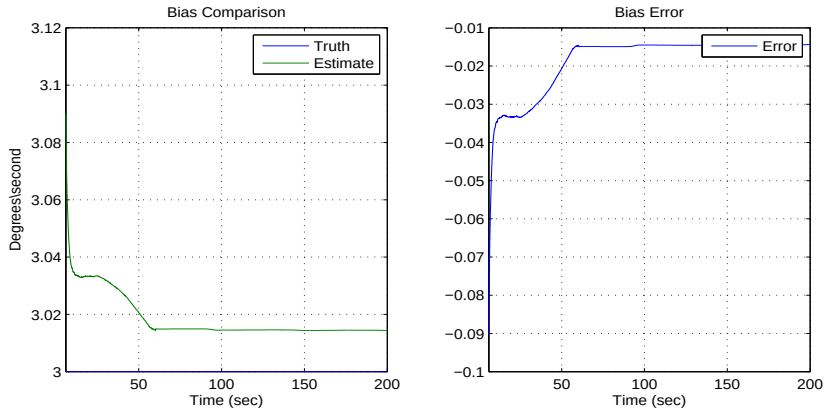

Figure G.10: Bias Results using Published Noise Parameters - 3rd LDKF

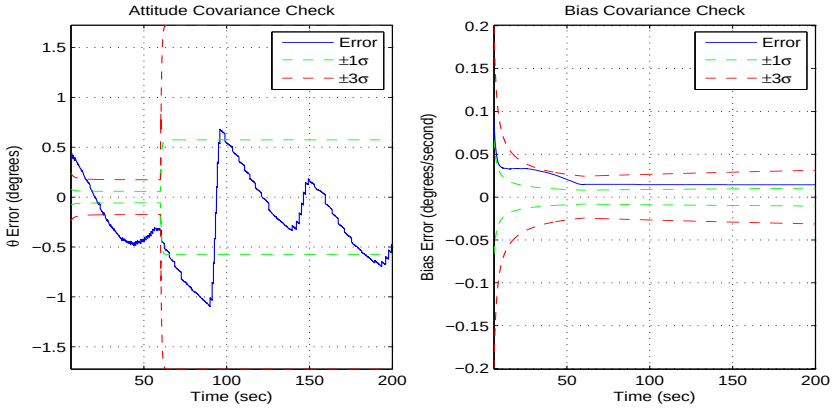

Figure G.11: Covariance Error Results using Published Noise Parameters - 3rd LDKF

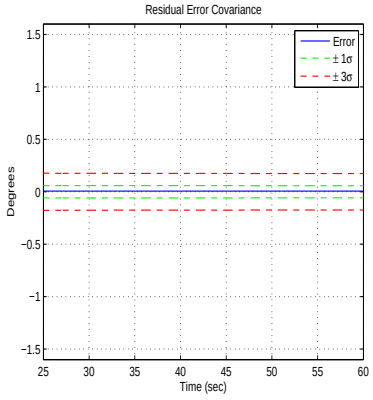

Figure G.12: Residual Error Results using Published Noise Parameters - 3rd LDKF

For all those who have gone before,
Thank you for the impact on my life
Harry Weisman II
Jerome Beach
Steven Beach
Darrell Beach
Caroline Weisman
Christopher Boyle
Marg Davidson

Serenity Prayer:
"*God grant me the Serenity to accept the things I cannot change,*
the Courage to change the things I can,
and the Wisdom to know the difference."